SYSTEMATIC CODE VERIFICATION AND VALIDATION OF DAMAGE IN HIGH STRENGTH ARMOR MATERIALS

by

Krishna C Kamojjala

A dissertation submitted to the faculty of
The University of Utah
in partial fulfillment of the requirements for the degree of

Doctor of Philosophy

Department of Mechanical Engineering

The University of Utah

December 2014

The University of Utah Graduate School

STATEMENT OF DISSERTATION APPROVAL

The dissertation of **Krishna C Kamojjala**

has been approved by the following supervisory committee members:

Rebecca M. Brannon	, Chair	**09-May-2014** Date Approved
James Guilkey	, Member	**09-May-2014** Date Approved
A. K. Balaji	, Member	**09-May-2014** Date Approved
K. S. Ravi Chandran	, Member	**09-May-2014** Date Approved
Daniel O. Adams	, Member	Date Approved

and by **Tim Ameel** , Chair/Dean of

the Department/College/School of **Mechanical Engineering**

and by David B. Kieda, Dean of The Graduate School.

ABSTRACT

With a goal towards improving predictions of metallic armor damage observed in the laboratory investigations of unnotched Charpy impact and Taylor-anvil impact experiments, a systematic verification and validation (V&V) study is presented. Solid mechanics lags behind other scientific communities in terms of code verification research. To address this gap, increasingly complicated code verification tests appropriate for benchmark testing of solid-mechanics codes are presented. Simple patch tests for frame-indifference and traction boundary conditions under affine deformations, followed by two large-deformation problems, are designed using method of manufactured solutions (MMS) technique for solid-mechanics codes. These large-deformation verification problems have all particles undergoing identical loading modes (simple shear or uniaxial strain) to various levels of intensity and with various amounts of superimposed rotation. Initially, they are designed for nonlinear-elastic constitutive models, and then two of them are extended to a more complicated path-dependent model. Furthermore, systematic validation studies of two engineering applications (unnotched Charpy and Taylor-anvil impact) are presented using damage theories that include aleatory uncertainty and scale effects with the focus on comparing the predicted fields with laboratory data. These features, however, sometimes mitigate mesh dependencies while other times exacerbating them. The Brazilian indirect tension test, which is known to exhibit mesh dependency when run with variability and scale effects is re-analyzed using a novel numerical technique called data relocalization. For failure initiation, slow convergence is first demonstrated using a 1D MMS with both low-order and high-order elements. Slow convergence is likewise demonstrated for a more complicated Brazilian test, and then data relocalization is shown to significantly accelerate convergence for the low-order case when the prefailure stress field is known.

CONTENTS

LIST OF FIGURES

LIST OF TABLES

ACKNOWLEDGEMENTS

First and foremost, I would like to thank my advisor, Dr. Rebecca Brannon, for continuously encouraging me throughout my graduate career. It has been an honor to pursue my Ph.D. under her advisement and all her contributions during my academic career are highly appreciated. I would also like to thank Dr. James Guilkey for his valuable assistance helping me to achieve my research and professional goals. Special thanks to my graduate committee members, Dr. A. K. Balaji, Dr. K.S. Ravi Chandran, and Dr. Daniel Adams, for their time and interest.

I would like to appreciate my fellow students, Dr. Jeffrey Burghardt, James Colovos, Asghar Yarahmadi, HamidReza Sarmadi, Steven Schmidt and Emad Ghodrati, for their help and assistance. Specifically, I would like to thank Brian Leavy, Dr. Alireza Sadeghirad, Scot Swan, David Austin, Michael Homel and Dr. Timothy Fuller as they have directly helped my research in some way.

I am grateful to Jeffrey Lacy and Henry Chu at Idaho National Laboratory for providing the experimental details on unnotched Charpy and Taylor-anvil impact and also for their generous support in sponsoring the research. I am also grateful to Bill Bruchey at Survice Engineering for his momentous support during the modeling effort. I would like to express my appreciation to Survice Engineering, Schlumberger Technology Corporation and Sandia National Laboratories for sponsoring my research.

The support and resources from the Center for High Performance Computing at the University of Utah is gratefully acknowledged. I would also like to thank the administrative department of Mechanical Engineering for providing all the necessary paperwork during my Ph.D.

Lastly, I would like to thank my family and friends for their unconditional love and support. To my parents, as they have been a constant source of strength and inspiration. To my sisters for their moral support. Finally, I would like to thank my wife, Pavani, for her love, encouragement and patience during all stages of my Ph.D.

CHAPTER 1

INTRODUCTION

1.1 Verification and validation

Computer simulations of physical events play a crucial role in decision making for both industry and the scientific community. Systematic verification and validation (V&V) establishes confidence in the predictions of these computer models. Code verification is the process of demonstrating that the governing equations are solved correctly, whereas code validation is the evidence that the predictions of these governing equations are acceptable approximations to reality for a given engineering application [79].

Code verification is a necessary prerequisite to code validation. Different types of verification tests commonly adopted by the scientific community include single-element tests, trend tests, symmetry tests, comparison tests, convergence tests, the method of exact solutions (MES), and the method of manufactured solutions (MMS). This research focuses primarily on single-element and MMS testing, each of which is defined in greater detail below. This verification work is then supplemented with validation testing for engineering applications of constitutive damage theories that include aleatory uncertainty and scale effects.

Single-element tests are very useful during the development stage of the constitutive models where the numerical predictions of stress are compared against analytical solutions. For the situations where the analytical solutions are not available, trend tests, convergence tests, symmetry tests, and comparison tests are used to verify the code based on expert judgment. With the known analytical solutions, convergence tests are also used to illustrate the magnitude of the discretization error based on a grid refinement study. In the MES, the source terms (*e.g.,* boundary conditions and body forces) are chosen, and then the solution of the governing equations is derived analytically. However, simplifying assumptions (*e.g.,* small deformations or otherwise simplistic displacement fields) are often required to derive these solutions. In MMS, on the other hand, a solution is manufactured, and then the source terms are found by solving the partial differential equations backwards [51].

Of all the verification tests mentioned above, only MES and MMS can be used to assess the error of the host-code solver of the momentum equation. The advantage of the MMS is that it can more compellingly verify a majority of code capabilities compared to other forms of verification testing. However, limitations of these manufactured solutions arise if the code does not allow for applying variable forcing terms as an option to the user.

The MMS technique has been extensively used in fluid mechanics, electromagnetics, heat transfer, nuclear engineering *etc.*, but has been relatively ignored in the solid mechanics community. The manufactured solutions in solid mechanics are limited to elastic constitutive models under simplistic deformation modes (small deformations without rotations and/or distortions). To address this gap, the primary purpose of this dissertation is to develop code verification tests using the MMS technique for large deformations using both elastic and more complicated path-dependent constitutive models. Section 1.2 provides an overview of the MMS technique for solid mechanics. Chapters 2 and 3 provide a series of increasingly complicated code verification tests designed for solid mechanics using elasticity and plasticity. These problems are designed in such a way that they can be relatively easily extended to special cases of damage models.

Predictive damage simulations benefit many industries like aerospace, automotive, defense, safety *etc.* Previous work has shown that the computational mesh and the material model significantly affect the damage patterns in impact simulations [90, 91, 6]. The secondary purpose of this dissertation is to perform a validation study of damage observed in unnotched Charpy and Taylor-anvil impact experiments along with resolving some verification convergence difficulties known to arise with such models. Section 1.4 provides the overview of the constitutive model used for this validation study and Chapter 4 provides the details of the numerical results. Non-convergence is demonstrated using a deterministic model, and then improved results are shown with the inclusion of statistical variability in strength and scale effects. These features, however, sometimes mitigate mesh dependencies, while other times they aggravate them.

Chapter 5 provides a novel numerical alternative stress field regularization technique (which we call *data relocalization*) designed to preserve probabilities of failure initiation. To illustrate the concept, the strength is taken to be Weibull distributed (though the same approach should apply to more realistic distributions). For the purpose of determining failure probability, the uniform stress state assigned to a low-order finite element is set equal to the m-norm of the actual (spatially varying) stress field on the element, where m is the Weibull modulus. The use of an m-norm is shown to be sufficient to preserve

probability of failure initiation of a finite subdomain of the body regardless of whether it is discretized into few or many elements. The concept is first demonstrated using the method of manufactured solutions in 1D. Using statistical variability and scale effects, slow convergence is demonstrated for a more complicated Brazilian test using low-order elements, and then data relocalization is shown to significantly accelerate convergence for the low-order case when the prefailure stress field is known.

1.2 Method of manufactured solutions

This section provides a brief procedure of designing verification problems using method of manufactured solutions (MMS). MMS is the process of deriving the analytical body forces, tractions, and initial conditions required to achieve a predetermined deformation field. These analytical forcing functions are supplied as inputs to the codes, and error is then quantified by comparing the predicted and predetermined displacement and stress fields. The primary governing equation of motion in continuum mechanics is balance of momentum:

$$\operatorname{div}(\boldsymbol{\sigma}) + \rho \boldsymbol{b} = \rho \boldsymbol{a} \ , \tag{1.1}$$

where $\boldsymbol{\sigma}$ is Cauchy stress, ρ is the spatial mass density, $\boldsymbol{b}$ is the body force, $\boldsymbol{a}$ is the acceleration, and $\operatorname{div}\boldsymbol{\sigma}$ is the spatial divergence of stress, having its i^{th} component given by $\partial \sigma_{ij}/\partial x_j$ (where repeated indices are implicitly summed from 1 to 3). Sometimes, the reference form of the momentum equation,

$$\operatorname{DIV}(\boldsymbol{P}) + \rho_0 \boldsymbol{b} = \rho_0 \boldsymbol{a} \ , \tag{1.2}$$

is more convenient. Here, $\boldsymbol{P}$ is the first Piola-Kirchhoff (PK1) stress defined by $\boldsymbol{P} = J\boldsymbol{\sigma} \cdot \boldsymbol{F}^{-T}$, ρ_0 is the initial density, $\operatorname{DIV}(\boldsymbol{P})$ is the backwards reference divergence of $\boldsymbol{P}$, defined with respect to the Cartesian basis $(\mathbf{E}_1, \mathbf{E}_2, \mathbf{E}_3)$ by

$$\operatorname{DIV}(\boldsymbol{P}) = \frac{\partial P_{ij}}{\partial X_j}\mathbf{E}_i = \frac{\partial \boldsymbol{P}}{\partial \boldsymbol{X}} : \boldsymbol{I} \ , \tag{1.3}$$

where ":" is the second-order tensor inner product, and $\boldsymbol{I}$ is the second-order identity tensor, $\boldsymbol{F}$ denotes the deformation gradient tensor, and $J = \det\boldsymbol{F}$.

First, a predetermined displacement/deformation field is chosen from which the initial conditions for displacement and velocity can be computed. To determine the body force from Eq. (1.1), the acceleration and the stress divergence need to be evaluated. Acceleration is the second derivative of the displacement field with respect to time (which is known, by

design, from the predetermined deformation). In solid mechanics, a constitutive model gives stress as a function of deformation gradient/strain/strain history/*etc.*, and knowing the predetermined displacement field is sufficient (though nontrivial) to determine the stress field and its divergence, thus allowing the body force to be found from Eq. (1.1). Since the stress field is available, the boundary traction is given by $\boldsymbol{t} = \boldsymbol{\sigma} \cdot \boldsymbol{n}$, where $\boldsymbol{\sigma}$ is the Cauchy stress and $\boldsymbol{n}$ is the unit outward normal. Once all of the forcing functions are derived, they are supplied as inputs to the code, and the accuracy of the constitutive model and momentum solver is then quantified by comparing the predicted displacement and stress fields with the manufactured fields.

Single-element tests are one of the simplest MMS cases, for which the predetermined deformation field is homogeneous. Before solving a single-element test as an MMS, it is helpful to first develop and test the constitutive models as MES problems in which the forcing function is the prescribed homogeneous deformation field. To illustrate, this research aims to verify and validate one particular general-purpose plasticity and damage code, called Kayenta, which is summarized in Sec. 1.4.

1.3 The Material Point Method (MPM)

Validation studies on unnotched Charpy and Taylor-impact tests are performed in the Uintah computational framework [34] using the Kayenta material model [15].

Uintah uses the material point method (MPM) [87] to solve the momentum equation. Advantages of MPM over conventional Lagrangian finite-element methods or Eulerian finite-difference methods is that MPM includes an automatic no-slip no-stick contact behavior without any special revisions to the code and without needing to know *a priori* which surfaces are going to interact. This has obvious appeal for applications of fragmentation that introduce material fragments that might impact each other. Moreover, the MPM saves constitutive internal field variables at Lagrangian particles that move arbitrarily through an overlaid rectilinear grid on which the weak form of the momentum equation is solved.

The governing equations on the overlaid grid are identical to those for a conventional finite-element method. For example, the lumped mass and force integrals on the grid are

$$m_i = \int_\Omega \rho(\boldsymbol{x}, t) S_i(\boldsymbol{x}) \, \mathrm{d}V \; ; \qquad f_i^{\mathrm{int}} = - \int_\Omega \boldsymbol{\sigma}(\boldsymbol{x}, t) \cdot \nabla S_i(\boldsymbol{x}) \, \mathrm{d}V. \tag{1.4}$$

In either case, the problem is essentially to evaluate the integral some field $h_i(\boldsymbol{x}, t)$ over the entire domain,

$$\int_\Omega h_i(\boldsymbol{x}, t) \, \mathrm{d}V \; . \tag{1.5}$$

For the internal nodal force vector, the generic integrand $h_i(\boldsymbol{x}, t)$ is

$$h_i(\boldsymbol{x}, t) = \boldsymbol{\sigma}(\boldsymbol{x}, t) \cdot \nabla S_i(\boldsymbol{x}) \, . \tag{1.6}$$

The integrand for the nodal mass is

$$h_i(\boldsymbol{x}, t) = \rho(\boldsymbol{x}, t) S_i(\boldsymbol{x}) \tag{1.7}$$

In a conventional finite-element method, these are evaluated by summing over element domains and sampling the integrands at Gauss points:

$$\int_\Omega h_i(\boldsymbol{x}, t) \, \mathrm{d}V = \sum_e \int_{\Omega_e} h_i(\boldsymbol{x}, t) \, \mathrm{d}V \approx \sum_g h_i(\boldsymbol{x}_g, t) W_g \tag{1.8}$$

Here, the subscript "e" refers to an element sum, while the the subscript "g" refers to Gauss points (with the Gauss weight denoted W_g).

In the MPM, the same integrals are evaluated by summing over particle domains:

$$\int_\Omega h_i(\boldsymbol{x}, t) \, \mathrm{d}V = \sum_p \int_{\Omega_p} h_i(\boldsymbol{x}, t) \, \mathrm{d}V = \sum_p h_{ip} V_p, \tag{1.9}$$

where

$$h_{ip} = \frac{\int_{\Omega_p} h_i(\boldsymbol{x}, t) \, \mathrm{d}V}{\int_{\Omega_p} \mathrm{d}V} \tag{1.10}$$

and

$$V_p = \int_{\Omega_p} \mathrm{d}V \tag{1.11}$$

Here, h_{ip} is the average of the field $h_i(\boldsymbol{x}, t)$ over the p^{th} particle domain. Variants of MPM are distinguished by how this average is computed, and may be generalized as

$$h_{ip} \approx \frac{\int_{\Omega_p^*} f^*(\boldsymbol{x}, t) \chi(\boldsymbol{x}) \, \mathrm{d}V^*}{V_p^*} \qquad \text{where} \qquad V_p^* = \int_{\Omega_p^*} \chi(\boldsymbol{x}) \, \mathrm{d}V^* \tag{1.12}$$

Here, the desired average of $f(\boldsymbol{x}, t)$ over the particle domain is replaced with a weighted average of an approximate function $f^*(\boldsymbol{x}, t)$, where $\chi(\boldsymbol{x})$ denotes the weighting function, and this approximate average is evaluated over a domain Ω_p^* that might not exactly coincide with the actual particle domain. For example, the approximate function used in the nodal force integral is typically taken as

$$f_i^*(\boldsymbol{x}, t) = \boldsymbol{\sigma}(\boldsymbol{x}_p, t) \cdot \nabla S_i(\boldsymbol{x}) \, . \tag{1.13}$$

which is identical to Eq. (1.6) except that the spatially varying stress $\boldsymbol{\sigma}(\boldsymbol{x}, t)$ is approximated to be uniform over the particle. To recover original formulations of MPM [87], the

weighting function is taken to be a Dirac delta $\chi(\boldsymbol{x}) = \delta(\boldsymbol{x} - \boldsymbol{x}_p)$, while a different method (called GIMP) typically takes the weighting to be a top-hat function equal to 1 over a rectangle (or cuboid in 3D) centered around the particle and 0 elsewhere. A relatively recent integration option, called convected particle domain interpolation (CPDI), uses a first-order accurate approximation of the actual particle domain Ω_p (*i.e.,* Ω_p^* is a parallelepiped determined directly from the deformation gradient tensor). CPDI furthermore makes the integrals tractable by replacing the conventional grid shape functions $S_i(\boldsymbol{x})$ with alternative shape functions $S_i^*(\boldsymbol{x})$, as detailed in Ref. [77].

1.4 Overview of Kayenta

Kayenta is a generalized and unified stress-based plasticity model applicable to a broad class of materials including rock, rock-like engineered materials, metals, *etc.* Similar to engineering plasticity and damage models for concrete [16], Kayenta defines the limits for allowable stress states using both a yield surface and a limit surface. As illustrated in Fig. 1.1, the yield surface is the boundary of elastically obtainable stress states, and the limit surface is the boundary of stress states attainable by any quasistatic means, elastic or plastic. For high-rate loading, the model includes a Duvaut-Lions overstress formulation [24] that permits apparent increase in strength with strain rate by allowing the stress to fall transiently outside of the limit surface.

Damage in Kayenta initiates when the stress state of the material reaches the limit surface. Depending on the model options, the stress state lingers at the limit surface for a finite amount of time before softening, defined by collapse of the limit surface, which takes place as illustrated in Fig. 1.2. During softening, the limit surface collapses to a user-prescribed failed surface, which defaults to a limit surface commonly used for disaggregated sand (which has strength in compression but not tension). In Fig. 1.2, $\sqrt{J_2}$ is the square root of the second stress invariant (equivalent shear stress in the material) and $\bar{I}_1$ is the first stress invariant (positive in compression). Sections 1.4.1 and 1.4.2 provide a brief overview of the Duvaut-Lions overstress formulation for rate dependence and different softening options available in Kayenta.

1.4.1 Rate dependence

Many relatively simplistic engineering plasticity models (*e.g.,* Johnson-Cook) take strength to be a function of strain rate, whereas Kayenta takes strength to be a functional of strain rate. In particular, Kayenta adopts a Duvaut-Lions viscoplastic formulation [24], which permits a transient phase during which the strength under constant strain rate

asymptotes to a final value. The difference between the dynamic and quasistatic strengths is called the overstress. The steady-state overstress under conditions of constant strain rate is used to infer the parameters in the viscoplastic model. Kayenta permits overstress using the parameters T_1 and T_2 for rate effects. In the present build of Kayenta, these T-parameters are used to assign a value of the characteristic time according to the following formula

$$\tau = f\left(\dot{\varepsilon}\right) = T_1 \left(\frac{1}{\dot{\varepsilon}}\right)^{T_2} \tag{1.14}$$

A procedure to parameterize T_1 and T_2 from experimental data is provided in Chapter 4.

1.4.2 Softening

The distinguishing advantage of Kayenta is that it supports both time-to-failure and strain-to-failure softening mechanisms. The difference between the two mechanisms is illustrated via a uniaxial-strain single-element test shown in Fig. 1.3. The uniaxial-strain single-element test is run for each type of softening model at both low strain rate and high strain rate. The constant strain-to-failure model correctly (from a verification perspective) exhibits similar behavior for both strain rates. In contrast, the time-to-failure model takes the same amount of time to fail at all loading rates and therefore the amount of strain accumulated during the failure process is smaller at low strain rates, leading to the noticeably reduced apparent strain-to-failure evident in a time-to-failure formulation.

The different strain-to-failure softening options available in Kayenta are

1. Constant equivalent-strain-to-failure [98] model: Failure will occur when the equivalent strain reaches a critical strain which is defined by a constant value.

$$\varepsilon_f = D_1 \tag{1.15}$$

2. Johnson-Cook failure model [44]: The equivalent strain to failure is given by

$$\varepsilon_f = \left(D_1 + D_2 e^{-D_3 \frac{\sigma_m}{\sigma_e}}\right)\left(1 + D_4 \ln \frac{\dot{\varepsilon}}{\dot{\varepsilon_0}}\right)\left(1 + D_5 \frac{T - T_r}{T_m - T_r}\right) \tag{1.16}$$

where D_1 through D_5 are the model parameters, T_r and T_m are respectively the room temperature and melt temperature, σ_m is the mean stress, σ_e is the von-Mises equivalent stress, $\dot{\varepsilon}$ is the equivalent plastic strain rate, and $\dot{\varepsilon_0}$ is the reference strain rate.

3. Xue-Wierzbicki failure model [6, 96]: The equivalent strain to failure is

$$\varepsilon_f = D_1 e^{-D_2\eta} - \left(D_1 e^{-D_2\eta} - D_3 e^{-D_4\eta}\right)(1-\xi^m)^n\,, \tag{1.17}$$
$$\xi = \frac{27 J_3}{2\sigma_e^3},\ \ \eta = \frac{\sigma_m}{\sigma_e},\ \ \text{and}\ \ m = 2\,\text{Round}\left(\frac{1}{2n}\right)$$

where D_1 through D_4 are the model parameters, σ_m is the mean stress, σ_e is the von-Mises equivalent stress, ξ is called the Lode parameter, n is the hardening exponent, and $J_3 = \det(\boldsymbol{S})$, where $\boldsymbol{S}$ is the deviatoric part of the stress tensor.

A comprehensive verification of the implementation of these strain-to-failure softening options is provided in [88]. Chapter 4 details the validation study on unnotched Charpy and Taylor-anvil impact using the constant equivalent-strain-to-failure and Johnson-Cook softening options.

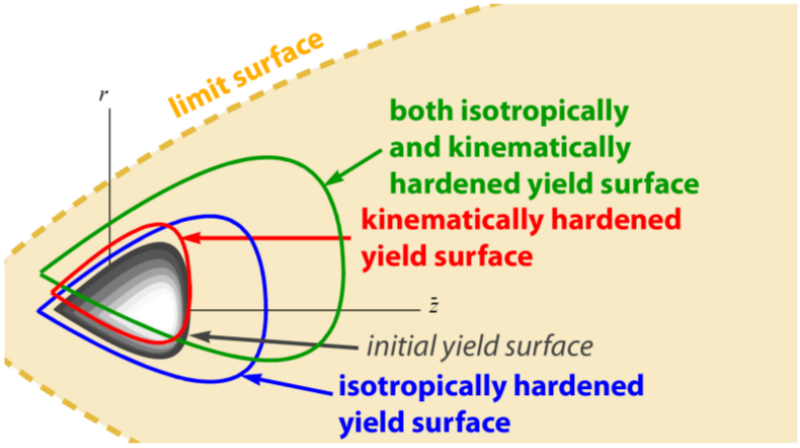

Figure 1.1: Difference between a yield surface and the limit surface. Reproduced with permission [15]

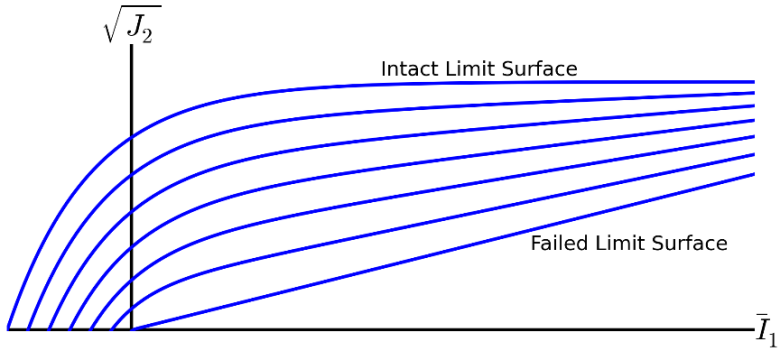

Figure 1.2: The collapse of limit surface to a failed surface during softening. Reproduced with permission [15]

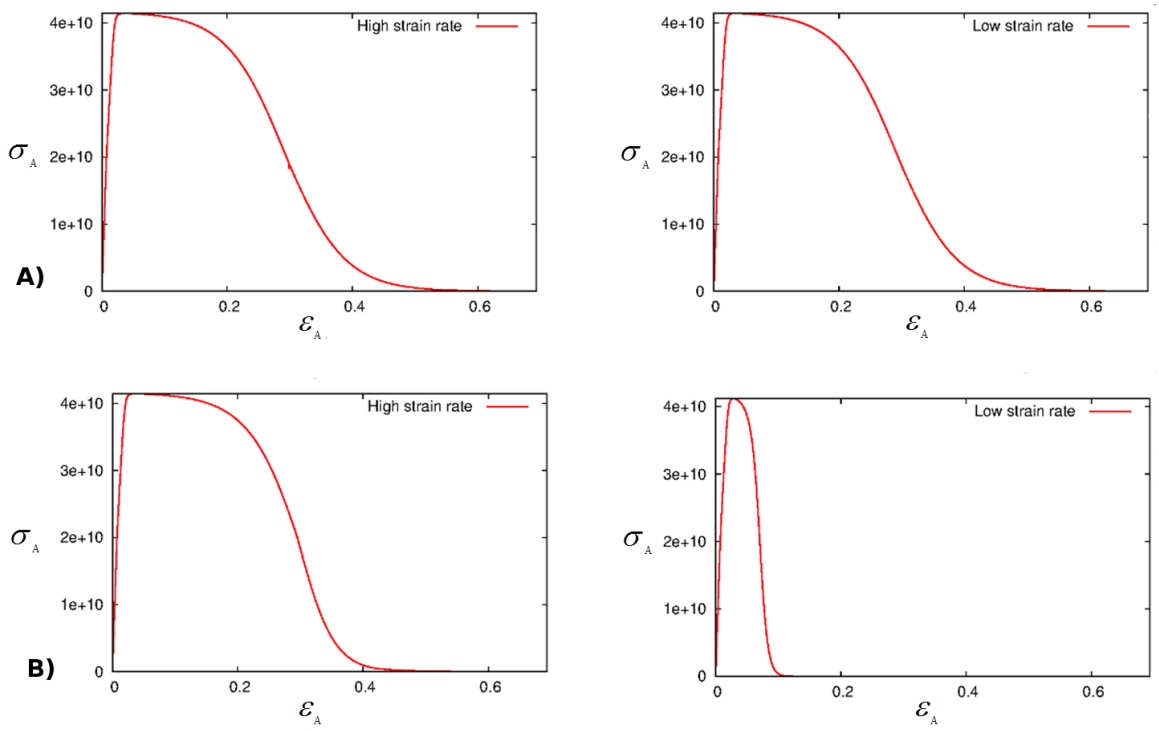

Figure 1.3: Time-to-failure vs. strain-to-failure softening for a single element uniaxial strain simulation. A) Simulation using strain-to-failure predicting the same failure strain for both the rates. B) Same simulations using time-to-failure predicting lower strain-to-failure at low rates

CHAPTER 2

CODE VERIFICATION TESTS FOR NONLINEAR ELASTIC CONSTITUTIVE MODELS UNDER LARGE DEFORMATIONS

2.1 Abstract

Code verification against analytical solutions is a prerequisite to code validation against experimental data. Though solid-mechanics codes have established basic verification standards such as patch tests and convergence tests, few (if any) similar standards exist for testing solid-mechanics constitutive models under nontrivial massive deformations. Increasingly complicated verification tests for solid mechanics are presented, starting with simple patch tests of frame-indifference and traction boundary conditions under affine deformations, followed by two large-deformation problems that might serve as standardized verification tests suitable to quantify accuracy, robustness, and convergence of momentum solvers used in solid-mechanics codes. These problems use an accepted standard of verification testing, the method of manufactured solutions (MMS), which is rarely applied in solid mechanics. Body forces inducing a specified deformation are found analytically by treating the constitutive model abstractly, with a specific model introduced only at the last step in examples. One nonaffine MMS problem subjects the momentum solver and constitutive model to large shears comparable to those in penetration, while ensuring natural boundary conditions to accommodate codes lacking support for applied tractions. Two additional MMS problems, one affine and one nonaffine, include nontrivial traction boundary conditions.

2.2 Introduction

Computer simulations of physical events are now well integrated into engineering design and analysis processes, often offering the only means of decision making in problems that

---

K. Kamojjala, R. Brannon, A. Sadeghirad, and J. Guilkey, Verification tests in solid mechanics *Eng. Comput.*, 2013, 1-21. Reprinted with permission from Springer.

are too dangerous or expensive to explore directly in the laboratory or in full scale tests. Verification and validation (V&V) of computational codes that simulate physical events is critical to establish confidence and credibility in the methods, and the mathematical models used. Detailed (and now standardized) V&V definitions [79] and procedures are documented in [73, 74, 67, 65, 66, 51, 72, 76, 93, 5]. Code verification is continually accumulated evidence that the governing equations are solved correctly, and code validation is evidence that the governing equations themselves provide an acceptable description of the reality. Code verification can be used to test the implementation of numerical methods and the computational models that affect the accuracy and robustness of the code. With the multiphysics codes being so large, and consisting of many computational constitutive models, simple computer bugs, or intrinsically flawed algorithms in a simulation might go unnoticed unless aggressively searched for via code verification testing.

Different types of verification tests used by the scientific community include trend tests, symmetry tests, comparison tests, convergence studies, method of exact solutions (MES), and method of manufactured solutions (MMS) [51]. In MES, the source terms are chosen, and then the solution for the governing equation is derived using mathematical methods. In MMS, a solution is *manufactured*, and then the source terms are found by solving the partial differential equations backwards [51]. Specifically, for solid mechanics, MMS is the process of deriving the analytical body forces, tractions, and the initial conditions required to achieve a predetermined deformation field. These analytical solutions for the forcing functions are supplied as inputs to the codes, and error is then quantified by comparing the predicted and predetermined displacement and stress fields. "MMS can be applied in principle to any code, though of course some commercial codes make it difficult to modify to provide the necessary user-defined source terms." MMS has been extensively used in fluid mechanics [75, 93], electromagnetics [72], heat transfer [18], nuclear engineering [68], *etc.*, but very few MMS verification tests have been developed in solid mechanics. A simple 1D MMS for solids [7], straightforward 2D examples with stationary reference stretch directions and no material rotations [94, 82] constructed based on Ref [9], 2D examples under small strain setting, for elastic wave equations and for friction laws used in rupture dynamics [12, 4, 52] can be found in the literature. The advantage of the MMS is that it can expose a broader range of errors in the implementation of computational models and host codes compared to other forms of verification testing like single-element tests, patch tests, trend tests, *etc.* This chapter presents the following code verification tests for solid mechanics:

1. Frame-indifference of constitutive models, with special attention to strong objectivity

2. Homogeneous uniaxial strain MMS for traction boundary conditions

3. Generalized vortex MMS using nonlinear elastic constitutive model

4. Bending bar MMS using a nonlinear elastic constitutive model

All of these code verification problems focus on rate-independent constitutive models, where "time" defines the motion parametrically. These problems, therefore, may be run at high or low rates, making them appropriate for testing both dynamic and quasistatic codes. These problems are certainly suitable to test implementations of the finite-element method (FEM), but they are herein illustrated using the material point method (MPM) because this relatively new technique has only recently been emerging as an alternative to FEM for certain classes of problems. Accordingly, verification testing of the MPM is performed for its contemporary interest (especially to expose its algorithmic shortcomings rather than simply to catch coding bugs).

2.3 Frame-indifference verification test

The principle of material frame indifference (PMFI) requires the constitutive model to be self-consistent under superimposed rigid rotations and translations. PMFI demands the spatial tractions and stresses to rotate when the deformed material is rigidly rotated. While so-called objective rates are often used to satisfy frame indifference, Ref [70] demonstrated that numerical applications involving large rotations over a single time step (as might occur in penetration, ball milling, *etc.*) can satisfy frame indifference far more accurately through the use of polar Lie derivatives. This approach solves the constitutive model in an unrotated frame, after which the results are transformed back to the spatial frame. When run as an MES problem (*i.e.,* specifying the displacements of the boundary) this test will be illustrated herein to demonstrate that an approximation used in the implementations of strong objectivity (namely, neglecting changes in the pull-back or push-forward transformation tensor during the time step) results in failure to satisfy the PMFI. This problem may also be run as an MMS problem (*i.e.,* specifying tractions at the boundary) to test implementation of "follower force" pressure boundary conditions. The test problem is defined as follows:

- An initially cube-shaped element undergoes uniaxial strain (along the x-axis) from time $t = 0$ to $t = 1$. Being uniaxial strain, this problem is a special case of plane strain.

- This deformed element next undergoes superimposed rotation of 90° about the z-axis from time $t = 1$ to $t = 2$.

The exact solution during the second leg is given by:

$$\boldsymbol{\sigma} = \boldsymbol{R} \cdot \overline{\boldsymbol{\sigma}} \cdot \boldsymbol{R}^T \,, \tag{2.1}$$

where

$$\mathbf{R} = \begin{bmatrix} \cos\theta & -\sin\theta & 0 \\ \sin\theta & \cos\theta & 0 \\ 0 & 0 & 1 \end{bmatrix}, \qquad \text{and} \qquad \overline{\boldsymbol{\sigma}} = \begin{bmatrix} \sigma_A & 0 & 0 \\ 0 & \sigma_L & 0 \\ 0 & 0 & \sigma_L \end{bmatrix} . \tag{2.2}$$

$\overline{\boldsymbol{\sigma}}$ is the unrotated Cauchy stress, σ_A is the axial stress, σ_L is the lateral stress, and θ is the rotation angle equal to zero from $t = 0$ to $t = 1$ and equal to $\frac{\pi}{2}(t-1)$ thereafter. Substituting Eq. (2.2) into Eq. (2.1) results in

$$\boldsymbol{\sigma} = \begin{bmatrix} \sigma_A \cos^2\theta + \sigma_L \sin^2\theta & (\sigma_A - \sigma_L)\sin\theta\cos\theta & 0 \\ (\sigma_A - \sigma_L)\sin\theta\cos\theta & \sigma_L \cos^2\theta + \sigma_A \sin^2\theta & 0 \\ 0 & 0 & \sigma_L \end{bmatrix} . \tag{2.3}$$

This solution applies to any constitutive model, as long as σ_A and σ_L equal whatever their values would be without superimposed rotation. To illustrate, Fig. 2.1 shows the analytical solution for the time history of the stress components (normalized by peak stress) from Eq. (2.3) in the case of a linear-elastic rate-independent material. Regardless of the complexity of the constitutive model, the in-plane stress components must change during the second leg to account for the rotation of the principal directions of Cauchy stress.

This simple problem could – and should – be solved as part of basic testing of any finite-element code. However, the urgent need to verify more contemporary (emerging) computational solid-mechanics algorithms has motivated illustrating all verification tests herein using the open-source Uintah computational framework [34] except the examples discussed in Sec. 2.4 and Sec. 2.6 which were run using an in-house research MPM MATLAB code. "Uintah is a software system designed with fundamental chemistry and engineering physics fully coupled with nonlinear solvers to support highly dynamic physical processes"[34]. While lessons learned about Uintah are shared herein, each different code can be expected to have different underlying bugs or algorithmic errors causing a failure to pass this crucial pull-and-rotate test. In the case of Uintah testing, Fig. 2.2 shows a flawed stress update

---

While we here consider the superimposed rotation to be applied after the stretching, it is equally important to test for appropriate predictions when the stretching and rotation are applied simultaneously, including at various accelerations.

algorithm that had been initially used for a newly implemented constitutive model, which was designed (in principle) to satisfy frame indifference by applying the constitutive model in the unrotated (material) frame. Preliminary frame-indifference test results (Fig. 2.3) showed that the first implementation of the model failed this simplistic test. The symmetric part of velocity gradient is zero during the second leg, so the constitutive model correctly predicts no change in the unrotated stress. However, the unrotation/re-rotation operation applied in the host code failed to include a necessary update in the rotation tensor over the timestep. Even though changes in the rotation go to zero as the timestep goes to zero, this test revealed that the same rotation tensor must not be used for both the unrotation and re-rotation operations. Figures 2.4 and 2.5 show that the corrected algorithm passes this simple test.

This problem aimed to demonstrate consistent results between a baseline (fiducial) non-rotating uniaxial strain problem to the same problem with superimposed rotation applied to the spatial domain. These frame-indifference comparisons have the same *initial* configurations in both problems. A fundamentally different – equally important – verification test of any constitutive model likewise demonstrates consistency of predictions between a fiducial problem (horizontal stretching) and a comparison problem (angled stretching) in which the initial configuration in the comparison problem is rotated from the outset. This second type of test verifies basis indifference of tensor equations, which might perhaps catch implementation bugs in off-diagonal components of tensors. An outwardly expanding ring (with and without superimposed rotation), or any similar problem having cylindrical or spherical symmetry likewise can test a code's basis and frame indifference. Such testing has been recently demonstrated to be important in problems for which angled material boundaries are poorly approximated (as is common when importing computed tomography data into simulations without applying smoothing algorithms)[78].

2.4 Uniaxial strain MMS for traction boundary conditions

A manufactured solution is a predetermined time-varying field for the displacement, $\boldsymbol{u} = \boldsymbol{x} - \boldsymbol{X}$, of points initially located at position $\boldsymbol{X}$ to points $\boldsymbol{x}$ in the deformed configuration. Equivalently, noting that $\boldsymbol{x}$ varies with time t, an MMS prescribes the continuum mapping function $\boldsymbol{x} = \chi(\boldsymbol{X}, t)$. Development of a manufactured solution begins with a statement of the primary governing equation, which for continuum mechanics is Cauchy's first law of motion (*i.e.,* balance of momentum):

$$\mathrm{div}(\boldsymbol{\sigma}) + \rho \boldsymbol{b} = \rho \boldsymbol{a} \ , \tag{2.4}$$

where $\boldsymbol{\sigma}$ is Cauchy stress, ρ is the spatial mass density, $\boldsymbol{b}$ is the body force, $\boldsymbol{a}$ is the acceleration, and $\mathrm{div}\boldsymbol{\sigma}$ is the spatial divergence of stress. An MMS analysis first applies the constitutive model to infer the stress field associated with the prescribed deformation. Then this stress field is substituted into the momentum equation to determine the body force $\boldsymbol{b}$.

Given a predetermined and time-varying displacement field, the acceleration on the right-hand side of Eq. (2.4) can be evaluated by

$$\boldsymbol{a} = \left(\frac{\partial^2 \boldsymbol{x}}{\partial t^2} \right)_{\boldsymbol{X}} \ , \tag{2.5}$$

where the subscript emphasizes that $\boldsymbol{X}$ is held constant. Furthermore, an elastic constitutive model in solid mechanics gives stress as a function of strain, or, more generally for inelastic path-dependent media, the constitutive model gives stress as a functional of the strain history. In either case, knowing a predetermined displacement field is sufficient (though nontrivial) to determine the stress field and its divergence, thus allowing the body force to be found from Eq. (2.4). Below, we illustrate this process of deriving a manufactured solution for homogeneous uniaxial strain of a hyperelastic solid. Subsequent sections address more challenging prescribed deformations. In the absence of translation, the mapping for a homogeneous deformation of a point $\boldsymbol{X}$ in the initial configuration to $\boldsymbol{x}$ in the deformed configuration is given by

$$\boldsymbol{x} = \boldsymbol{F} \cdot \boldsymbol{X}, \tag{2.6}$$

where the deformation gradient tensor $\boldsymbol{F}$ varies with time, but not position. Accordingly, the acceleration in Eq. (2.5) is

$$\boldsymbol{a} = \ddot{\boldsymbol{F}} \cdot \boldsymbol{X} \ . \tag{2.7}$$

As an example, consider a deformation gradient that varies linearly through time from an initial value of $\boldsymbol{I}$ to a final value of $\boldsymbol{G}$ according to $\boldsymbol{F} = \boldsymbol{I}(1-t) + \boldsymbol{G}t$, where $\boldsymbol{G}$ characterizes the final deformed shape at the simulation stop time of $t = 1s$. For uniaxial strain corresponding to a final stretch Λ in the 1-direction, the component matrix for $\boldsymbol{G}$ is

$$\boldsymbol{G} = \begin{bmatrix} \Lambda & 0 & 0 \\ 0 & 1 & 0 \\ 0 & 0 & 1 \end{bmatrix} \ , \tag{2.8}$$

and therefore the component matrix for the time-varying deformation gradient is

$$\boldsymbol{F} = \begin{bmatrix} \phi(t) & 0 & 0 \\ 0 & 1 & 0 \\ 0 & 0 & 1 \end{bmatrix}, \quad \text{where} \quad \phi(t) = 1 + (\Lambda - 1)t \; . \tag{2.9}$$

Thus, for this example, $\ddot{\boldsymbol{F}} = \boldsymbol{0}$, which is a zero tensor and hence, the material acceleration is zero.

For a homogeneous material, the constitutive model and its associated parameters are the same at all points in space. Accordingly, for a homogeneous deformation, the stress predicted by the constitutive model is the same at all points in space, making the divergence of stress zero. Thus, with both the acceleration and stress divergence zero, Eq. (2.4) implies that the body force must be zero.

Though the body force is zero, the initial velocity field, $\boldsymbol{v} = \dot{\boldsymbol{F}} \cdot \boldsymbol{X}$, is nonzero (so this problem offers a simple test for initializing velocity fields in a code). Also, boundary traction is given by $\boldsymbol{t} = \boldsymbol{\sigma} \cdot \boldsymbol{n}$, where $\boldsymbol{\sigma}$ is the Cauchy stress and $\boldsymbol{n}$ is the unit outward normal. To evaluate the analytical tractions, suppose that a simple Neo-Hookean constitutive model,

$$\boldsymbol{\sigma} = \frac{\lambda \log[J]}{J} \boldsymbol{I} + \frac{\mu}{J} [\boldsymbol{F} \cdot \boldsymbol{F}^T - \boldsymbol{I}] \tag{2.10}$$

is adopted. Here λ and μ are the elastic Lamé material constants. Substituting $\boldsymbol{F}$ from Eq. (2.9) into Eq. (2.10) gives stress as a function of stretch Λ and time t, from which application of $\boldsymbol{t} = \boldsymbol{\sigma} \cdot \boldsymbol{n}$ gives tractions on the four faces of a 2D rectangular domain as follows

$$\boldsymbol{t}_1 = -\boldsymbol{t}_2 = \left[\frac{\lambda \ln(\Lambda t - t + 1) + \mu((\Lambda t - t + 1)^2 - 1)}{(\Lambda t - t + 1)} \right] \mathbf{E}_1 \; , \tag{2.11}$$

$$\boldsymbol{t}_3 = -\boldsymbol{t}_4 = \left[\frac{\lambda \ln(\Lambda t - t + 1)}{(\Lambda t - t + 1)} \right] \mathbf{E}_2 \; , \tag{2.12}$$

where $\boldsymbol{t}_1$ is the traction on the positive x-face, $\boldsymbol{t}_2$ is the traction on negative x-face, $\boldsymbol{t}_3$ is the traction on the positive y-face and $\boldsymbol{t}_4$ is the traction on the negative y-face.

Young's modulus and Poisson's ratio are 10^6Pa and 0.25, respectively, while the stop time of the simulation is $T = 1s$; *i.e.,* $0 \leq t \leq T$. Figure 2.6(b) shows the deformed configuration of the initial unit square (Fig. 2.6(a)) at the end of the simulation that was run using an in-house research MPM MATLAB code to test this MMS using a traction boundary condition option that had never been previously verified for large-deformation applications. The initial results exhibited a nonzero lateral strain (*i.e.,* a contraction in the y-direction) which contradicted the manufactured solution and therefore exposed a limitation of the

existing traction boundary condition option. Mesh refinement did not eliminate this error. Code inspection revealed that discretized force applied to each boundary particle had been calculated based on the pressure times the *initial* cross-sectional area, so this test demonstrated the need for the code to be modified to update the area in response to deformation. In general, the updated area element vector $\mathrm{d}\boldsymbol{A}$ is related to the initial area vector $\mathrm{d}\boldsymbol{A}_0$ according to Nanson's relation [57],

$$\mathrm{d}\boldsymbol{A} = J\boldsymbol{F}^{-T} \cdot \mathrm{d}\boldsymbol{A}_0 \ . \tag{2.13}$$

Applied to this problem, this equation merely indicates that the force applied to each boundary particle must increase with axial strain to maintain a constant boundary pressure. Implementing appropriate code revisions resulted in a much improved result showing very little anomalous lateral contraction, but then some error remained evident at the corners of the domain, thus exposing the need for revision of the traction algorithm where surfaces intersect. After both corrections were implemented, the manufactured displacement field was reproduced exactly, as shown in Figure 2.7(b). Though simple, this manufactured solution thus proved to be crucial to identify limitations of the existing traction boundary conditions and to subsequently extend that feature to allow large deformations. As with any verification test, a natural subsequent test would be to run the same problem at an angle and with superimposed rotation.

2.5 Generalized vortex verification test

This verification test uses the method of manufactured solutions to derive analytical solutions for the initial conditions, body forces, and tractions required to induce a deformation field for which all points in the domain are subjected to varying levels of simple shear with superimposed rotation. The problem domain is a ring of inner radius a and outer radius b, as shown in Fig. 2.8. This manufactured solution has zero displacements and (to achieve traction-free boundaries) zero displacement gradients at the inner and outer radii. Since material moves along circular paths only in the interior of the ring (see Fig. 2.9), this problem may be alternatively regarded to apply on a square domain for which material outside the ring is prescribed to be stationary. This problem simultaneously confirms basis and frame indifference.

Even though the displacement field for this problem is more complicated than other MMS problems in the solid-mechanics literature, the nature of the local deformation is everywhere and at all times simple shear with superimposed rotation, thus making this problem a good candidate for general constitutive model testing since the model response

must be determined analytically (or in tabular form) for only a single loading mode. Details of the derivation are provided in Sec. 2.8.1, allowing this section to focus exclusively on stating the equations necessary to run and assess this problem in any host code.

2.5.1 Numerical simulation of the MMS on a ring domain

The constitutive model selected to illustrate the solution is the following simple Neo-Hookean model:

$$\boldsymbol{\sigma} = \frac{\lambda \log[J]}{J}\mathbf{I} + \frac{\mu}{J}[\mathbf{F}\cdot\mathbf{F}^T - \mathbf{I}] \,, \tag{2.14}$$

where, λ and μ are the elastic Lamé material constants, J is the Jacobian of the deformation gradient tensor $\mathbf{F}$, and $\mathbf{I}$ is the identity tensor. The initial density, Young's modulus and Poisson's ratio are chosen to be $\rho_o = 1000\frac{kg}{m^3}$, 10^3Pa and 0.3, respectively, (corresponding to $\lambda = 577$Pa and $\mu = 385$Pa). The inner and outer radii are 0.75m and 1.25m, respectively. The stop time of the simulation is $T = 1s$; *i.e.,* $0 \leq t \leq T$. The initial condition is zero displacement and zero velocity everywhere. The deformation field is plane strain. As explained in Sec. 2.8.1, the components of the body force may be evaluated at any location (x, y) by the following sequence of calculations (see algorithm 1). The peak amplitude of rotation, $A = 1$ radian. This manufactured solution was implemented in the open-source Uintah MPM framework [34]. The results using two integrator options (called uGIMP [8] and CPDI [77]) are presented.

As seen in Figs. 2.10 and 2.11, the simulation becomes unstable for this code's uGIMP option, while remaining stable for the CPDI option. Even though the CPDI method gives superior results in comparison to all predecessor MPM methods, its final configuration, shown in Fig. 2.12 (which for the exact solution should coincide with the initial configuration), still shows clear evidence of mesh and/or particle distribution texture bias because it is not circular in shape. This was further investigated by creating a ring domain with the particles conforming to the boundary as shown in Fig. 2.13, and the improved final shape can be seen in Fig. 2.14.

2.5.2 Numerical simulation of the MMS on a square domain

Generalized vortex MMS can be also applied on a square domain since the material motion occurs only in the interior of the ring, and material outside the ring is prescribed to be stationary.

Algorithm 1 Generalized vortex MMS

1: Initialize the velocity and displacement to zero at time $t = 0$.
2: Evaluate $R = \sqrt{X^2 + Y^2}$. Since all material motion is circular, this also equals the deformed radius.
3: Evaluate $\Theta = ArcTan[X, Y]$ where the two-argument arc-tangent must be used.
4: Evaluate $p_1 = \frac{4096R\left(15-47R+48R^2-16R^3\right)^2 \mu \sin^4(\pi t)}{\rho_0}$ ▷ temporary variable
5: Evaluate $p_2 = \pi^2 R \left(15 - 32R + 16R^2\right)^4 \sin(2\pi t)^2$ ▷ temporary variable
6: Evaluate $p_3 = -16\left(-45 + 188R - 240R^2 + 96R^3\right)$ ▷ temporary variable
7: Evaluate $p_4 = \left(-45 + 188R - 240R^2 + 96R^3\right)$ ▷ temporary variable
8: Evaluate $p_5 = \left(15 - 32R + 16R^2\right)^2$ ▷ temporary variable
9: Evaluate $b_r = p_1 - p_2$ ▷ Radial component of the body force
10: Evaluate $b_\theta = \frac{2\mu p_3 + 2\cos(2\pi t)\left(16\mu p_4 + \pi^2 R \rho_0 p_5\right)}{\rho_0}$ ▷ Tangential component of the body force
11: Evaluate the rotation angle $\alpha = \frac{A(1-cos(2\pi t))(1-32(R-1)^2+256(R-1)^4)}{2}$
12: Evaluate the deformed angular coordinate $\theta = \Theta + \alpha$
13: Evaluate $b_x = b_r \cos(\theta) - b_\theta \sin(\theta)$ ▷ x-component of the body force
14: Evaluate $b_y = b_r \sin(\theta) + b_\theta \cos(\theta)$ ▷ y-component of the body force
15: Set the z component of the body force $b_z = 0$ if the simulation is run in $3D$

This section provides the results of the numerical simulation of the generalized vortex problem when run on a square domain using CPDI and uGIMP. Figures 2.15–2.18 show color plots of displacement near the peak rotation angle and the final shapes using CPDI and uGIMP, respectively. The final shapes clearly show the advantage of CPDI over uGIMP. This problem illustrates the potential of the uGIMP integrator to produce spurious numerical fracture, which might have otherwise been incorrectly seen as a physical prediction in a validation simulation (*e.g.,* penetration).

Thus, this problem reiterates the importance of delaying validation assessments until the model is demonstrated to pass verification tests in loading modes similar to the application (in our case, large shears in penetration).

2.5.3 Convergence study

This section compares spatial convergence studies for displacement of the generalized vortex problem on the ring domain (with and without particles conforming with the boundary) and on the square domain. Following Wallstedt *et al.* [94], a temporal convergence study was performed independently, and the smallest CFL number (0.05) in our temporal convergence simulations were used for all the subsequent spatial convergence studies discussed in this section. As indicated by Wallstedt *et al.*, this choice is made to ensure that errors in the spatial convergence study are attributable to the spatial resolution, not the time integrator. The spatial L_2 error is defined by

$$L_2 \text{ error} = \sqrt{\frac{\sum_{N_p} \parallel \mathbf{u}_{\text{exact}}(\boldsymbol{x}_p, t) - \mathbf{u}_{\text{app}}(\boldsymbol{x}_p, t) \parallel^2}{N_p}} \,, \tag{2.15}$$

where $\mathbf{u}_{\text{exact}}(x_p, t)$ and $\mathbf{u}_{\text{app}}(x_p, t)$ are, respectively, the analytical and calculated displacement vectors at the p^{th} particle position $\boldsymbol{x}$, and N_p is total number of particles in the domain. To have a fair comparison of error for both the square domain and ring domain, the error in the square domain was calculated only for the particles that lie in the circular domain. Figure 2.19 compares the convergence for a peak amplitude of 1 radian. The L_2 error is calculated at the end of the simulation t=1 s.

Sensitivity of the peak amplitude on the convergence was also studied. Figure 2.20 shows the comparison for both the ring and square domain for various peak amplitudes. The results show poor convergence using uGIMP for both the ring and the square domain, as the simulation is unstable for this peak amplitude. It can be concluded that, as the peak amplitude of displacement is reduced and the mesh is refined, the uGIMP and CPDI converge to the same solution. In other words, the uGIMP integrator is convergent in

small deformations, but it fails verification testing in large deformations. Interestingly, and disturbingly, the uGIMP method nevertheless continues to be used routinely in large deformation problems because it tends to be more robust (*i.e.,* it will still provide an answer). Similar problems of spurious numerical fracture are known to affect other particle methods, like smoothed-particle hydrodynamics [63], whenever particles separate without a concomitant extension of the support domains of their associated basis functions.

2.6 Bending bar verification test

The problem domain is a rectangular bar with height H and base B. This problem is similar to the generalized vortex problem in the sense that all material points undergo an identical deformation mode: uniaxial strain with superimposed rotation, as seen in Fig. 2.21. Unlike the generalized vortex, this problem also includes a time and space-varying traction on the boundary, thus giving this problem the advantage of assessing the code's algorithms for geometrically nonlinear traction boundary conditions under nonhomogeneous deformations. The analytical solutions are detailed in Sec. 2.8.2.

The constitutive model is the same Neo-Hookean model given by

$$\boldsymbol{\sigma} = \frac{\lambda \log[J]}{J}\mathbf{I} + \frac{\mu}{J}[\mathbf{F}\cdot\mathbf{F}^T - \mathbf{I}] \,, \tag{2.16}$$

where λ is the Lame modulus, μ is the shear modulus, J is the Jacobian of the deformation gradient tensor $\mathbf{F}$ and $\mathbf{I}$ is the identity tensor. The initial density is chosen to be $\rho_o = 1000\frac{kg}{m^3}$, Young's modulus and Poisson's ratio are chosen to be 10^3Pa and 0.3, respectively, (corresponding to $\lambda = 577$Pa and $\mu = 385$Pa). The height H of the bar is chosen to be 8m and base B is 1m. The stop time of the simulation is $T = 1s$ *i.e.,* $0 \leq t \leq T$. As explained in Sec. 2.8.2, the components of the body force may be evaluated at any location (x, y) by the sequence of calculations shown in algorithm 2.

Tractions are evaluated by the sequence of calculations shown in algorithm 3. The peak amplitude A was chosen to be $\frac{\pi}{2}$, and the simulations were run using an in-house research MPM MATLAB code. The snapshots of the deformation during the loading and the unloading phase can be seen in Figs. 2.22–2.23, respectively. Figure 2.24 shows the spatial convergence plot for a peak amplitude of $\frac{\pi}{2}$. The L_2 error (defined by Eq. (5.13)) is calculated at the end of the simulations *i.e.,* t =1 sec. The spatial convergence plot shows a decrease in error as the mesh resolution is increased, with the rate of convergence close to 1.2. Ref [56] indicated that "the MPM algorithm inherits the conservation properties of the grid solution." This was indeed observed in [78] using an energy norm. Above, we use a different norm and hence, different rate of convergence.

Algorithm 2 Body forces in bending bar MMS

1: Initialize the velocity and displacement to zero at time $t = 0$
2: Evaluate an amplitude function $\beta(t) = \frac{A\left(1-\cos\left(\frac{2\pi t}{T}\right)\right)}{2}$
3: Evaluate the element rotation angle $\alpha(t) = \frac{\beta(t)X_2}{H}$, where X_2 is the initial Y-coordinate of the element
4: Evaluate $p_1 = 128H^3 - 8A^2HX_2{}^2 - 5A^3X_1X_2^2 +$
$4\left(16H^3 + A^2HX_2^2 + A^3X_1X_2^2\right)\cos(2\pi t)$ ▷ temporary variable
5: Evaluate $p_2 = 4A^2(2H + AX_1)X_2^2\cos(4\pi t) - 4A^3X_1X_2^2\cos(6\pi t) + A^3X_1X_2^2\cos(8\pi t)$ ▷ temporary variable
6: Evaluate $p_3 = -128H^3\cos\left(\frac{AX_2\sin(\pi t)^2}{H}\right) -$
$32H^3\cos\left(2\pi t - \frac{AX_2\sin(\pi t)^2}{H}\right)$ ▷ temporary variable
7: Evaluate $p_4 = -32H^3\cos\left(2\pi t + \frac{AX_2\sin(\pi t)^2}{H}\right)$ ▷ temporary variable
8: Evaluate $p_5 = \frac{A\left(1+\frac{AX_1(1-\cos(2\pi t))}{2H}\right)}{2H\rho_0(2H+AX_1-AX_1\cos(2\pi t))^2}$ ▷ temporary variable
9: Evaluate $p_6 = -8H^2\lambda + 8AH\mu X_1 + 3A^2\mu X_1^2 - 4A\mu X_1(2H + AX_1)\cos(2\pi t)$ ▷ temporary variable
10: Evaluate $p_7 = A^2\mu X_1^2\cos(4\pi t) + 8H^2\lambda\log\left(1 + \frac{AX_1\sin(\pi t)^2}{H}\right)$ ▷ temporary variable
11: Evaluate $p_8 = -12AHX_2 - 4A^2X_1X_2 + A(8H + 7AX_1)X_2$
$\cos(2\pi t) + 4A(H - AX_1)X_2\cos(4\pi t)$ ▷ temporary variable
12: Evaluate $p_9 = A^2X_1X_2\cos(6\pi t) + 32H^2\sin\left(\frac{AX_2\sin(\pi t)^2}{H}\right)$ ▷ temporary variable
13: Evaluate $p_{10} = -8H^2\sin\left(2\pi t - \frac{AX_2\sin(\pi t)^2}{H}\right) +$
$8H^2\sin\left(2\pi t + \frac{AX_2\sin(\pi t)^2}{H}\right)$ ▷ temporary variable
14: Evaluate $b_r = \frac{\pi^2\csc(\pi t)^4(p_1+p_2+p_3+p_4)}{32AH^2} + p_5(p_6 + p_7)$ ▷ Radial component of the body force
15: Evaluate $b_\theta = \frac{\pi^2\csc(\pi t)^4(p_8+p_9+p_{10})}{8AH}$ ▷ Tangential component of the body force
16: Evaluate $b_x = b_r\cos(\alpha) - b_\theta\sin(\alpha)$ ▷ x-component of the body force
17: Evaluate $b_y = b_r\sin(\alpha) + b_\theta\cos(\alpha)$ ▷ y-component of the body force
18: Set the z component of the body force $b_z = 0$ if the simulation is run in $3D$

Algorithm 3 Tractions in bending bar MMS

1: Evaluate $\beta(t) = \frac{A\left(1-\cos\left(\frac{2\pi t}{T}\right)\right)}{2}$
2: Evaluate $\alpha(t) = \frac{\beta(t)X_2}{H}$
3: Evaluate $\Lambda(t) = 1 + \frac{\beta(t)X_1}{H}$, where X_1 is the initial X-coordinate of the element, and H is the height of the bar
4: Evaluate the stretch tensor $\boldsymbol{U} = \begin{bmatrix} 1 & 0 \\ 0 & \Lambda \end{bmatrix}$
5: Evaluate the Jacobian $J = \det(\boldsymbol{U})$
6: Evaluate the constitutive model in the unrotated frame $\overline{\boldsymbol{\sigma}} = \frac{\lambda\log[J]}{J}\mathbf{I} + \frac{\mu}{J}[\boldsymbol{U}^2 - \mathbf{I}]$
7: Evaluate the orthogonal rotation tensor $\boldsymbol{Q} = \begin{bmatrix} \cos(\alpha) & -\sin(\alpha) \\ \sin(\alpha) & \cos(\alpha) \end{bmatrix}$
8: Evaluate the tractions on each face of the bar using $\boldsymbol{t} = \boldsymbol{Q}\cdot\overline{\boldsymbol{\sigma}}\cdot\boldsymbol{N}$, where $\boldsymbol{N}$ is unit outward normal on each face in the reference frame

2.7 Conclusions

This chapter has presented a sequence of code verification tests of increasing complexity appropriate for benchmarks of solid-mechanics codes. Specifically, the verification tests and their key conclusions are summarized as follows:

1. A simple uniaxial-strain frame-indifference verification test revealed that an approximation used in the implementations of strong objectivity (namely neglect of rotation increments during the step) results in failure to satisfy the PMFI. Different polar rotation tensors need to be used for different operations in the stress update algorithm.

2. A homogeneous uniaxial strain patch test was designed using the method of manufactured solutions. This problem has *pure tractions with no external body forces*, and hence can be used to verify the implementation of a code's traction boundary conditions in a relatively simple context.

3. A relatively complicated generalized-vortex manufactured solution was derived to produce pure circular motion of all particles, and therefore all material elements are subjected to a state of simple shear with superimposed rotation. The angular displacement function was designed to provide the simplification that the initial conditions were quiescent (zero displacement and zero velocity) and the boundary conditions were traction free. In other words, this problem has a forcing function exclusively provided by external body forces. This problem simultaneously confirms basis and frame indifference. The extension of this problem to a square domain makes it a good candidate to test Eulerian codes as well. A convergence study was performed on both a ring-shaped and square domain to reveal advantages of a new material point method integrator [77] over predecessor methods. This problem also revealed errors associated with poor (stair-stepped) descriptions of angled boundaries, which are often adopted in mesoscale validation simulations of imported computed tomography data without requisite evidence of verification. The importance of boundary smoothing appears to be recognized in the biomechanics community [53], but is relatively unrecognized elsewhere in mechanics.

4. A bending bar problem was developed that, like the generalized vortex, involved all points in the domain undergoing identical deformation modes, which for this problem was uniaxial strain with superimposed rotation. This problem also simultaneously tests basis and frame indifference. This problem is slightly more complicated than

the generalized vortex in the sense that it has both external body forces and applied tractions.

2.8 Analytical derivations of forcing functions

2.8.1 Derivation of analytical forcing functions for generalized vortex problem

The dynamic equation of motion is:

$$\mathrm{DIV}(\mathbf{P}) + \rho_o \mathbf{b} = \rho_o \mathbf{a} \ , \tag{2.17}$$

where $\mathbf{a}$ is the acceleration, $\mathbf{b}$ is the body force, $\mathbf{P}$ is the first-Piola Kirchhoff (PK1) stress, ρ_o is the initial density, and $\mathrm{DIV}(\mathbf{P})$ is the backwards reference divergence of $\mathbf{T}$, defined with respect to the Cartesian basis $(\mathbf{E}_1, \mathbf{E}_2, \mathbf{E}_3)$ by

$$\mathrm{DIV}(\mathbf{P}) = \frac{\partial P_{ij}}{\partial X_j}\mathbf{E}_i = \frac{\partial \mathbf{P}}{\partial \mathbf{X}} : \mathbf{I} \ , \tag{2.18}$$

where ":" is the second-order tensor inner product, and $\mathbf{I}$ is the second-order identity tensor. The problem domain is a ring of inner radius a and outer radius b, as shown in Fig. 2.25. The upcoming manufactured solution will have zero displacements and (to achieve traction-free boundaries) zero displacement gradients at the inner and outer radii. Thus, since material motion will occur only in the interior of the ring, this problem may be also regarded to apply on a square domain for which material outside the ring is prescribed to be stationary. This problem involves pure circular motion of all particles. The angular displacement varies with the radial coordinate, thus inducing simple shear with superimposed rotation at all times and at all spatial locations.

For plane strain circular particle motion, the mapping from the initial position $\mathbf{X}$ to the current position $\mathbf{x}$ is given by

$$\mathbf{x} = \mathbf{Q} \cdot \mathbf{X}. \tag{2.19}$$

Here, $\mathbf{Q}$ is the orthogonal tensor with components

$$\mathbf{Q} = \begin{bmatrix} \cos\alpha & -\sin\alpha & 0 \\ \sin\alpha & \cos\alpha & 0 \\ 0 & 0 & 1 \end{bmatrix} \ , \tag{2.20}$$

where α is the rotation angle, which varies with time and radial coordinate R but not with angular coordinate Θ. Specifically,

$$\alpha(R,t) = g(t)h(R) \tag{2.21}$$

where, $g(t)$ controls the amplitude of the deformation, and $h(R)$ is a function (having a peak amplitude of unity) that defines the relative radial variation of the rotation angle.

The $h(R)$ function is selected in a way to ensure that material motion occurs only between the inner and outer radii, a and b. Thus, $h(R) = 0$ for $R < a$ and $R > b$. For continuous displacements, this implies that $h(a) = h(b) = 0$. Moreover, choosing $h'(a) = h'(b) = 0$ ensures zero strain (and hence zero traction) at the boundaries, which is termed a "natural" boundary condition because it is the default boundary condition in most momentum solvers (requiring no special handling in the algorithm). The goal of the ensuing analysis is to find the spatially varying body force field $\mathbf{b}(R, \Theta)$ necessary to produce this motion.

To begin the analysis, the following lemmas are useful: for any scalar s,

$$\frac{d\mathbf{Q}}{ds} = \frac{d\mathbf{Q}}{d\alpha}\frac{d\alpha}{ds} = \mathbf{A}\cdot\mathbf{Q}\frac{d\alpha}{ds}\ , \tag{2.22}$$

where $\mathbf{A}$ is the axial tensor associated with the rotation axis. Namely,

$$\mathbf{A} = \begin{bmatrix} 0 & -1 & 0 \\ 1 & 0 & 0 \\ 0 & 0 & 0 \end{bmatrix}. \tag{2.23}$$

The axial tensor has the important property that, for any vector $\mathbf{w}$,

$$\mathbf{A}\cdot\mathbf{w} = \mathbf{E}_z \times \mathbf{w}\ , \tag{2.24}$$

where $\mathbf{E}_z$ is the unit cylindrical base vector along the axis of rotation. Thus, for example, noting that the position vector is $\mathbf{X} = R\ \mathbf{E}_R$,

$$\mathbf{A}\cdot\mathbf{X} = \mathbf{E}_z \times (R\ \mathbf{E}_R) = R\ \mathbf{E}_\Theta\ . \tag{2.25}$$

The following sections provide steps for determining the deformation gradient $\mathbf{F}$, divergence of the PK1 stress DIV($\mathbf{T}$), and acceleration $\mathbf{a}$ required to ultimately solve (2.17) for the body force.

2.8.1.1 Deformation gradient and divergence of PK1 stress

Differentiating (2.21), the gradient of the rotation angle is given by

$$\frac{d\alpha}{d\mathbf{X}} = g(t)\frac{dh}{dR}\frac{dR}{d\mathbf{X}} = g(t)h'(R)\mathbf{E}_R. \tag{2.26}$$

The deformation gradient is found by taking the derivative of (2.19)

$$\mathbf{F} = \frac{d\mathbf{x}}{d\mathbf{X}} = \mathbf{Q} + \mathbf{X}\cdot\frac{d\mathbf{Q}^T}{d\alpha}\frac{d\alpha}{d\mathbf{X}}. \tag{2.27}$$

Using (2.22),(2.26), (2.25), and the fact that $\mathbf{Q}^T\cdot\mathbf{A}\cdot\mathbf{Q} = \mathbf{A}$, we have

$$\mathbf{F} = \mathbf{Q}\cdot\left[\mathbf{I} + R\ g(t)h'(R)\ \mathbf{E}_\Theta\mathbf{E}_R\right]. \tag{2.28}$$

The terms in the brackets represent a state of simple shear in the Θ direction with the shear plane tangent to the circumference. The multiplication by $\mathbf{Q}$ represents additional superimposed rotation into the current configuration. Let

$$2\ \xi(R) = R\ h'(R). \tag{2.29}$$

Then the shear strain is given by

$$\epsilon(t, R) = g(t)\ \xi(R). \tag{2.30}$$

The deformation gradient in (2.28) may be written as

$$\mathbf{F} = \mathbf{Q} \cdot \mathbf{q} \cdot \mathscr{F} \cdot \mathbf{q}^T\ , \tag{2.31}$$

where

$$\mathscr{F} = \mathbf{I} + 2\epsilon(t, R)\mathbf{E}_2\mathbf{E}_1 \qquad \text{and} \qquad \mathbf{q} = \begin{bmatrix} \cos\Theta & -\sin\Theta & 0 \\ \sin\Theta & \cos\Theta & 0 \\ 0 & 0 & 1 \end{bmatrix}. \tag{2.32}$$

Note that

$$\mathbf{F} = \mathbf{r} \cdot \mathscr{F} \cdot \mathbf{q}^T \qquad \text{where} \qquad \mathbf{r} = \begin{bmatrix} \cos\theta & -\sin\theta & 0 \\ \sin\theta & \cos\theta & 0 \\ 0 & 0 & 1 \end{bmatrix}. \tag{2.33}$$

Here, $\theta = \Theta + \alpha = \Theta + g(t)h(R)$, which is the angular coordinate of the particle in the deformed configuration. Note that $\mathscr{F}$ is an angle-independent "baseline" deformation representing simple shear without superimposed rotation. Further note that $\frac{d\mathscr{F}}{dR} = 2g(t)\xi'(R)\mathbf{E}_2\mathbf{E}_1$. Also, $\mathbf{q}$ is independent of R, and $\frac{d\mathbf{q}}{d\Theta} = \mathbf{A} \cdot \mathbf{q}$. The tensor $\mathbf{r}$ depends only on the deformed angular coordinate, but (since the deformed angle varies with radial coordinate), this tensor implicitly depends on both angular and radial coordinates. Thus, applying the chain rule,

$$\frac{d\mathbf{r}}{d\theta} = \mathbf{A} \cdot \mathbf{r}; \quad \left(\frac{\partial \mathbf{r}}{\partial \Theta}\right)_R = \mathbf{A} \cdot \mathbf{r}; \quad \left(\frac{\partial \mathbf{r}}{\partial R}\right)_\Theta = g(t)h'(R)\mathbf{A} \cdot \mathbf{r}\ , \tag{2.34}$$

where subscripts are used to indicate what is held constant in partial derivatives. Let S denote the second-Piola Kirchhoff (PK2) stress associated with the deformation $\mathscr{F}$. Then, for an isotropic material, it follows that the PK2 stress $\mathbf{S}$ associated with $\mathbf{F}$ must be

$$\mathbf{S} = \mathbf{q} \cdot S \cdot \mathbf{q}^T\ . \tag{2.35}$$

The first Piola-Kirchhoff (PK1) stress associated with deformation $\mathbf{F}$ is then

$$\mathbf{P} = \mathbf{F} \cdot \mathbf{S} = \mathbf{Q} \cdot \mathbf{q} \cdot \boldsymbol{\tau} \cdot \mathbf{q}^T = \mathbf{r} \cdot \boldsymbol{\tau} \cdot \mathbf{q}^T \ , \tag{2.36}$$

where $\boldsymbol{\tau} = \mathscr{F} \cdot S$ is the PK1 stress associated with the baseline deformation $\mathscr{F}$, which depends on R indirectly through dependence of the shear strain on R, but this baseline PK1 stress is not dependent on the angular coordinate. Thus

$$\left(\frac{\partial \boldsymbol{\tau}}{\partial R}\right)_t = \frac{d\boldsymbol{\tau}}{d\epsilon}\left(\frac{\partial \epsilon}{\partial R}\right)_t = \frac{d\boldsymbol{\tau}}{d\epsilon} g(t)\xi'(R). \tag{2.37}$$

The reference gradient of PK1 stress is a third-order tensor given by

$$\left(\frac{\partial \mathbf{P}}{\partial \mathbf{X}}\right)_t = \left(\frac{\partial \mathbf{P}}{\partial R}\right)_{\Theta,t} \mathbf{E}_R + \frac{1}{R}\left(\frac{\partial \mathbf{P}}{\partial \Theta}\right)_{R,t} \mathbf{E}_\Theta \ , \tag{2.38}$$

where the terms on the right-hand side are multiplied dyadically. Using (2.36), (2.34), and the chain rule, this equation becomes

$$\left(\frac{\partial \mathbf{P}}{\partial \mathbf{X}}\right)_t = \left(g(t)h'(R)\ \mathbf{A}\cdot\mathbf{P} + g(t)\xi'(R)\ \mathbf{r}\cdot\frac{d\boldsymbol{\tau}}{d\epsilon}\cdot\mathbf{q}^T\right)\mathbf{E}_R + \frac{1}{R} (\mathbf{A}\cdot\mathbf{P} + \mathbf{P}\cdot\mathbf{A}^T)\mathbf{E}_\Theta. \tag{2.39}$$

Referring to (2.18), recognizing that $\mathbf{q}^T \cdot \mathbf{E}_R = \mathbf{E}_1$, and using (2.24) to note that $\mathbf{A}^T \cdot \mathbf{E}_\Theta = \mathbf{E}_R$, the reference divergence of PK1 stress is given by

$$\mathrm{DIV}(\mathbf{P}) = \rho_o(\mathbf{a}-\mathbf{b}) = g(t)\ h'(R)\mathbf{A}\cdot\mathbf{P}\cdot\mathbf{E}_R + g(t)\ \xi'(R)\ \mathbf{r}\cdot\frac{d\boldsymbol{\tau}}{d\epsilon}\cdot\mathbf{E}_1 + \frac{1}{R}(\mathbf{A}\cdot\mathbf{P}\cdot\mathbf{E}_\Theta + \mathbf{P}\cdot\mathbf{E}_R). \tag{2.40}$$

In terms of the deformed angular coordinate θ, the spatial cylindrical base vectors are

$$\mathbf{e}_r = \cos(\theta)\mathbf{E}_1 + \sin(\theta)\mathbf{E}_2 \ , \qquad \mathbf{e}_\theta = -\sin(\theta)\mathbf{E}_1 + \cos(\theta)\mathbf{E}_2. \tag{2.41}$$

Dotting (2.40) by these spatial cylindrical base vectors, the spatial cylindrical components of the divergence of PK1 stress are given by

$$\rho_o(a_r - b_r) = \left(\xi'(R)\ \frac{d\tau_{11}}{d\epsilon} - h'(R)\ \tau_{21}\right)\ g(t) + \frac{1}{R}(\tau_{11}-\tau_{22}) \ , \tag{2.42}$$

$$\rho_o(a_\theta - b_\theta) = \left(\xi'(R)\ \frac{d\tau_{21}}{d\epsilon} + h'(R)\ \tau_{11}\right)\ g(t) + \frac{1}{R}(\tau_{12}+\tau_{21}). \tag{2.43}$$

The key advantage of the above result is that it is expressed in terms of Cartesian components of the PK1 stress corresponding to a baseline homogeneous simple shear, thus requiring the constitutive model to be evaluated only for that special case. The introduction of a specific constitutive model is avoided (for now) so that this result applies to any elastic model or for an inelastic model if no unloading is applied.

2.8.1.2 Velocity and acceleration

Using (2.19), (2.21) and (2.22), the velocity and acceleration of any given material particle are

$$\mathbf{v} = \dot{\mathbf{Q}} \cdot \mathbf{X} = g'(t)h(R)\ \mathbf{A} \cdot \mathbf{x} = R\ \omega\ \mathbf{e}_\theta\ , \tag{2.44}$$

$$\mathbf{a} = g''(t)h(R)\ \mathbf{A} \cdot \mathbf{x} - (g'(t)h(R))^2\mathbf{x} = R\ \dot{\omega}\ \mathbf{e}_\theta - R\ \omega^2\ \mathbf{e}_r\ , \tag{2.45}$$

where

$$\omega = g'(t)h(R) \qquad \text{and} \qquad \dot{\omega} = g''(t)h(R). \tag{2.46}$$

2.8.1.3 Body force

The body force vector is given by

$$\mathbf{b} = b_r\mathbf{e}_r + b_\theta\mathbf{e}_\theta. \tag{2.47}$$

Using (2.42), (2.43), (2.45), and (2.46), the spatial cylindrical components of the body force are

$$b_r = -R\ (g'(t)h(R))^2 - \frac{1}{\rho_o}\left[(\xi'[R]\ \frac{d\tau_{11}}{d\epsilon} - h'[R]\ \tau_{21})g(t) + \frac{1}{R}(\tau_{11} - \tau_{22})\right], \tag{2.48}$$

$$b_\theta = -R\ (g''(t)h(R)) - \frac{1}{\rho_o}\left[(\xi'[R]\ \frac{d\tau_{21}}{d\epsilon} + h'[R]\ \tau_{11})g(t) + \frac{1}{R}(\tau_{12} + \tau_{21})\right]. \tag{2.49}$$

The Cartesian components are obtained by substituting (2.41) into (2.47).

2.8.2 Derivation of analytical forcing functions for bending bar problem

The equation of motion in terms of Cauchy stress is given by:

$$\mathrm{div}\boldsymbol{\sigma} + \rho\mathbf{b} = \rho\mathbf{a}\ , \tag{2.50}$$

where $\mathbf{a}$ is the acceleration, $\mathbf{b}$ is the body force, $\boldsymbol{\sigma}$ is the Cauchy stress, ρ_o is the initial density, and $\mathrm{div}\boldsymbol{\sigma}$ is the backward spatial divergence of $\boldsymbol{\sigma}$, having its i^{th} component given by $\partial\sigma_{ij}/\partial x_j$ (where repeated indices are implicitly summed from 1 to 3).

From Fig. 2.26, the corresponding mapping from an initial position $\mathbf{X}$ to deformed position $\mathbf{x}$ is:

$$\begin{pmatrix} x_1 \\ x_2 \end{pmatrix} = \begin{pmatrix} \frac{-H}{\beta} + \left(\frac{H}{\beta} + X_1\right)\cos\left(\frac{\beta X_2}{H}\right) \\ \left(\frac{H}{\beta} + X_1\right)\sin\left(\frac{\beta X_2}{H}\right) \end{pmatrix} . \tag{2.51}$$

As can be confirmed by direct substitution, the following sequence of calculations decomposes the deformation gradient into rotation and stretch $\mathbf{F} = \mathbf{R} \cdot \mathbf{U}$, where $\mathbf{R}$ is the rotation tensor and $\mathbf{U}$ is the stretch tensor:

$$\alpha = \frac{\beta[t] X_2}{H}, \qquad \lambda = \frac{\beta[t] X_1}{H} + 1, \tag{2.52a}$$

$$\mathbf{R} = \begin{pmatrix} \cos\alpha & -\sin\alpha & 0 \\ \sin\alpha & \cos\alpha & 0 \\ 0 & 0 & 1 \end{pmatrix}, \qquad \mathbf{U} = \begin{pmatrix} 1 & 0 & 0 \\ 0 & \lambda & 0 \\ 0 & 0 & 1 \end{pmatrix} . \tag{2.52b}$$

Here, α is the angle of rotation at the material point of interest, λ is the amount of stretch in the 2-direction. For uniaxial strain in the 2-direction, the rotation is $\mathbf{R} = \mathbf{I}$, and therefore the deformation gradient is $\mathbf{F} = \mathbf{U}$, and the Jacobian is λ.

In the MMS, we assume that we have all the information in (2.50) except the body force. It is possible (*e.g.,* by running a single-element model driver) to obtain all stress components as a function of uniaxial strain stretching in the 2-direction *without rotation.* To apply this manufactured solution to an arbitrary, potentially anisotropic and even more nonlinear, elastic constitutive model, the upcoming analysis presumes only that the response functions for all components of stress under uniaxial strain in the 2-direction are known; *i.e.,*

$$[\bar{\boldsymbol{\sigma}}] = \begin{bmatrix} \sigma_{11}[\lambda] & \sigma_{12}[\lambda] & \sigma_{13}[\lambda] \\ \sigma_{21}[\lambda] & \sigma_{22}[\lambda] & \sigma_{23}[\lambda] \\ \sigma_{31}[\lambda] & \sigma_{32}[\lambda] & \sigma_{33}[\lambda] \end{bmatrix} . \tag{2.53}$$

Then the Cauchy stress $\boldsymbol{\sigma}$ is computed using

$$\boldsymbol{\sigma} = \mathbf{R} \cdot \bar{\boldsymbol{\sigma}} \cdot \mathbf{R}^{\mathbf{T}} , \tag{2.54}$$

where $\mathbf{R}$ is the rotation tensor. The indicial form for (2.54) is given by

$$\frac{\partial \sigma_{ij}}{\partial x_j} = \frac{\partial}{\partial x_j}(R_{im} \cdot \bar{\sigma}_{mn} \cdot R_{jn}) . \tag{2.55}$$

By the product rule,

$$\frac{\partial \sigma_{ij}}{\partial x_j} = \frac{\partial (R_{im})}{\partial x_j}\, \bar{\sigma}_{mn} R_{jn} + R_{im} \bar{\sigma}_{mn}\, \frac{\partial (R_{jn})}{\partial x_j} + R_{im}\, \frac{\partial \bar{\sigma}_{mn}}{\partial x_j}\, R_{jn} . \tag{2.56}$$

Recalling from (2.53) that $\bar{\boldsymbol{\sigma}}$ depends only on λ, and noting that (2.52) shows that the polar rotation $\mathbf{R}$ depends only on the rotation angle α, using the chain rule

$$\frac{\partial (R_{im})}{\partial x_j} = \frac{d(R_{im})}{d\alpha}\, \frac{\partial \alpha}{\partial x_j}, \qquad \frac{\partial \bar{\sigma}_{mn}}{\partial x_j} = \frac{d\bar{\sigma}_{mn}}{d\lambda}\, \frac{\partial \lambda}{\partial x_j} , \tag{2.57a}$$

$$\frac{d\mathbf{R}}{d\alpha} = \mathbf{A}\cdot\mathbf{R}, \quad \text{where} \quad \mathbf{A} = \begin{pmatrix} 0 & -1 & 0 \\ 1 & 0 & 0 \\ 0 & 0 & 0 \end{pmatrix} , \tag{2.57b}$$

$$\frac{\partial\alpha}{\partial x_j} = \frac{d\alpha}{dX_s}\,\frac{\partial X_s}{\partial x_j} = \frac{d\alpha}{dX_s}\,F^{-1}_{sj} = \frac{d\alpha}{dX_s}\,U^{-1}_{sa}\,R_{ja} . \tag{2.57c}$$

Using (2.57b), (2.57c) and substituting in (2.57a),

$$\frac{\partial R_{im}}{\partial x_j} = A_{ip}\,R_{pm}\,\frac{d\alpha}{dX_s}\,U^{-1}_{sa}\,R_{ja} . \tag{2.58}$$

This implies that

$$\frac{\partial R_{jn}}{\partial x_j} = A_{jp}\,R_{pn}\,\frac{d\alpha}{dX_s}\,U^{-1}_{sa}\,R_{ja} . \tag{2.59}$$

Using (2.58) and (2.59), (2.56) can be reduced to

$$\begin{aligned} f_i = \frac{\partial\sigma_{ij}}{\partial x_j} = A_{ip}\,R_{pm}\,\frac{d\alpha}{dX_s}\,U^{-1}_{sa}\,R_{ja}\,\bar{\sigma}_{mn}\,R_{jn} + R_{im}\,\frac{\partial\bar{\sigma}_{mn}}{\partial x_j}\,R_{jn} \\ + R_{im}\,\bar{\sigma}_{mn}\,A_{jp}\,R_{pn}\,\frac{d\alpha}{dX_s}\,U^{-1}_{sa}\,R_{ja} . \end{aligned} \tag{2.60}$$

Multiplying both sides of (2.60) using R_{iq} and simplifying using the fact that $\mathbf{R}$ is orthogonal

$$\bar{f}_q = R_{iq}\,\frac{\partial\sigma_{ij}}{\partial x_j} = A_{qm}\,\frac{d\alpha}{dX_s}\,U^{-1}_{sn}\,\bar{\sigma}_{mn} + \frac{\partial\bar{\sigma}_{qn}}{\partial x_j}\,R_{jn} + \bar{\sigma}_{qn}\,A_{qn}\,\frac{d\alpha}{dX_s}\,U^{-1}_{sa} . \tag{2.61}$$

Recalling from (2.53) that $\boldsymbol{\sigma}$ depends only on λ, and from (2.52) that λ depends only on $\boldsymbol{X}$

$$\frac{\partial\bar{\sigma}_{qn}}{\partial x_j} = \frac{\partial\bar{\sigma}_{qn}}{\partial\lambda}\,\frac{\partial\lambda}{\partial x_j} = \frac{\partial\bar{\sigma}_{qn}}{\partial\lambda}\,\frac{\partial\lambda}{\partial X_p}\,\frac{\partial X_p}{\partial x_j} = \frac{\partial\bar{\sigma}_{qn}}{\partial\lambda}\,\frac{\partial\lambda}{\partial X_p}\,U^{-1}_{pt}\,R_{jt} . \tag{2.62}$$

Using the definitions of λ, $\mathbf{U}$ and $\mathbf{A}$ and substituting (2.62) in (2.61), we have

$$\bar{f}_q = R_{iq}\,\frac{\partial\sigma_{ij}}{\partial x_j} = \frac{\beta}{H\lambda}(A_{q1}\,\bar{\sigma}_{12} + A_{q2}\,\bar{\sigma}_{22} + \lambda\,\frac{\partial\bar{\sigma}_{q1}}{\partial\lambda} + \bar{\sigma}_{q1}) . \tag{2.63}$$

Thus, the unrotated force components are

$$\bar{f}_1 = \frac{\beta}{H\lambda}(-\bar{\sigma}_{22} + \lambda\frac{\partial\bar{\sigma}_{11}}{\partial\lambda} + \bar{\sigma}_{11}) , \tag{2.64a}$$

$$\bar{f}_2 = \frac{\beta}{H\lambda}(\bar{\sigma}_{12} + \lambda\frac{\partial\bar{\sigma}_{21}}{\partial\lambda} + \bar{\sigma}_{21}) , \tag{2.64b}$$

$$\bar{f}_1 = \frac{\beta}{H\lambda}(\lambda\frac{\partial\bar{\sigma}_{31}}{\partial\lambda} + \bar{\sigma}_{31}) . \tag{2.64c}$$

These are the unrotated force components. To apply these in a calculation of the body force for the manufactured solution, the actual force vector can be computed by recalling that $\boldsymbol{f} = \mathbf{R}\cdot\bar{\boldsymbol{f}}$. In general, this comes out to be in the form

$$\boldsymbol{f} = f_r\boldsymbol{e}_r + f_\theta\boldsymbol{e}_\theta . \tag{2.65}$$

The force contribution from the material acceleration is relatively easy because we already have the relation between $\boldsymbol{x}$ and $\boldsymbol{X}$. Acceleration is simply

$$\boldsymbol{a} = \left(\frac{\partial^2 \boldsymbol{x}}{\partial t^2}\right)_{\boldsymbol{X}} = \frac{\partial^2 \boldsymbol{x}}{\partial \beta^2}\left(\frac{d\beta}{dt}\right)^2 + \frac{\partial \boldsymbol{x}}{\partial \beta}\frac{\partial^2 \beta}{\partial t^2} \ , \tag{2.66}$$

where the derivatives with respect to β are found by differentiating (2.52). The result gives the cartesian components of acceleration which must be converted to polar components to give a final acceleration of the form

$$\boldsymbol{a} = a_r \boldsymbol{e}_r + a_\theta \boldsymbol{e}_\theta \ . \tag{2.67}$$

Density is

$$\rho = \frac{\rho_0}{\lambda} \ . \tag{2.68}$$

Substituting (2.68), (2.67), and (2.65) in (2.50) after choosing the material model and material constants, the total body force required for this deformation is:

$$\boldsymbol{b} = b_r \boldsymbol{e}_r + b_\theta \boldsymbol{e}_\theta \ , \tag{2.69}$$

where

$$b_r = a_r - \frac{f_r}{\rho}, \quad b_\theta = a_\theta - \frac{f_\theta}{\rho} \ . \tag{2.70}$$

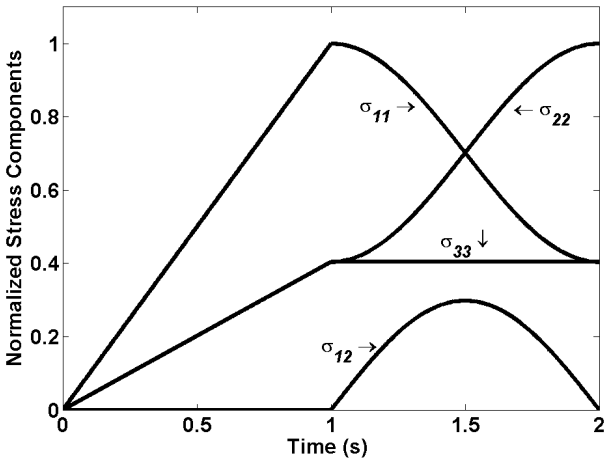

Figure 2.1: Analytical solution for a rate-independent linear-elastic medium

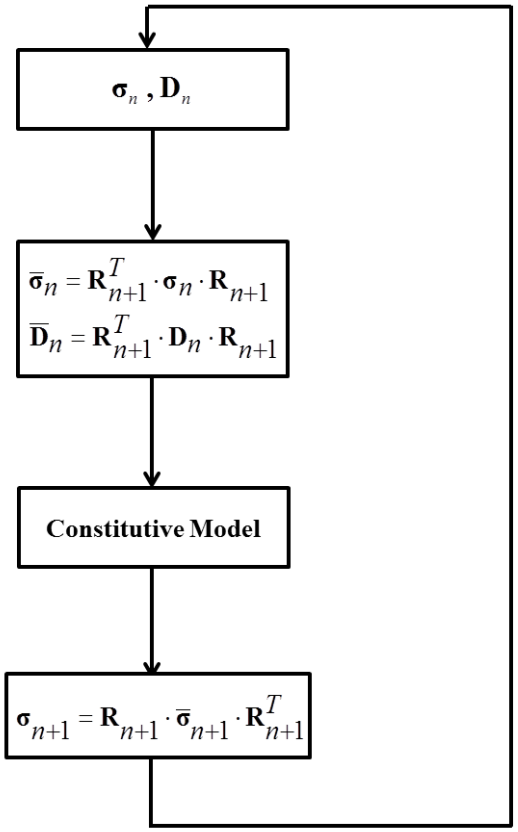

Figure 2.2: Flawed stress update algorithm

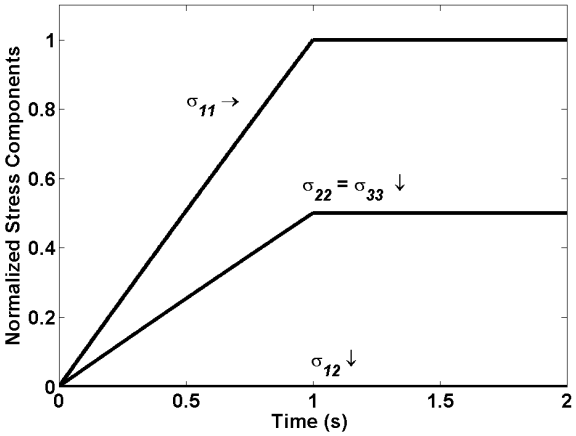

Figure 2.3: Incorrect solution resulting from flawed application of strong objectivity

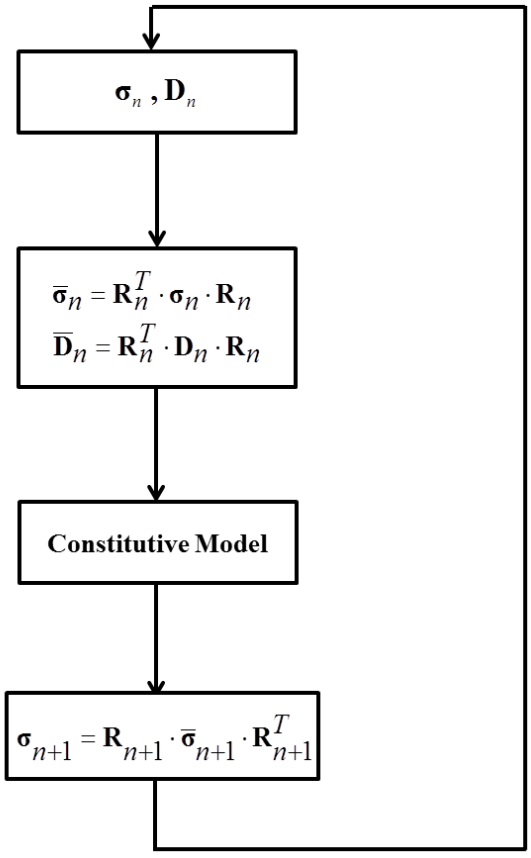

Figure 2.4: Corrected stress update algorithm

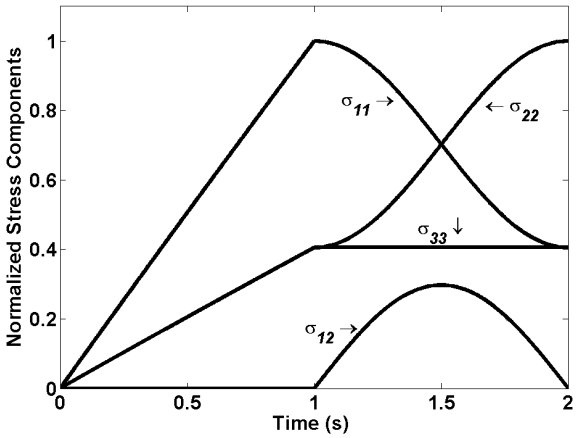

Figure 2.5: Correct solution resulting from the corrected stress update algorithm

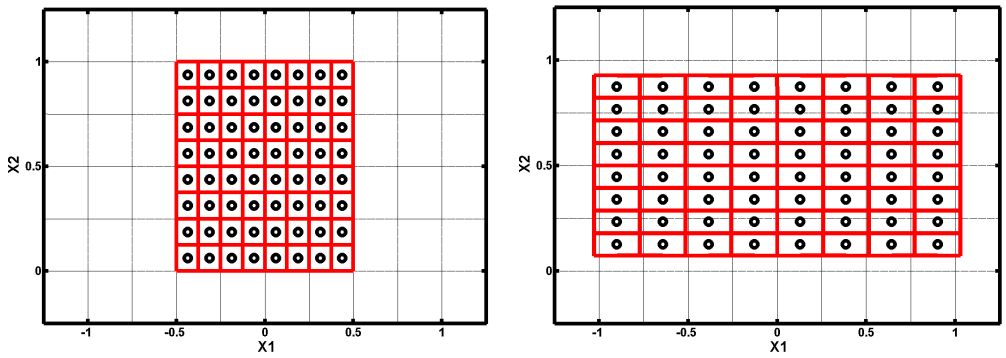

(a) Initial square domain **(b)** Flawed solution

Figure 2.6: Anomalous vertical contraction in a uniaxial strain MMS, exposing an applicability limit of an existing traction boundary condition option. (a) shows the initial configuration, and (b) shows the anamolous vertical contraction

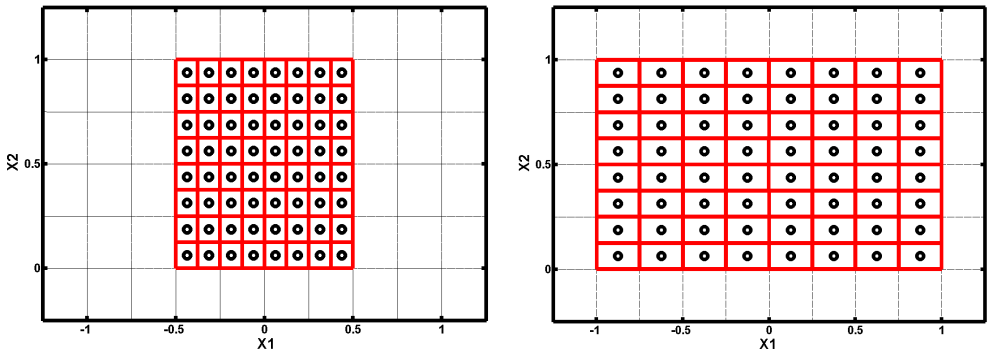

(a) Initial square domain **(b)** Corrected solution

Figure 2.7: Elimination of anomalous vertical contraction upon the extension of traction boundary conditions to account for geometric nonlinearity of varying area. (a) shows the initial configuration, and (b) shows the elimination of anamolous vertical contraction

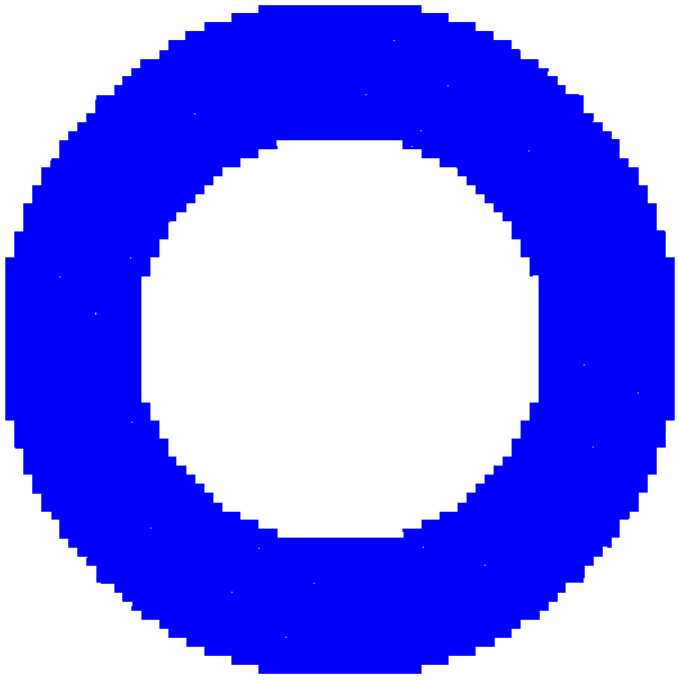

Figure 2.8: The problem domain of the generalized vortex example using a ragged (*i.e.*, stair-stepped/nonconforming) boundary

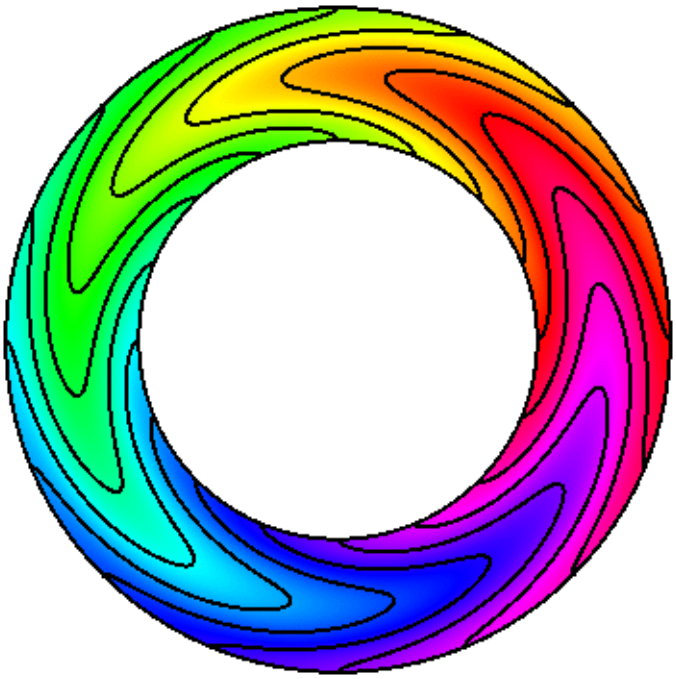

Figure 2.9: Problem domain of generalized vortex with the displacement field. The hue is proportional to initial angular coordinate

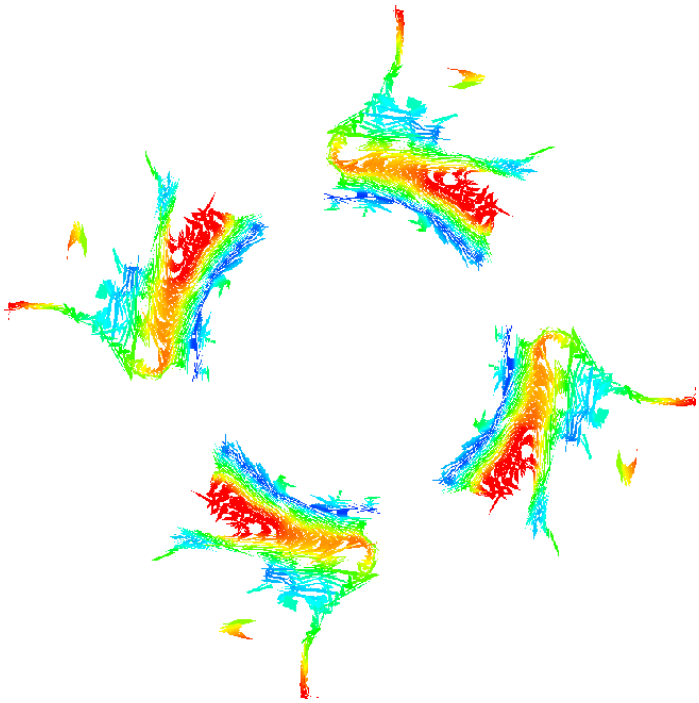

Figure 2.10: Color plot of displacement magnitude using uGIMP where the simulation becomes unstable. Red is maximum displacement (peak amplitude of 1 radian), blue is zero displacement

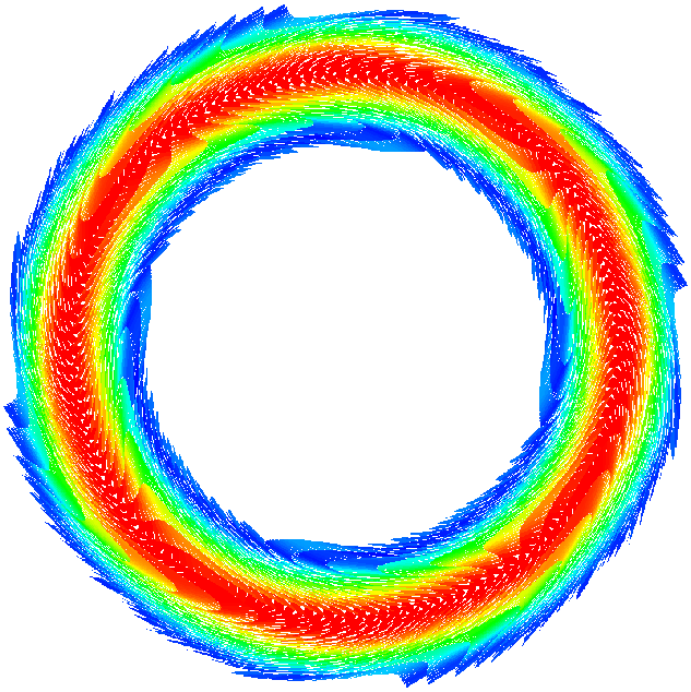

Figure 2.11: Color plot of displacement magnitude near the peak rotation angle using CPDI. Red is maximum displacement (peak amplitude of 1 radian), blue is zero displacement

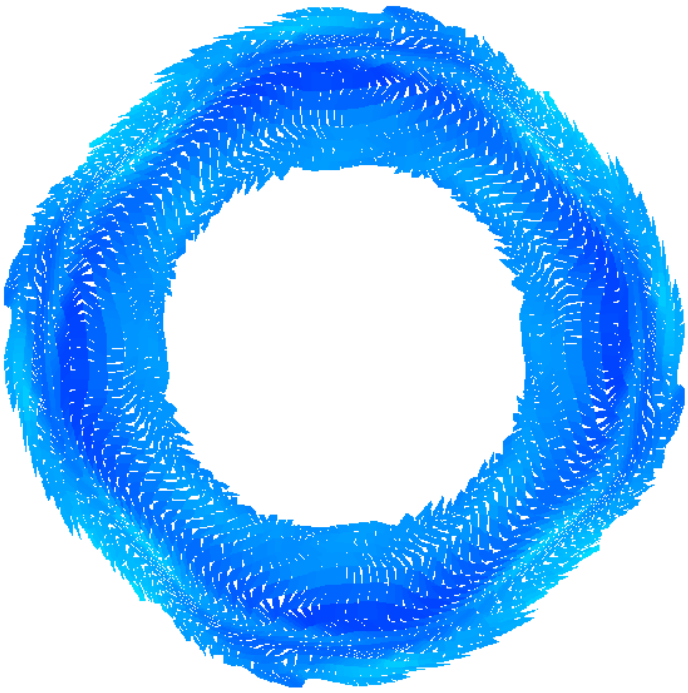

Figure 2.12: Final configuration using CPDI at $t = 1s$. Red is maximum displacement (peak amplitude of 1 radian), blue is zero displacement

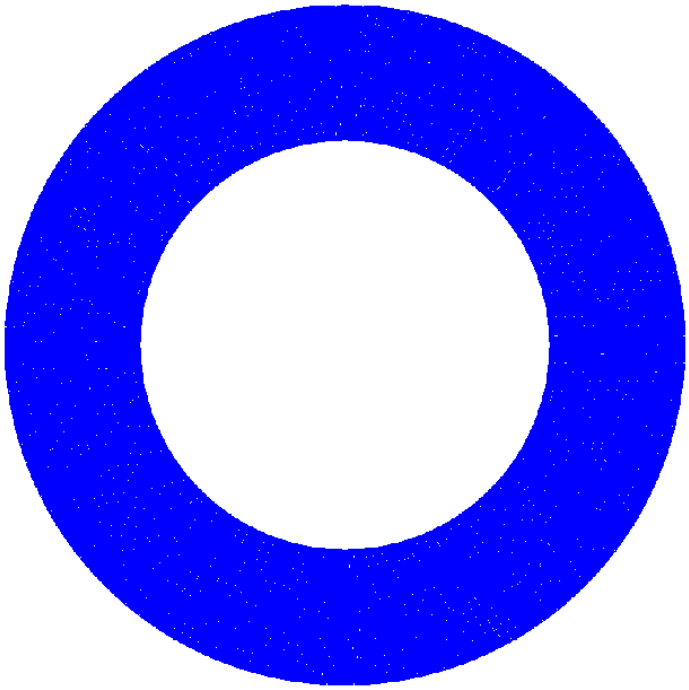

Figure 2.13: Domain with the particles conforming with the boundary

Figure 2.14: Final configuration using CPDI with conforming boundary. Red is maximum displacement (peak amplitude of 1 radian), blue is zero displacement

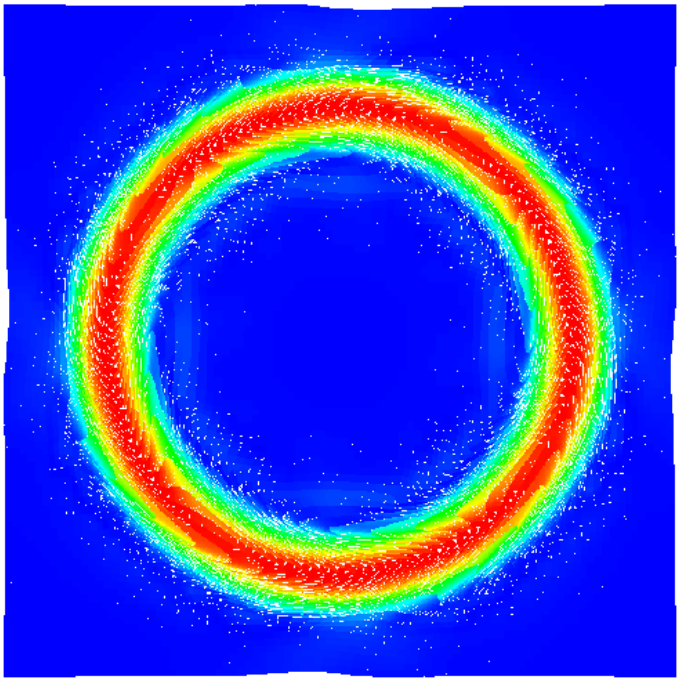

Figure 2.15: Color plot of displacement magnitude near the peak rotation angle using CPDI. Red is maximum displacement (peak amplitude of 1 radian), blue is zero displacement

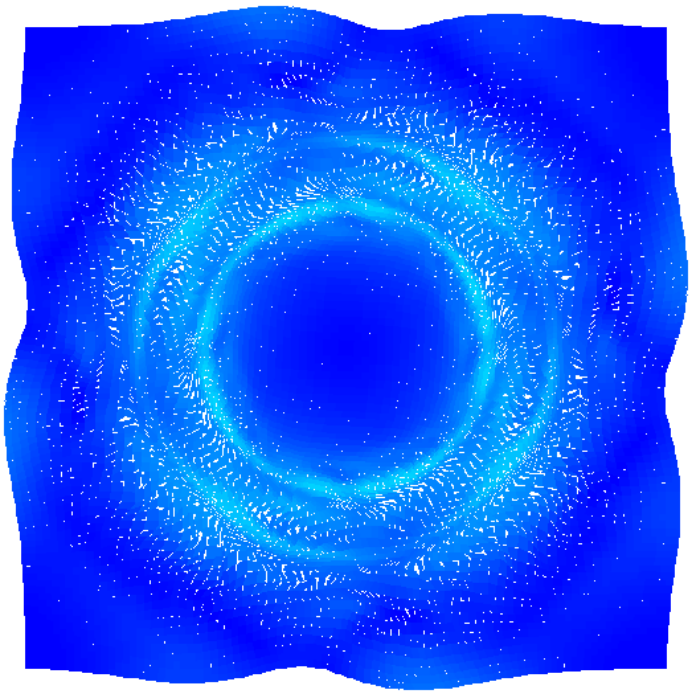

Figure 2.16: The final configuration using CPDI. Red is maximum displacement (peak amplitude of 1 radian), blue is zero displacement

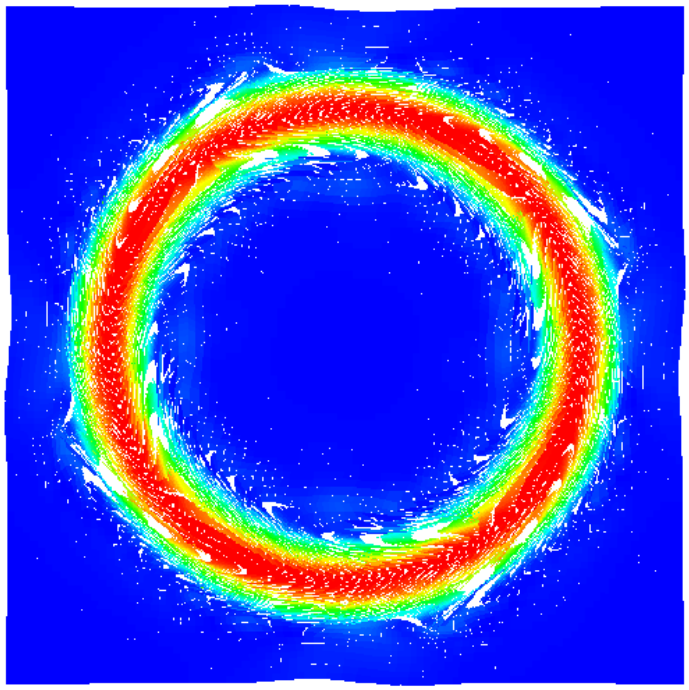

Figure 2.17: Color plot of displacement magnitude near the peak rotation angle using uGIMP. Red is maximum displacement (peak amplitude of 1 radian), blue is zero displacement

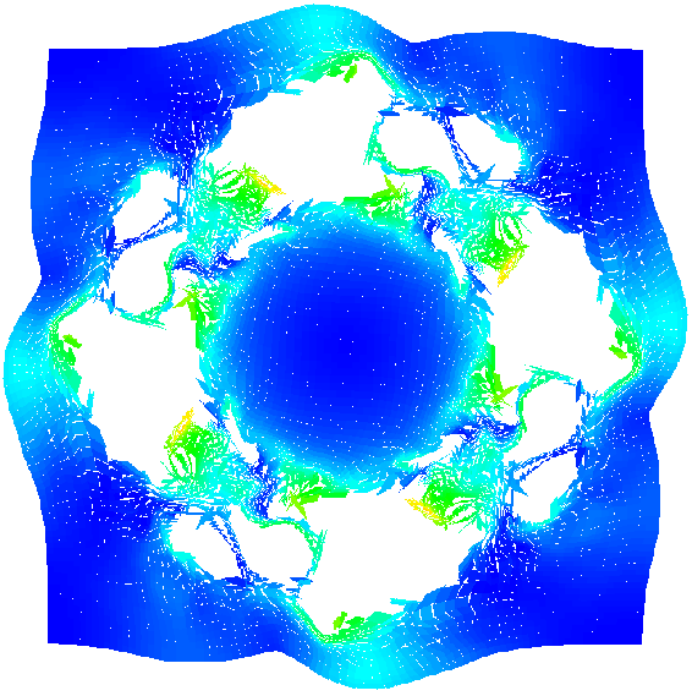

Figure 2.18: The final configuration using uGIMP. Red is maximum displacement (peak amplitude of 1 radian), blue is zero displacement

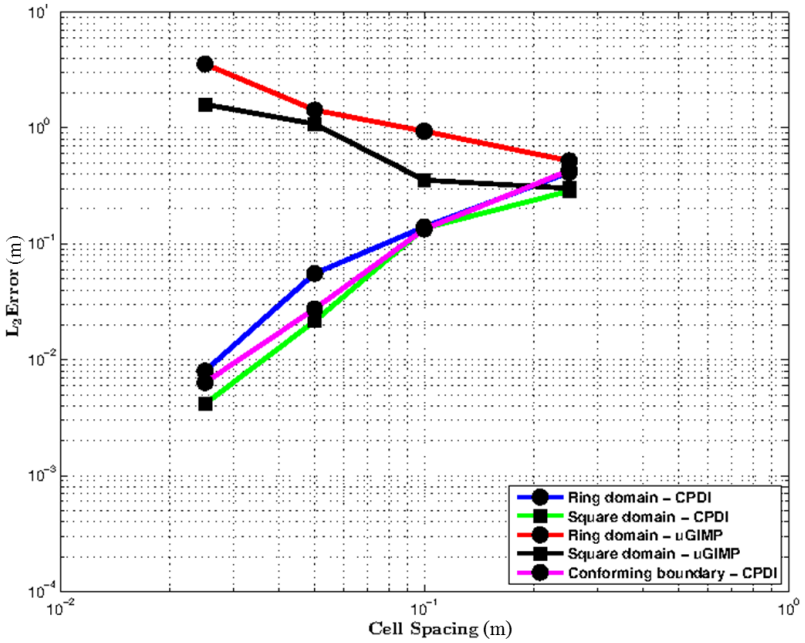

Figure 2.19: L_2 error vs. cell spacing comparison for peak amplitude of 1 radian at the end of the simulation

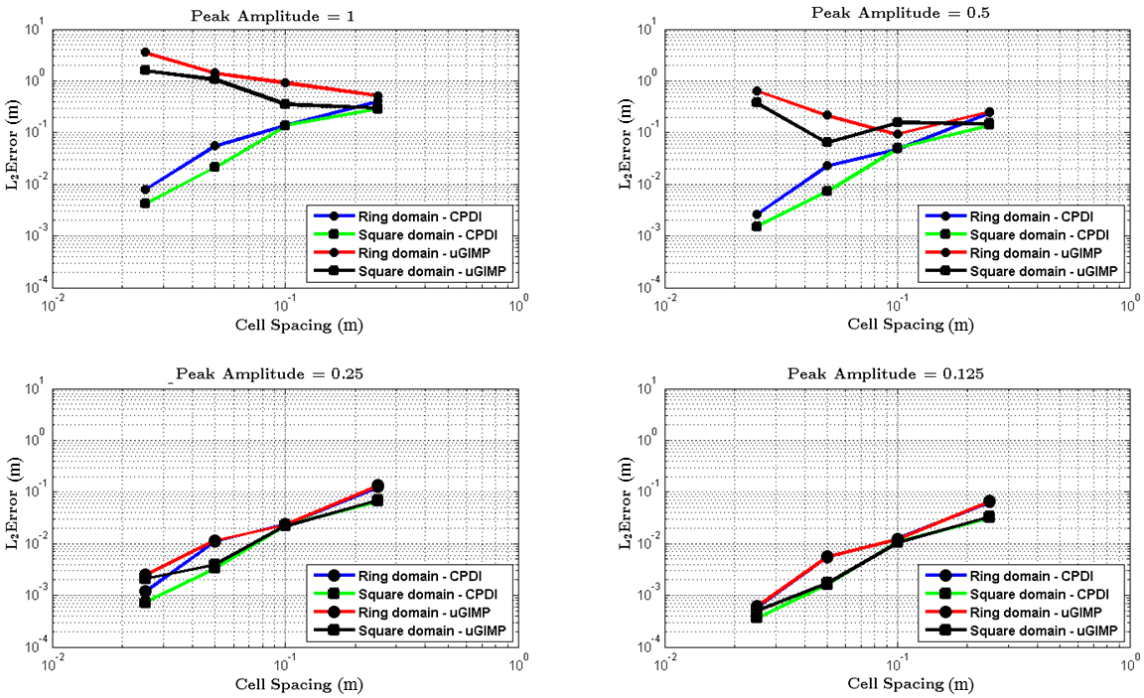

Figure 2.20: L_2 error vs. cell spacing comparison for various peak amplitudes at the end of the simulation

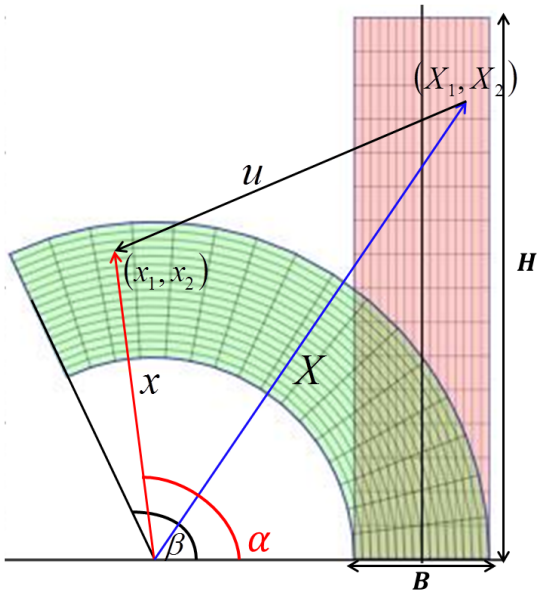

Figure 2.21: Snapshot of deformation in time for the bending bar problem

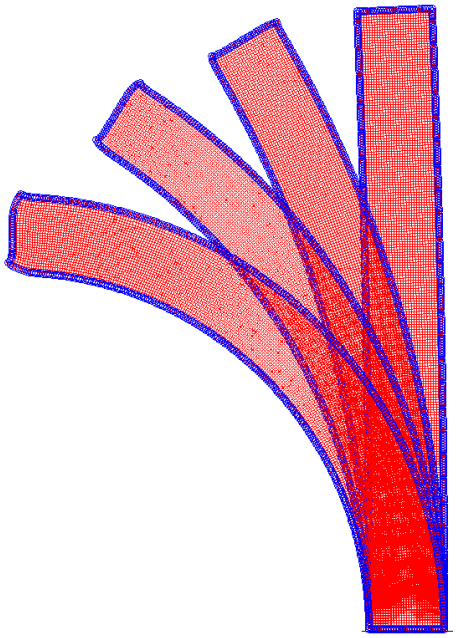

Figure 2.22: Snapshots of the deformation during loading phase

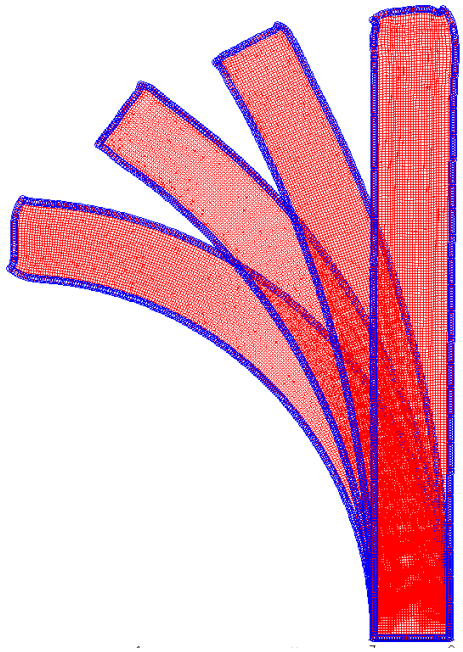

Figure 2.23: Snapshots of the deformation during unloading phase

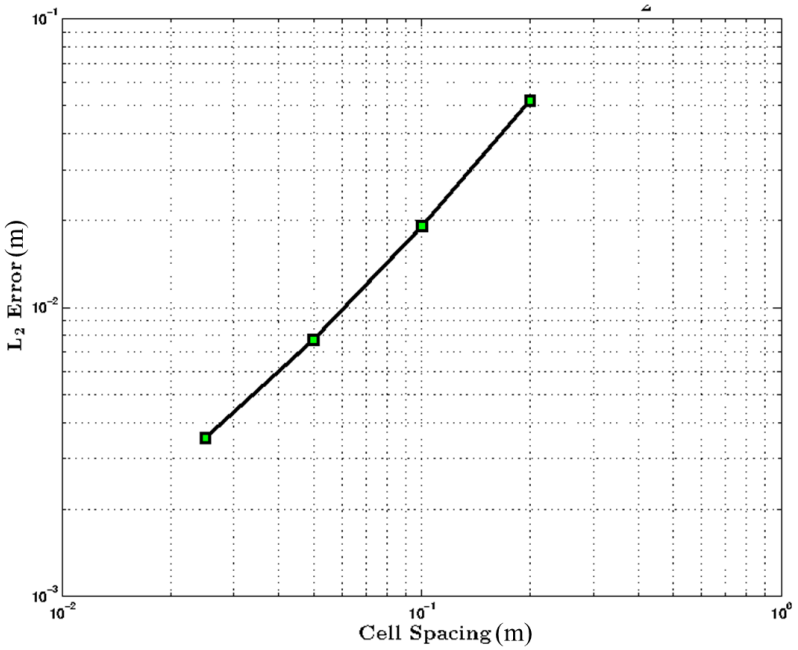

Figure 2.24: L_2 error vs. cell spacing for a peak amplitude of $\frac{\pi}{2}$ at the end of the simulation

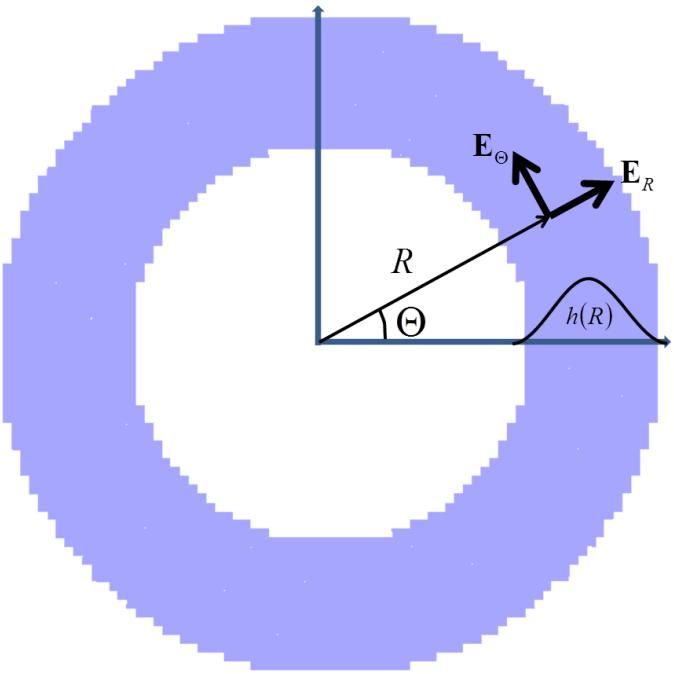

Figure 2.25: The problem domain of the generalized vortex example

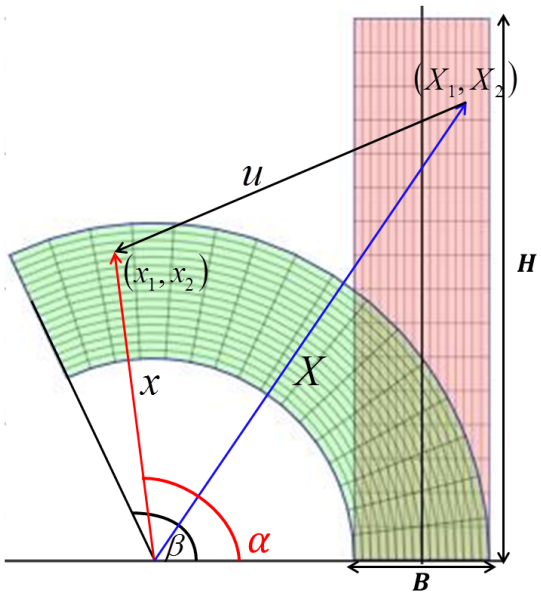

Figure 2.26: Snapshot of deformation in time for the bending bar problem

CHAPTER 3

CODE VERIFICATION TESTS FOR PLASTIC CONSTITUTIVE MODELS UNDER LARGE DEFORMATIONS

3.1 Abstract

Path-dependent constitutive models are intensely researched in solid mechanics due to their importance for many practical engineering applications. Responsible use of these models requires a rigorous verification and validation process. Previous work using method of manufactured solutions (MMS) to verify elastic constitutive models is extended to include two large-deformation problems using linear-elastic, perfectly-plastic constitutive models. These verification tests include homogeneous and nonhomogeneous deformations subjected to both loading and unloading. The nonhomogeneous MMS problem also includes varying levels of superimposed rotations. These problems can be used to quantify the accuracy and robustness of any plasticity model that includes von-Mises plasticity as a special case.

3.2 Introduction

Numerical simulations are now a common component in decision making for both industry and the scientific community, which therefore implies an ongoing need to assess solution quality. Verification and validation (V&V) definitions and procedures are well documented in the literature [79, 73, 67]. Code verification is the process of confirming that the numerical methods and the constitutive models are implemented correctly by comparing the numerical solutions against known solutions, whereas code validation is evidence of how close the numerical predictions are to reality (experimental data). In this work, we focus on code verification problems using the method of manufactured solutions (MMS) [84].

This chapter has been submitted to "Engineering with Computers" and is under review.

To date, verification has applied the MMS to test boundary-value solvers with moderately simplistic (*e.g.,* elastic) constitutive models (*c.f.,* [12, 3, 52]), but tests of path-dependent constitutive models are needed because of their prevalent use in various fields such as aerospace, automotive, defense, safety *etc.* Verification of these models naturally must precede validating them. MMS is the process of deriving the analytical body forces, tractions, and the initial conditions required to achieve a pre-determined deformation field. Different engineering fields including fluid mechanics [75, 93, 28], electromagnetics [72], heat transfer [18], nuclear engineering [68], *etc.* have already adopted this verification technique. In the area of solid mechanics, manufactured solutions available in the literature are limited to elastic constitutive models and might furthermore entail deformation modes that are too simplistic (*e.g.,* lacking material rotation and/or distortion) to reveal shortcomings of the constitutive model or the host-code solver of the momentum equation [94, 82].

The method of manufactured solutions (MMS), which is built up from a predetermined deformation field, typically requires a nonzero body force in addition to boundary tractions. The method of exact solutions (MES) [51], on the other hand, determines the stress and deformation fields from specified boundary tractions, usually without body forces. To find such solutions, simplifying assumptions (such as small strains, elasticity, and/or quasistatics [2, 19]) are often required, and transients (such as unloading or changes in loading direction and/or loading rate) are often avoided if the constitutive model is history dependent. In elasto-plastic simulations, the loading and unloading parts behave differently, depending on whether or not the yield criterion is met, and this complication is especially difficult if plasticity is part of the unloading response. Closed-form mathematical expressions for ideal plastic bending at finite strain were first presented by Ref [41], but neglecting elastic strains. Ref [99] presented a closed-form solution to finite bending of a compressible elastic-perfectly plastic rectangular block, but the analytical solution was limited to loading. Several other exact solutions [102, 31] for elasto-plasticity are available in the literature, but they are also limited to loading. These MES solutions therefore fall short of properly verifying the code for arbitrary deformations.

This chapter presents two method of manufactured solutions for large deformation plasticity:

1. Homogeneous deformation MMS for an elastic, perfectly-plastic constitutive model under large deformations for both loading and unloading.

2. Nonhomogeneous deformation bending bar MMS for an elastic, perfectly-plastic constitutive model under large deformations for both loading and unloading.

For a manufactured solution, the analytical forcing terms are derived from balance of momentum in continuum mechanics:

$$\operatorname{div}(\boldsymbol{\sigma}) + \rho \boldsymbol{b} = \rho \boldsymbol{a} \ , \tag{3.1}$$

where $\boldsymbol{\sigma}$ is Cauchy stress, ρ is the spatial mass density, $\boldsymbol{b}$ is the body force per unit mass, $\boldsymbol{a}$ is the acceleration, and $\operatorname{div}(\boldsymbol{\sigma})$ is the spatial divergence of Cauchy stress. An equivalent form of the momentum equation is

$$\operatorname{DIV}(\boldsymbol{P}) + \rho_0 \boldsymbol{b} = \rho_0 \boldsymbol{a} \ , \tag{3.2}$$

in which ρ_0 is the initial density, $\boldsymbol{P}$ is the first Piola-Kirchhoff stress defined in terms of the deformation gradient $\boldsymbol{F}$ and its Jacobian determinant J by $\boldsymbol{P} = J\boldsymbol{\sigma} \cdot \boldsymbol{F}^{-T}$, and $\operatorname{DIV}(\boldsymbol{P})$ is the reference divergence of stress for which the i^{th} component is $\partial P_{ij}/\partial X_j$ (where X_j is the j^{th} component of the initial position vector).

The MMS problems are illustrated here using a particle-based method called the material point method (MPM)[87], but they can also be used to verify any other momentum solver. Our focus on the MPM is motivated by its increasing appeal in mechanics [42, 104] (not to mention its usefulness in so-called physics-based animation [85]), requiring a greater urgency to properly verify MPM in comparison to far more reliably established approaches such as the finite-element method (FEM). For example, while patch tests (*e.g.*, homogeneous deformations) are more than adequately demonstrated in the FEM literature, such tests remain almost entirely absent in the MPM literature and are much needed because algorithms for traction boundary conditions in the MPM are still under active development (*c.f.,* [103]).

3.3 Uniaxial strain MMS for traction boundary conditions

This section describes a homogeneous uniaxial-strain MMS for a linear-elastic, perfectly-plastic material under loading and unloading. Aside from being a crucial test for users and developers of any elastic-plastic constitutive model (especially when run as an MMS problem rather than MES), uniaxial strain deformation is the main subcomponent of the inhomogeneous deformation problem of Sec. 3.4. To determine the analytical body forces from Eq. (3.1), the constitutive model is used to infer the stress field, from which the associated spatial divergence can be evaluated; for history-dependent materials, this step is nontrivial because the stress is not determined exclusively from the deformed state: *finding the stress field requires consideration of the entire history of deformation up to the current instant in time.* Acceleration is evaluated from the predetermined displacement

field. Because both the deformation and the material are assumed to be homogeneous, the stress is the same at all points in space, making the divergence of the stress zero. Thus, the body force from Eq. (3.1) is equal to the acceleration. To evaluate the boundary tractions, we consider a linear-elastic perfectly-plastic constitutive model. The linear-elastic part is governed by Hooke's law,

$$\boldsymbol{\sigma} = \lambda \, \mathrm{tr}\,(\boldsymbol{\varepsilon})\, \mathbf{I} + 2G\,(\boldsymbol{\varepsilon})\,, \tag{3.3}$$

where λ, and G are the Lamé material constants, ε is the logarithmic strain tensor, and $\mathbf{I}$ is the identity tensor. Equivalently, the spectral form of Hooke's law is

$$\boldsymbol{\sigma} = 3K \, \mathrm{iso}\,(\boldsymbol{\varepsilon}) + 2G \, \mathrm{dev}\,(\boldsymbol{\varepsilon})\,, \tag{3.4}$$

where K and G are the bulk and shear moduli, respectively, and the operators "iso" and "dev" take the isotropic and deviatoric parts, respectively. Classical von-Mises plasticity is governed by a yield criterion,

$$\sqrt{3J_2} = Y, \tag{3.5}$$

where $J_2 = \frac{1}{2}\left\|\mathrm{dev}\boldsymbol{\sigma}\right\|^2$, and Y is the yield stress in uniaxial stress. Analytical solutions under uniaxial strain (in which lateral strain is zero) and uniaxial stress (in which lateral stress is zero) (*c.f.* [14]) are shown in Fig. 3.1, where σ_A and σ_L are the axial and lateral components of stress respectively, and ε_A is the axial strain.

From Fig. 3.1, the stress tensor components under different loading and unloading zones are given below.

1. Under the initial elastic loading (EL), the stress tensor $\boldsymbol{\sigma}_{\mathrm{EL}}$ for uniaxial-strain deformation is

$$\boldsymbol{\sigma}_{\mathrm{EL}} = \begin{pmatrix} \sigma_A & 0 & 0 \\ 0 & \sigma_L & 0 \\ 0 & 0 & \sigma_L \end{pmatrix} \text{ where, } \sigma_A = C\varepsilon_A, \;\; \sigma_L = \lambda\varepsilon_A, \tag{3.6}$$
$$C = \left(K + \frac{4}{3}G\right), \text{ and } \lambda = \left(K - \frac{2}{3}G\right).$$

   This leg of the solution applies until the yield criterion is met (*i.e.,* until the stress difference is $|\sigma_A - \sigma_L| = Y$), at which time, the yield strain is

$$\varepsilon_Y = \frac{Y}{2G} \tag{3.7}$$

2. Once uniaxial-strain plastic loading (PL) commences, the stress tensor $\boldsymbol{\sigma}_{\mathrm{PL}}$ is

$$\boldsymbol{\sigma}_{\mathrm{PL}} = \begin{pmatrix} \sigma_A & 0 & 0 \\ 0 & \sigma_L & 0 \\ 0 & 0 & \sigma_L \end{pmatrix} \text{ where, } \sigma_A = \sigma_{\mathrm{AY}} + K\varepsilon_A, \;\; \sigma_L = \sigma_{\mathrm{LY}} + K\varepsilon_A, \\ \sigma_{\mathrm{AY}} = \frac{CY}{2G}, \quad \text{and } \; \sigma_{\mathrm{LY}} = \frac{\lambda Y}{2G}. \tag{3.8}$$

3. During elastic unloading, the initial slopes for the axial stress-strain and lateral stress-strain curves are the constrained modulus C, and the Lamé modulus λ, respectively, until the strain difference, $|\varepsilon_A - \varepsilon_L|$, accumulated during that leg equals twice the yield strain. During this period, the stress state of the material falls within the yield surface. The stress tensor during this elastic unloading phase (EUL) is

$$\boldsymbol{\sigma}_{\mathrm{EUL}} = \begin{pmatrix} \sigma_A & 0 & 0 \\ 0 & \sigma_L & 0 \\ 0 & 0 & \sigma_L \end{pmatrix} \text{ where, } \sigma_A = \sigma_{A\mathrm{Peak}} - C\left(\varepsilon_{\mathrm{peak}} - \varepsilon_A\right), \\ \sigma_L = \sigma_{L\mathrm{Peak}} - \lambda\left(\varepsilon_{\mathrm{peak}} - \varepsilon_A\right), \; \sigma_{A\mathrm{Peak}} = \sigma_{\mathrm{AY}} + K\left(\varepsilon_{\mathrm{peak}} - \varepsilon_Y\right), \\ \text{and } \; \sigma_{L\mathrm{Peak}} = \sigma_{\mathrm{LY}} + K\left(\varepsilon_{\mathrm{peak}} - \varepsilon_Y\right). \tag{3.9}$$

4. Once the strain difference during unloading equals twice the yield strain, the particles become plastic under compression and the slope of the axial stress-strain and the lateral stress-strain changes back to the bulk modulus K. The stress state of the material lies on the yield surface during this period, but changes by moving along the surface in the direction of the hydrostat, thus accumulating an increase in pressure during the plastic unloading (PUL) phase according to

$$\boldsymbol{\sigma}_{\mathrm{PUL}} = \begin{pmatrix} \sigma_A & 0 & 0 \\ 0 & \sigma_L & 0 \\ 0 & 0 & \sigma_L \end{pmatrix} \text{ where, } \sigma_A = \sigma_{\mathrm{PA}} - K\left(\varepsilon_P - \varepsilon_A\right), \\ \sigma_L = \sigma_{\mathrm{PL}} - K\left(\varepsilon_P - \varepsilon_A\right), \; \sigma_{\mathrm{PA}} = \sigma_{A\mathrm{Peak}} - \frac{CY}{G}, \;\; \sigma_{\mathrm{PL}} = \sigma_{L\mathrm{Peak}} - \frac{\lambda Y}{G}, \\ \text{and } \; \varepsilon_P = \varepsilon_{\mathrm{peak}} - \frac{Y}{G}. \tag{3.10}$$

Once the stress is evaluated for all of the loading and unloading zones, the tractions on the faces of the 2D rectangular domain are given by $\boldsymbol{t} = \boldsymbol{\sigma} \cdot \boldsymbol{n}$, where $\boldsymbol{n}$ is the unit normal to the face.

Figures 3.2–3.4 show the snapshot of the initial discretized configuration of a unit square domain (corresponding to time $t = 0$s), deformed configuration at the end of loading period (corresponding to time $t = 0.5$s), and deformed configuration at the end of the unloading period (corresponding to time $t = 1$s), respectively.

The colors cyan and red, respectively, indicate particles that are elastic and plastic (for which the stress state lies on the yield surface). The corresponding MMS algorithm is presented in algorithm 4, which includes choices for material constants and other problem data. As indicated in algorithm 4, the peak displacement (defined by β) for each particle at the end of the loading period is 0.4m, and the final displacement at the end of the simulation is zero. Appropriate displacement predictions can be seen in Figs. 3.2–3.4.

To verify the stress predictions, the time histories of stress components and stress invariants were extracted for all particles during the simulation (shown in Fig. 3.5). Before providing quantitative errors, we note that the equivalent stress $\sqrt{3J_2}$ vs. time t plot in Fig. 3.5(b) confirms that all particles yield at the right value ($Y=$ 86646 Pa, defined in algorithm 4). Once the particles yield, during the plastic loading phase (until the time $t = 0.5$s), the stress state is on the yield surface (corresponding to zero slope in $\sqrt{3J_2}$ vs. t during loading). During unloading (time $t > 0.5$s), the stress state ($\sqrt{3J_2}$) of all the particles undergo elastic unloading until the strain difference equals twice the yield strain (corresponding to the decrease in value of $\sqrt{3J_2}$ and then increase back to yield). Once the current strain equals twice the yield strain, the particles undergo plastic unloading (corresponding to zero slope in $\sqrt{3J_2}$ vs. t) where the stress state of the particles lie on the yield surface.

For the components of the stress vs. strain plot (Fig. 3.5(a)), slope discontinuities occur at the right values as the analytical solution (Fig. 3.1). I_1 is defined as $tr(\boldsymbol{\sigma})$. Similar correct trends can be seen for $\sqrt{J_2}$ vs. I_1, and I_1 vs. time t plots, though some error is evident. The next section details the error quantification for displacements and stresses, where it is shown that the small errors are rooted in spatial discretization scheme of the material point method (which is an interesting observation since this problem is a patch test having zero spatial discretization error in more established methods like the finite-element method).

3.3.1 Convergence study

This section provides the spatial convergence studies for displacement and stress for the homogeneous deformation MMS. The spatial L_2 error [94] for displacement is defined by

$$\mathrm{L}_2 \text{ error} = \sqrt{\frac{\sum_{N_p} \parallel \mathbf{u}_{\text{exact}}(\boldsymbol{x}_p, t) - \mathbf{u}_{\text{app}}(\boldsymbol{x}_p, t) \parallel^2}{N_p}} \,, \tag{3.11}$$

where $\mathbf{u}_{\text{exact}}(x_p, t)$ and $\mathbf{u}_{\text{app}}(x_p, t)$ are, respectively, the analytical and calculated displacement vectors at the p^{th} particle position $\boldsymbol{x_p}$, and N_p is total number of particles in the domain.

Algorithm 4 Uniaxial strain plasticity homogeneous deformation MMS

1: Generate a 2D rectangular plane strain (cuboid in 3D) computational domain (we used a 1 meter on each side, but dimensions should be inconsequential since this is a homogeneous problem). The remainder of this algorithm refers to the 2D case; extension to 3D should be self-evident with the understanding that the out-of-plane boundary condition should be the lateral tractions.
2: Define the material constants and other problem parameters. For the MMS demonstrated here, the bulk and shear moduli are respectively $K = 416666.7$ and $G = 454545.5$ Pa. The yield stress is $Y = 86646$ Pa (which has been selected to initiate yield at 10% engineering strain). The stop time is $T = 1$ second.
3: Compute the Lamé and constrained moduli: $\lambda{=}K - \frac{2G}{3}$ and $C{=}K + \frac{4G}{3}$. All remaining steps in this algorithm apply to each material point (*e.g.,* each Gauss point in the case of FEM) and each timestep for time t satisfying $0 < t < T$.
4: Define a displacement scale function $\beta(t) = A\left(\frac{1-\cos(2\pi t/T)}{2}\right)$ (a cyclic function is used here). Here, $A = 0.4$.
5: Define stretch $\Lambda = 1 + \beta(t)$.
6: Define the stretch at yield. Here, $\Lambda_Y = e^{Y/(2G)}$, which should evaluate to 1.1 for the data in step 1.
7: Evaluate the peak stretch. $\Lambda_{\text{peak}} = \Lambda(t = 0.5) = 1 + A = 1.4$
8: Evaluate axial and lateral stress at yield in uniaxial strain. $\sigma_{\text{AY}} = \frac{CY}{2G}$, and $\sigma_{\text{LY}} = \frac{\lambda Y}{2G}$
9: **if** $(t \le T/2)$ **then**
10: $\sigma_{\text{EA}} = C(\log\Lambda)$ ▷ Axial stress under elastic loading
11: $\sigma_{\text{EL}} = \lambda(\log\Lambda)$ ▷ Lateral stress under elastic loading
12: $\sigma_{\text{PA}} = \sigma_{\text{AY}} + K(\log\Lambda - \log\Lambda_Y)$ ▷ Axial stress under plastic loading
13: $\sigma_{\text{PL}} = \sigma_{\text{LY}} + K(\log\Lambda - \log\Lambda_Y)$ ▷ Lateral stress under plastic loading
14: **if** $(\Lambda \le \Lambda_Y)$ **then**
15: $\boldsymbol{\sigma} = \begin{pmatrix} \sigma_{EA} & 0 \\ 0 & \sigma_{\text{EL}} \end{pmatrix}$ ▷ Stress solution during initial elastic loading leg
16: **else**
17: $\boldsymbol{\sigma} = \begin{pmatrix} \sigma_{\text{PA}} & 0 \\ 0 & \sigma_{\text{PL}} \end{pmatrix}$ ▷ Stress during the initial plastic loading leg
18: **end if**
19: **else**
20: **if** $T/2 < t \le T$ **then**
21: $\sigma_{A\text{Peak}} = \sigma_{\text{AY}} + K\left(\log\Lambda_{\text{peak}} - \log\Lambda_Y\right)$ ▷ Peak axial stress under plastic loading
22: $\sigma_{L\text{Peak}} = \sigma_{\text{LY}} + K\left(\log\Lambda_{\text{peak}} - \log\Lambda_Y\right)$ ▷ Peak lateral stress under plastic loading
23: **if** $\left(\log\Lambda_{\text{peak}} - \log\Lambda \ge \frac{Y}{G}\right)$ **then**
24: $\varepsilon_{\text{UL}} = \log\Lambda_{\text{peak}} - \frac{Y}{G}$ ▷ Value of strain where plastic unloading starts
25: $\sigma_{\text{AULP}} = \sigma_{A\text{Peak}} - C\left(\frac{Y}{G}\right)$ ▷ Value of axial stress where plastic unloading starts
26: $\sigma_{\text{LULP}} = \sigma_{L\text{Peak}} - \lambda\left(\frac{Y}{G}\right)$ ▷ Value of lateral stress where plastic unloading starts
27: $\sigma_{\text{AUL}} = \sigma_{\text{AULP}} - K(\varepsilon_{\text{UL}} - \log\Lambda)$ ▷ Axial stress under plastic unloading
28: $\sigma_{\text{LUL}} = \sigma_{\text{LULP}} - \lambda(\varepsilon_{\text{UL}} - \log\Lambda)$ ▷ Lateral stress under plastic unloading
29: **else**
30: $\sigma_{\text{AUL}} = \sigma_{A\text{Peak}} - C\left(\log\Lambda_{\text{peak}} - \log\Lambda\right)$ ▷ Axial stress under elastic unloading
31: $\sigma_{\text{LUL}} = \sigma_{L\text{Peak}} - \lambda\left(\log\Lambda_{\text{peak}} - \log\Lambda\right)$ ▷ Lateral stress under elastic unloading
32: **end if**
33: $\boldsymbol{\sigma} = \begin{pmatrix} \sigma_{\text{AUL}} & 0 \\ 0 & \sigma_{\text{LUL}} \end{pmatrix}$ ▷ Stress state during the elastic and plastic unloading legs
34: **else**
35: STOP.
36: **end if**
37: **end if**
38: Since all the stresses are available, tractions can be evaluated using $\mathbf{t} = \boldsymbol{\sigma} \cdot \mathbf{n}$, where $\mathbf{n}$ is the outward normal on the four faces of the rectangular domain. If the simulation is run in 3D, the same lateral stress component is used to evaluate the tractions on the other two faces of the domain.
39: Since the displacement scale function β is available, acceleration is the second derivative of the displacement scale function with respect to time multiplied by the domain length.
40: For each time step, compute the body forces using $\begin{pmatrix} b_x \\ b_y \end{pmatrix} = \begin{pmatrix} 2A\pi^2\cos(2\pi t)\, X_1 \\ 0 \end{pmatrix}$, where X is the axial position coordinate of the particle in the reference configuration. If the simulation is run in 3D, use $b_z = 0$.

The simulation was run for four different meshes, and the error in displacement was calculated at the end of the loading and unloading phases (corresponding to times $t = 0.5$s and $t = 1.0$s, respectively). Figure 3.6 shows the convergence plot for displacement with the rate of convergence 2.4 at the end of loading period and 1.2 at the end of unloading period. Similarly, the spatial L_2 error for stress is defined as

$$\text{L}_2 \text{ error} = \sqrt{\frac{1}{N_p}\sum_{N_p}\left\|\frac{\sigma_{\text{exact}}(x,t)}{Y} - \frac{\sigma_{\text{app}}(x,t)}{Y}\right\|^2} \tag{3.12}$$

where $\sigma_{\text{exact}}(x,t)$ and $\sigma_{\text{app}}(x,t)$ are, respectively, the analytical and numerical stress tensors at location x, and N_p is total number of particles in the domain. The divisor of Y is introduced to avoid overflow from large stress values and to give a nondimensional error.

For the error in stress (using a fixed CFL) the rate of convergence is 1.2 at the end of loading period and 0.94 at the end of unloading period. The convergence study was also repeated using a fixed time step (the smallest one in the fixed-CFL study) with no significant change in the convergence plot, thus indicating that the convergence behavior is primarily due to spatial resolution, not the time-stepping algorithm.

This verification test can be used to verify the implementation of a von-Mises plasticity model or any model that includes von-Mises plasticity as a special case [43, 15]. By exploiting the knowledge of strain at the end of loading, this problem may also be used to test a constant strain-to-failure option in damage models (*c.f.* [44, 96]).

3.4 Bending bar plasticity MMS

The problem domain for this test is a rectangular bar with height H and base B as shown in Fig. 3.8. The deformation state at all times and all locations is uniaxial strain with superimposed rotation, making this problem a natural extension of Sec. 3.3 to simultaneously test for correct, frame-indifferent, results under nonhomogeneous deformation. Chapter 2 presented this manufactured solution for a nonlinear-elastic constitutive model, and this section details the extension of the problem to the same von-Mises plasticity model discussed in Sec. 3.3. This bending bar solution is complicated by the need to break the domain into three sections: yield in compression, yield in tension, each surrounding an elastic core at the centerline. As the boundaries between these domains move, there will always be a collection of MPM particles (or, if applicable, FEM elements) that are theoretically in a mixed discontinuous elastic-plastic state, but which are treated as either elastic or plastic in the discretized solution (thus representing a source of error). The required body forces and tractions are derived in the Sec. 3.6.1 and summarized in algorithms 5–6.

Algorithm 5 Analytical body forces to run bending bar plasticity MMS

1: Define the material constants, problem domain dimensions, and other problem data. For the MMS demonstrated here, these are: initial density $\rho_0 = 1000\frac{kg}{m^3}$, bulk modulus $K = 416666.7Pa$, shear modulus $G = 454545.5Pa$, yield stress $Y = 1.5377 \times 10^4$ Pa, base of the bar $B = 1$m, height of the bar $H = 8m$, stop time $T = 1$s, and the amplitude of rotation $A = \frac{\pi}{4}$. In the remainder of this algorithm, each time t should be understood to actually time normalized by the stop time, t/T.

2: Compute derived constants. Stretch at yield under tension and compression are given respectively by $\Lambda_{\mathrm{YT}} = e^{Y/(2G)}$ and $\Lambda_{\mathrm{YC}} = e^{-Y/(2G)}$. For the given problem data, these evaluate to $\Lambda_{\mathrm{YT}} = 1.0171$ and $\Lambda_{\mathrm{YC}} = 0.9832$.

3: Compute and save the peak stretch at the end of loading period: $\Lambda_{\mathrm{peak}} = 1 + \frac{AX_1}{H}$.

4: Define the displacement scale function, $\beta(t) = A\left(\frac{1-\cos(2\pi t)}{2}\right)$.

5: Define stretch function $\Lambda(t, X_1) = 1 + \frac{\beta(t)X_1}{H}$.

6: Define rotation angle function $\alpha(t, X_2) = \frac{\beta(t)X_2}{H}$.

7: **if** $(X_1 < 0)$ **then**

8: $Y = -Y$ ▷ This is required for applying appropriate body forces for particles under compression

9: **else**

10: $Y = Y$ ▷ This is required for applying appropriate body forces for particles under tension

11: **end if**

12: **if** $(t <= 0.5)$ **then** ▷ Loading phase

13: **if** $(\Lambda < \Lambda_{\mathrm{YT}})$ & $(\Lambda > \Lambda_{\mathrm{YC}})$ **then** ▷ Particles are elastic

14: $p_1 = 128H^3 - 8A^2HX_2{}^2 - 5A^3X_1X_2{}^2 + 4\left(16H^3 + A^2HX_2{}^2 + A^3X_1X_2{}^2\right)\cos[2\pi t]$ ▷ Temporary variable

15: $p_2 = 4A^2(2H + AX_1)X_2{}^2\cos[4\pi t] - 4A^2HX_2{}^2\cos[6\pi t] - 4A^3X_1X_2{}^2\cos[6\pi t]$ ▷ Temporary variable

16: $p_3 = A^3X_1X_2{}^2\cos[8\pi t] - 128H^3\cos\left[\frac{AX_2\sin[\pi t]^2}{H}\right] - 32H^3\cos\left[2\pi t - \frac{AX_2\sin[\pi t]^2}{H}\right]$ ▷ Temporary variable

17: $p_4 = -32H^3\cos\left[2\pi t + \frac{AX_2\sin[\pi t]^2}{H}\right]$ ▷ Temporary variable

18: $p_5 = 3\pi^2\rho_0\csc[\pi t]^4$ ▷ Temporary variable

19: $p_6 = 32A^2H\left(-3K + 2G + 6G\log\left[1 + \frac{AX_1\sin[\pi t]^2}{H}\right]\right)\sin[\pi t]^2$ ▷ Temporary variable

20: $p_7 = -12AHX_2 - 4A^2X_1X_2 + A(8H + 7AX_1)X_2\cos[2\pi t]$ ▷ Temporary variable

21: $p_8 = +4A(H - AX_1)X_2\cos[4\pi t] + A^2X_1X_2\cos[6\pi t] + 32H^2\sin\left[\frac{AX_2\sin[\pi t]^2}{H}\right]$ ▷ Temporary variable

22: $p_9 = -8H^2\sin\left[2\pi t - \frac{AX_2\sin[\pi t]^2}{H}\right] + 8H^2\sin\left[2\pi t + \frac{AX_2\sin[\pi t]^2}{H}\right]$ ▷ Temporary variable

23: $b_r = \frac{1}{96AH^2\rho_0}\left(\left(p_1 + p_2 + p_3 + p_4\right)p_5 + p_6\right)$ ▷ Radial component of body force

24: $b_t = \frac{\pi^2\csc[\pi t]^4}{8AH}\left(p_7 + p_8 + p_9\right)$ ▷ Tangential component of body force

25: **else** ▷ Particles are plastic under loading

26: $p_{10} = 128H^3 - 8A^2HX_2^2 - 5A^3X_1X_2^2 + 4\left(16H^3 + A^2HX_2^2 + A^3X_1X_2^2\right)\cos[2\pi t]$ ▷ Temporary variable

27: $p_{11} = 4A^2(2H + AX_1)X_2^2\cos[4\pi t] - 4A^2HX_2^2\cos[6\pi t] - 4A^3X_1X_2^2\cos[6\pi t]$ ▷ Temporary variable

28: $p_{12} = A^3X_1X_2^2\cos[8\pi t] - 128H^3\cos\left[\frac{AX_2\sin[\pi t]^2}{H}\right]$ ▷ Temporary variable

29: $p_{13} = -32H^3\cos\left[2\pi t - \frac{AX_2\sin[\pi t]^2}{H}\right] - 32H^3\cos\left[2\pi t + \frac{AX_2\sin[\pi t]^2}{H}\right]$ ▷ Temporary variable

30: $p_{14} = \frac{1}{32AH^2}\pi^2\csc[\pi t]^4$ ▷ Temporary variable

31: $p_{15} = -\frac{A(K-Y)\sin[\pi t]^2}{H\rho_0}$ ▷ Temporary variable

32: $b_r = \left(p_{10} + p_{11} + p_{12} + p_{13}\right)p_{14} + p_{15}$ ▷ Radial component of body force

33: $b_t = \frac{\pi^2\csc[\pi t]^4}{8AH}\left(p_7 + p_8 + p_9\right)$ ▷ Tangential component of body force. It is same for all the phases

34: **end if** ▷ End for if-else block in line 13

35: **end if** ▷ End of the loading if-block in line 12

Algorithm 5 Continued..

if $(t > 0.5)$ **then** ▷ Unloading phase
  if $\left(\Lambda_{\text{peak}} < \Lambda_{\text{YT}}\right)$ & $\left(\Lambda_{\text{peak}} > \Lambda_{\text{YC}}\right)$ **then** ▷ Particles are elastic under unloading
    $b_r = \frac{1}{96AH^2\rho_0}\left(\left(p_1 + p_2 + p_3 + p_4\right)p_5 + p_6\right)$ ▷ Radial component of body force
    $b_t = \frac{\pi^2 \csc[\pi t]^4}{8AH}\left(p_7 + p_8 + p_9\right)$ ▷ Tangential component of body force
  else ▷ Particles are plastic under unloading
    if $(X_1 < 0)$ **then**
      if $\left(\log\left(\Lambda_{\text{peak}}\right) - \log\left(\Lambda\right) <= \frac{Y}{G}\right)$ **then**
      ▷ Particles that were under compression during loading become plastic under tension during unloading
        $p_{16} = -\frac{A(K+Y)\sin[\pi t]^2}{H\rho_0}$ ▷ Temporary variable
        $b_r = \left(p_{10} + p_{11} + p_{12} + p_{13}\right)p_{14} + p_{16}$ ▷ Radial component of body force
        $b_t = \frac{\pi^2 \csc[\pi t]^4}{8AH}\left(p_7 + p_8 + p_9\right)$ ▷ Tangential component of body force
      else ▷ Elastic unloading
        $p_{17} = -128H^3 + 8A^2HX_2^2 + 5A^3X_1X_2^2 - 4A^2(2H + AX_1)X_2^2\cos[4\pi t]$ ▷ Temporary variable
        $p_{18} = 4A^2(H + AX_1)X_2^2\cos[6\pi t] - A^3X_1X_2^2\cos[8\pi t] + 128H^3\cos\left[\frac{AX_2\sin[\pi t]^2}{H}\right]$ ▷ Temporary variable
        $p_{19} = 32H^3\cos\left[2\pi t - \frac{AX_2\sin[\pi t]^2}{H}\right] + 32H^3\cos\left[2\pi t + \frac{AX_2\sin[\pi t]^2}{H}\right]$ ▷ Temporary variable
        $p_{20} = -3\Lambda_{\text{peak}}\pi^2\rho_0\csc[\pi t]^4$ ▷ Temporary variable
        $p_{21} = 3KH\Lambda_{\text{peak}} - 3H\Lambda_{\text{peak}}Y + 4HG - 2H\Lambda_{\text{peak}}G + 2AGX_1$ ▷ Temporary variable
        $p_{22} = 6H\Lambda_{\text{peak}}G\log[\Lambda_{\text{peak}}] - 6H\Lambda_{\text{peak}}G\log\left[1 + \frac{AX_1\sin[\pi t]^2}{H}\right]$ ▷ Temporary variable
        $p_{23} = 3\Lambda_{\text{peak}}\pi^2\left(16H^3 + A^2HX_2^2 + A^3X_1X_2^2\right)\rho_0\csc[\pi t]^4$ ▷ Temporary variable
        $p_{24} = 3KH\Lambda_{\text{peak}} - 3H\Lambda_{\text{peak}}Y - 2H\Lambda_{\text{peak}}G + 2AGX_1$ ▷ Temporary variable
        $p_{25} = 6H\Lambda_{\text{peak}}G\log[\Lambda_{\text{peak}}] - 6H\Lambda_{\text{peak}}G\log\left[1 + \frac{AX_1\sin[\pi t]^2}{H}\right]$ ▷ Temporary variable
        $b_r = \frac{1}{96AH^2\Lambda_{\text{peak}}\rho_0}\left(\left(p_{17} + p_{18} + p_{19}\right)p_{20} - 16A^2\left(p_{21} + p_{22}\right) + 4\cos[2\pi t]\left(p_{23} + 4A^2\left(p_{24} + p_{25}\right)\right)\right)$ ▷ Radial component of body force
        $b_t = \frac{\pi^2 \csc[\pi t]^4}{8AH}\left(p_7 + p_8 + p_9\right)$ ▷ Tangential component of body force
      end if ▷ End for if block in line 42
    else
      if $\left(\log\left(\Lambda_{\text{peak}}\right) - \log\left(\Lambda\right) >= \frac{Y}{G}\right)$ **then**
      ▷ Particles that were under tension during loading become plastic under compression during unloading
        $b_r = \left(p_{10} + p_{11} + p_{12} + p_{13}\right)p_{14} + p_{16}$ ▷ Radial component of body force
        $b_t = \frac{\pi^2 \csc[\pi t]^4}{8AH}\left(p_7 + p_8 + p_9\right)$ ▷ Tangential component of body force
      else ▷ Elastic unloading
        $b_r = \frac{1}{96AH^2\Lambda_{\text{peak}}\rho_0}\left(\left(p_{17} + p_{18} + p_{19}\right)p_{20} - 16A^2\left(p_{21} + p_{22}\right) + 4\cos[2\pi t]\left(p_{23} + 4A^2\left(p_{24} + p_{25}\right)\right)\right)$ ▷ Radial component of body force
        $b_t = \frac{\pi^2 \csc[\pi t]^4}{8AH}\left(p_7 + p_8 + p_9\right)$ ▷ Tangential component of body force
      end if ▷ End for if block in line 60
    end if ▷ End for if block in line 41
  end if ▷ End for if block in line 37
end if ▷ End of unloading period and end for if block in line 36
$b_x = \cos\left(\alpha\right)b_r - \sin\left(\alpha\right)b_t$ ▷ x-component of body force
$b_y = \sin\left(\alpha\right)b_r + \cos\left(\alpha\right)b_t$ ▷ y-component of body force
if $(t \geq 1)$ **then**
  STOP.
end if

Algorithm 6 Evaluating tractions to run bending bar plasticity MMS

1: Repeat steps 1 through 11 from Algorithm 5.
2: Axial stress and lateral stress at yield are given respectively by $\sigma_{\mathrm{AY}} = \frac{CY}{2G}$, and $\sigma_{\mathrm{LY}} = \frac{\lambda Y}{2G}$.
3: **if** $(X_1 < 0)$ **then**
4: $\quad \sigma_{\mathrm{PA}} = \sigma_{\mathrm{AY}} + K\left(\log\Lambda - \log\Lambda_{\mathrm{YC}}\right)$ ▷ Axial stress beyond yield for particles under compression
5: $\quad \sigma_{\mathrm{PL}} = \sigma_{\mathrm{LY}} + K\left(\log\Lambda - \log\Lambda_{\mathrm{YC}}\right)$ ▷ Lateral stress beyond yield for particles under compression
6: **else**
7: $\quad \sigma_{\mathrm{PA}} = \sigma_{\mathrm{AY}} + K\left(\log\Lambda - \log\Lambda_{\mathrm{YT}}\right)$ ▷ Axial stress beyond yield for particles under tension
8: $\quad \sigma_{\mathrm{PL}} = \sigma_{\mathrm{LY}} + K\left(\log\Lambda - \log\Lambda_{\mathrm{YT}}\right)$ ▷ Lateral stress beyond yield for particles under tension
9: **end if** ▷ End for if block in line 3
10: **if** $(t <= 0.5)$ **then**
11: $\quad$ **if** $(\Lambda < \Lambda_{\mathrm{YT}})$ & $(\Lambda > \Lambda_{\mathrm{YC}})$ **then** ▷ Particles are elastic under loading
12: $\quad\quad \sigma_{\mathrm{EA}} = C\left(\log\Lambda\right)$ ▷ Axial stress under elastic loading
13: $\quad\quad \sigma_{\mathrm{EL}} = L\left(\log\Lambda\right)$ ▷ Lateral stress under elastic loading
14: $\quad\quad \boldsymbol{\sigma} = [\ \sigma_{\mathrm{EL}} \quad 0\ ; \quad 0 \quad \sigma_{\mathrm{EA}}\ ]$
15: $\quad$ **else** ▷ Particles are plastic under loading
16: $\quad\quad \boldsymbol{\sigma} = [\ \sigma_{\mathrm{PL}} \quad 0\ ; \quad 0 \quad \sigma_{\mathrm{PA}}\ ]$
17: $\quad$ **end if** ▷ End for if block in line 11
18: **else**
19: $\quad$ **if** $\left(\Lambda_{\mathrm{peak}} < \Lambda_{\mathrm{YT}}\right)$ & $\left(\Lambda_{\mathrm{peak}} > \Lambda_{\mathrm{YC}}\right)$ **then** ▷ Particles are elastic under unloading
20: $\quad\quad \boldsymbol{\sigma} = [\ \sigma_{\mathrm{EL}} \quad 0\ ; \quad 0 \quad \sigma_{\mathrm{EA}}\ ]$
21: $\quad$ **else** ▷ Particles are plastic under unloading
22: $\quad\quad$ **if** $(X_1 < 0)$ **then** ▷ Tractions for particles under compression
23: $\quad\quad\quad \sigma_{A\mathrm{Peak}} = \sigma_{\mathrm{AY}} + K\left(\log\Lambda_{\mathrm{peak}} - \log\Lambda_{\mathrm{YC}}\right)$ ▷ Peak axial stress for particles under compression
24: $\quad\quad\quad \sigma_{L\mathrm{Peak}} = \sigma_{\mathrm{LY}} + K\left(\log\Lambda_{\mathrm{peak}} - \log\Lambda_{\mathrm{YC}}\right)$ ▷ Peak lateral stress for particles under compression
25: $\quad\quad\quad$ **if** $\left(\log\left(\Lambda_{\mathrm{peak}}\right) - \log\left(\Lambda\right) <= \frac{Y}{G}\right)$ **then**
▷ Particles under compression during loading become plastic under tension during unloading
26: $\quad\quad\quad\quad \varepsilon_{\mathrm{PD}} = \log\Lambda_{\mathrm{peak}} - \frac{Y}{G}$ ▷ Strain at the slope discontinuity under unloading
27: $\quad\quad\quad\quad \sigma_{\mathrm{APD}} = \sigma_{A\mathrm{Peak}} - C\left(\frac{Y}{G}\right)$ ▷ Axial stress at the slope discontinuity under unloading
28: $\quad\quad\quad\quad \sigma_{\mathrm{LPD}} = \sigma_{L\mathrm{Peak}} - \lambda\left(\frac{Y}{G}\right)$ ▷ Axial stress at the slope discontinuity under unloading
29: $\quad\quad\quad\quad \sigma_{\mathrm{AUL}} = \sigma_{\mathrm{APD}} - K\left(\varepsilon_{\mathrm{PD}} - \log\Lambda\right)$ ▷ Lateral stress during plastic unloading
30: $\quad\quad\quad\quad \sigma_{\mathrm{LUL}} = \sigma_{\mathrm{LPD}} - K\left(\varepsilon_{\mathrm{PD}} - \log\Lambda\right)$ ▷ Lateral stress during plastic unloading
31: $\quad\quad\quad\quad \boldsymbol{\sigma} = [\ \sigma_{\mathrm{LUL}} \quad 0\ ; \quad 0 \quad \sigma_{\mathrm{AUL}}\ ]$
32: $\quad\quad\quad$ **else**
33: $\quad\quad\quad\quad \sigma_{\mathrm{AUL}} = \sigma_{A\mathrm{Peak}} - C\left(\log\Lambda_{\mathrm{peak}} - \log\Lambda\right)$ ▷ Axial stress during elastic unloading
34: $\quad\quad\quad\quad \sigma_{\mathrm{LUL}} = \sigma_{L\mathrm{Peak}} - \lambda\left(\log\Lambda_{\mathrm{peak}} - \log\Lambda\right)$ ▷ Lateral stress during elastic unloading
35: $\quad\quad\quad\quad \boldsymbol{\sigma} = [\ \sigma_{\mathrm{LUL}} \quad 0\ ; \quad 0 \quad \sigma_{\mathrm{AUL}}\ ]$
36: $\quad\quad\quad$ **end if** ▷ End for if block in line 25
37: $\quad\quad$ **else** ▷ Tractions for particles under tension
38: $\quad\quad\quad \sigma_{A\mathrm{Peak}} = \sigma_{\mathrm{AY}} + K\left(\log\Lambda_{\mathrm{peak}} - \log\Lambda_{\mathrm{YT}}\right)$ ▷ Peak axial stress for particles under tension
39: $\quad\quad\quad \sigma_{L\mathrm{Peak}} = \sigma_{\mathrm{LY}} + K\left(\log\Lambda_{\mathrm{peak}} - \log\Lambda_{\mathrm{YT}}\right)$ ▷ Peak lateral stress for particles under tension
40: $\quad\quad\quad$ **if** $\left(\log\left(\Lambda_{\mathrm{peak}}\right) - \log\left(\Lambda\right) >= \frac{Y}{G}\right)$ **then**
▷ Particles under tension during loading become plastic under compression during unloading
41: $\quad\quad\quad\quad \varepsilon_{\mathrm{PD}} = \log\Lambda_{\mathrm{peak}} - \frac{Y}{G}$ ▷ Strain at the slope discontinuity under unloading
42: $\quad\quad\quad\quad \sigma_{\mathrm{APD}} = \sigma_{A\mathrm{Peak}} - C\left(\frac{Y}{G}\right)$ ▷ Axial stress at the slope discontinuity under unloading
43: $\quad\quad\quad\quad \sigma_{\mathrm{LPD}} = \sigma_{L\mathrm{Peak}} - \lambda\left(\frac{Y}{G}\right)$ ▷ Lateral stress at the slope discontinuity under unloading
44: $\quad\quad\quad\quad \sigma_{\mathrm{AUL}} = \sigma_{\mathrm{APD}} - K\left(\varepsilon_{\mathrm{PD}} - \log\Lambda\right)$ ▷ Axial stress during plastic unloading
45: $\quad\quad\quad\quad \sigma_{\mathrm{LUL}} = \sigma_{\mathrm{LPD}} - K\left(\varepsilon_{\mathrm{PD}} - \log\Lambda\right)$ ▷ Lateral stress during plastic unloading
46: $\quad\quad\quad\quad \boldsymbol{\sigma} = [\ \sigma_{\mathrm{LUL}} \quad 0\ ; \quad 0 \quad \sigma_{\mathrm{AUL}}\ ]$
47: $\quad\quad\quad$ **else**
48: $\quad\quad\quad\quad \sigma_{\mathrm{AUL}} = \sigma_{A\mathrm{Peak}} - C\left(\log\Lambda_{\mathrm{peak}} - \log\Lambda\right)$ ▷ Axial stress during elastic unloading
49: $\quad\quad\quad\quad \sigma_{\mathrm{LUL}} = \sigma_{L\mathrm{Peak}} - \lambda\left(\log\Lambda_{\mathrm{peak}} - \log\Lambda\right)$ ▷ Lateral stress during elastic unloading
50: $\quad\quad\quad\quad \boldsymbol{\sigma} = [\ \sigma_{\mathrm{LUL}} \quad 0\ ; \quad 0 \quad \sigma_{\mathrm{AUL}}\ ]$
51: $\quad\quad\quad$ **end if** ▷ End for if block in line 40
52: $\quad\quad$ **end if** ▷ End for if block in line 22
53: $\quad$ **end if** ▷ End for if block in line 19
54: **end if** ▷ End for if block in line 10
55: For all points on the boundary of the domain, evaluate and apply the tractions: $\mathbf{t} = \boldsymbol{Q} \cdot \boldsymbol{\sigma} \cdot \mathbf{n}$, where $\boldsymbol{Q} = [\ \cos\left(\alpha\right) \quad -\sin\left(\alpha\right)\ ; \quad -\sin\left(\alpha\right) \quad \cos\left(\alpha\right)\ ]$, and $\mathbf{n}$ is the outward unit normal.

Using B=1.0m and H=8.0m, the problem domain spans from -B/2m to B/2m in the x-direction, and 0 to H in the y-direction.

The above algorithms for body forces and tractions were implemented in our in-house research MPM code, giving the results summarized in Figures 3.9–3.10. Cyan indicates the elastic particles, while red indicates the plastic particles. The thickness of the red plastic zone grows to a maximum at the end of the loading phase. This zone decreases in size during the unloading phase by elastic unloading. However, the effect of path dependence is evident from the fact that this zone does not completely disappear. Similar to the homogeneous deformation plasticity MMS in Sec. 3.3, this verification test can be used to verify von-Mises plasticity model or any model that includes von-Mises plasticity as a special case. Also, this problem (by running it for loading only) can be extended to verify a simpler case of a material deformation/stress state that includes linear-elasticity with von-Mises plasticity and constant strain-to-failure damage option. In particular, this section will allow the material to damage, thereby breaking the domain into five sections: damage in compression, damage in tension, yield in compression, yield in tension, surrounding an elastic core at the centerline.

3.4.1 Convergence study

Error definitions are the same as Eqs. (3.11) and (3.12) that were used in the previous section's convergence study. The simulations were run for four different mesh resolutions. Figures 3.11–3.12 show the convergence plots for displacements and stresses at the end of loading and unloading period. For displacements, the rate of convergence was 1.9 at the end of loading period and 0.46 at the end of unloading period. For stresses, the rate of convergence was 1.2 at the end of loading period and 1.1 at the end of unloading period.

3.5 Conclusions

This chapter presented two of method of manufactured solutions (MMS) under large deformations for von-Mises plasticity:

1. Transient spatially homogeneous uniaxial strain, though conceptually trivial, provides a crucial preliminary test of time-stepping algorithms for inelastic loading with a load reversal not commonly considered in other von-Mises verification tests. Convergence studies were performed to test the accuracy of the constitutive model and the momentum solver's traction boundary conditions, and body forces. This test also helps users to avoid a common error associated with nonstandardized definition of the phrase

"yield stress" (which varies among different constitutive models to usually be either yield in shear or yield in uniaxial stress).

2. A bending-bar MMS was developed for von-Mises plasticity *with load reversals*. This problem simultaneously confirms basis and frame indifference. Unlike similar-looking method of exact solutions (MES) verification tests in the literature, the MMS entails (for all points in space and time) a single common deformation mode: uniaxial strain with superimposed rotation. The forcing functions are applied through both the external body forces and applied tractions. Both of these problems can be used to verify the implementation of von-Mises plasticity model or any model that includes von-Mises plasticity as a special case [43, 15]. By exploiting the knowledge of strain at the end of loading, these problems (by running them for loading only) also can be extended to verify a simpler case of a material deformation/stress state that includes linear-elasticity with von-Mises plasticity and constant strain-to-failure damage option (*c.f.*, [44, 96]).

3.6 Analytical derivations of forcing functions

3.6.1 Derivation of analytical forcing functions for bending bar problem

Though the derivations of the analytical forcing functions for the loading part are identical as provided in the Chapter 2 (also, repeated here for relevance), the complication increases for unloading. Also, the previous derivation was for nonlinear elastic constitutive model, whereas the derivation is extended here for a more complicated path-dependent model. The equation of motion in terms of Cauchy stress is given by:

$$\mathrm{div}\boldsymbol{\sigma} + \rho\mathbf{b} = \rho\mathbf{a}\ , \tag{3.13}$$

where $\mathbf{a}$ is the acceleration, $\mathbf{b}$ is the body force, $\boldsymbol{\sigma}$ is the Cauchy stress, ρ_o is the initial density, and $\mathrm{div}\boldsymbol{\sigma}$ is the backward spatial divergence of $\boldsymbol{\sigma}$, having its i^{th} component given by $\partial\sigma_{ij}/\partial x_j$ (where repeated indices are implicitly summed from 1 to 3).

From Fig. 3.13, the corresponding mapping from an initial position $\mathbf{X}$ to deformed position $\mathbf{x}$ is

$$\begin{pmatrix} x_1 \\ x_2 \end{pmatrix} = \begin{pmatrix} \frac{-H}{\beta} + \left(\frac{H}{\beta} + X_1\right)\cos\left(\frac{\beta X_2}{H}\right) \\ \left(\frac{H}{\beta} + X_1\right)\sin\left(\frac{\beta X_2}{H}\right) \end{pmatrix}\ . \tag{3.14}$$

As can be confirmed by direct substitution, the following sequence of calculations decomposes the deformation gradient into rotation and stretch $\mathbf{F} = \mathbf{R} \cdot \mathbf{U}$, where $\mathbf{R}$ is the rotation tensor and $\mathbf{U}$ is the stretch tensor:

$$\alpha = \frac{\beta[t] X_2}{H}, \qquad \lambda = \frac{\beta[t] X_1}{H} + 1, \tag{3.15a}$$

$$\mathbf{R} = \begin{pmatrix} \cos\alpha & -\sin\alpha & 0 \\ \sin\alpha & \cos\alpha & 0 \\ 0 & 0 & 1 \end{pmatrix}, \qquad \mathbf{U} = \begin{pmatrix} 1 & 0 & 0 \\ 0 & \lambda & 0 \\ 0 & 0 & 1 \end{pmatrix}. \tag{3.15b}$$

Here, α is the angle of rotation at the material point of interest, λ is the amount of stretch in the 2-direction. For uniaxial strain in the 2-direction, the rotation is $\mathbf{R} = \mathbf{I}$, and therefore the deformation gradient is $\mathbf{F} = \mathbf{U}$, and the Jacobian is λ.

In the MMS, we assume that we have all the information in (3.13) except the body force. It is possible (*e.g.,* by running a single-element model driver) to obtain all stress components as a function of uniaxial strain stretching in the 2-direction *without rotation* for von-Mises plasticity. The upcoming analysis presumes only that the response functions for all components of stress under uniaxial strain in the 2-direction are known. During loading, the stress is just a function of λ, whereas during unloading, the stress is function of both λ and λ_{peak} *i.e.,*

$$[\bar{\boldsymbol{\sigma}}]_{\mathbf{L}} = \begin{bmatrix} \sigma_{11}[\lambda] & \sigma_{12}[\lambda] & \sigma_{13}[\lambda] \\ \sigma_{21}[\lambda] & \sigma_{22}[\lambda] & \sigma_{23}[\lambda] \\ \sigma_{31}[\lambda] & \sigma_{32}[\lambda] & \sigma_{33}[\lambda] \end{bmatrix}, \tag{3.16}$$

$$[\bar{\boldsymbol{\sigma}}]_{\mathbf{UL}} = \begin{bmatrix} \sigma_{11}[\lambda,\ \lambda_{peak}] & \sigma_{12}[\lambda,\ \lambda_{peak}] & \sigma_{13}[\lambda,\ \lambda_{peak}] \\ \sigma_{21}[\lambda,\ \lambda_{peak}] & \sigma_{22}[\lambda,\ \lambda_{peak}] & \sigma_{23}[\lambda,\ \lambda_{peak}] \\ \sigma_{31}[\lambda,\ \lambda_{peak}] & \sigma_{32}[\lambda,\ \lambda_{peak}] & \sigma_{33}[\lambda,\ \lambda_{peak}] \end{bmatrix}. \tag{3.17}$$

Then the Cauchy stress $\boldsymbol{\sigma}$ is computed using

$$\boldsymbol{\sigma} = \mathbf{R} \cdot \bar{\boldsymbol{\sigma}} \cdot \mathbf{R}^{\mathbf{T}}, \tag{3.18}$$

where $\mathbf{R}$ is the rotation tensor. The indicial form for (3.18) is given by

$$\frac{\partial \sigma_{ij}}{\partial x_j} = \frac{\partial}{\partial x_j}(R_{im} \cdot \bar{\sigma}_{mn} \cdot R_{jn}). \tag{3.19}$$

By the product rule,

$$\frac{\partial \sigma_{ij}}{\partial x_j} = \frac{\partial (R_{im})}{\partial x_j}\ \bar{\sigma}_{mn} R_{jn} + R_{im} \bar{\sigma}_{mn}\ \frac{\partial (R_{jn})}{\partial x_j} + R_{im}\ \frac{\partial \bar{\sigma}_{mn}}{\partial x_j}\ R_{jn}. \tag{3.20}$$

Noting from (3.15) that the polar rotation $\mathbf{R}$ depends only on the rotation angle α, using the chain rule

$$\frac{\partial (R_{im})}{\partial x_j} = \frac{d(R_{im})}{d\alpha}\ \frac{\partial \alpha}{\partial x_j}, \tag{3.21a}$$

$$\frac{d\mathbf{R}}{d\alpha} = \mathbf{A}\cdot\mathbf{R}, \quad \text{where} \quad \mathbf{A} = \begin{pmatrix} 0 & -1 & 0 \\ 1 & 0 & 0 \\ 0 & 0 & 0 \end{pmatrix} , \tag{3.21b}$$

$$\frac{\partial\alpha}{\partial x_j} = \frac{d\alpha}{dX_s}\,\frac{\partial X_s}{\partial x_j} = \frac{d\alpha}{dX_s}\,F^{-1}_{sj} = \frac{d\alpha}{dX_s}\,U^{-1}_{sa}\,R_{ja}\,. \tag{3.21c}$$

Using (3.21b), (3.21c) and substituting in (3.21a),

$$\frac{\partial R_{im}}{\partial x_j} = A_{ip}\,R_{pm}\,\frac{d\alpha}{dX_s}\,U^{-1}_{sa}\,R_{ja}\,. \tag{3.22}$$

This implies that

$$\frac{\partial R_{jn}}{\partial x_j} = A_{jp}\,R_{pn}\,\frac{d\alpha}{dX_s}\,U^{-1}_{sa}\,R_{ja}\,. \tag{3.23}$$

Using (3.22) and (3.23) , (3.20) can be reduced to

$$f_i = \frac{\partial\sigma_{ij}}{\partial x_j} = A_{ip}\,R_{pm}\,\frac{d\alpha}{dX_s}\,U^{-1}_{sa}\,R_{ja}\,\bar{\sigma}_{mn}\,R_{jn} + R_{im}\,\frac{\partial\bar{\sigma}_{mn}}{\partial x_j}\,R_{jn} + R_{im}\,\bar{\sigma}_{mn}\,A_{jp}\,R_{pn}\,\frac{d\alpha}{dX_s}\,U^{-1}_{sa}\,R_{ja}\,. \tag{3.24}$$

Multiplying both sides of (3.24) using R_{iq} and simplifying using the fact that $\mathbf{R}$ is orthogonal

$$\bar{f}_q = R_{iq}\,\frac{\partial\sigma_{ij}}{\partial x_j} = A_{qm}\,\frac{d\alpha}{dX_s}\,U^{-1}_{sn}\,\bar{\sigma}_{mn} + \frac{\partial\bar{\sigma}_{qn}}{\partial x_j}\,R_{jn} + \bar{\sigma}_{qn}\,A_{qn}\,\frac{d\alpha}{dX_s}\,U^{-1}_{sa}\,. \tag{3.25}$$

The subsequent derivation will be split into two parts *i.e.,* evaluating $\frac{\partial\bar{\sigma}_{qn}}{\partial x_j}$ separately for loading and unloading.

3.6.2 Stress divergence during loading

Recalling from (3.16) that, during loading, $\boldsymbol{\sigma}$ depends only on λ, and from (3.15) that λ depends only on $\boldsymbol{X}$

$$\frac{\partial\bar{\sigma}_{qn}}{\partial x_j} = \frac{\partial\bar{\sigma}_{qn}}{\partial\lambda}\,\frac{\partial\lambda}{\partial x_j} = \frac{\partial\bar{\sigma}_{qn}}{\partial\lambda}\,\frac{\partial\lambda}{\partial X_p}\,\frac{\partial X_p}{\partial x_j} = \frac{\partial\bar{\sigma}_{qn}}{\partial\lambda}\,\frac{\partial\lambda}{\partial X_p}\,U^{-1}_{pt}\,R_{jt}\,. \tag{3.26}$$

Using the definitions of λ, $\mathbf{U}$ and $\mathbf{A}$ and substituting (3.26) in (3.25), we have

$$\bar{f}_q = R_{iq}\,\frac{\partial\sigma_{ij}}{\partial x_j} = \frac{\beta}{H\lambda}(A_{q1}\,\bar{\sigma}_{12} + A_{q2}\,\bar{\sigma}_{22} + \lambda\,\frac{\partial\bar{\sigma}_{q1}}{\partial\lambda} + \bar{\sigma}_{q1})\,. \tag{3.27}$$

Thus, the unrotated force components are

$$\bar{f}_1 = \frac{\beta}{H\lambda}(-\bar{\sigma}_{22} + \lambda\frac{\partial\bar{\sigma}_{11}}{\partial\lambda} + \bar{\sigma}_{11})\,, \tag{3.28a}$$

$$\bar{f}_2 = \frac{\beta}{H\lambda}(\bar{\sigma}_{12} + \lambda\frac{\partial\bar{\sigma}_{21}}{\partial\lambda} + \bar{\sigma}_{21})\,, \tag{3.28b}$$

$$\bar{f}_3 = \frac{\beta}{H\lambda}(\lambda\frac{\partial\bar{\sigma}_{31}}{\partial\lambda} + \bar{\sigma}_{31}). \tag{3.28c}$$

These apply even for an anisotropic constitutive model. For a special case case of an isotropic constitutive model, the unrotated stress will be diagonal, giving

$$\bar{f}_1 = \frac{\beta}{H\lambda}(-\bar{\sigma}_{22} + \lambda\frac{\partial\bar{\sigma}_{11}}{\partial\lambda} + \bar{\sigma}_{11}) \,, \tag{3.29a}$$

$$\bar{f}_2 = 0, \tag{3.29b}$$

$$\bar{f}_3 = 0. \tag{3.29c}$$

3.6.3 Stress divergence during unloading

Recalling from (3.17) that, during unloading, $\boldsymbol{\sigma}$ depends on λ and λ_{peak}, where λ_{peak} is the peak value of λ (value of λ at the end of loading period). From (3.15), λ depends only on $\boldsymbol{X}$, which implies λ_{peak} also depends only on $\boldsymbol{X}$.

$$\frac{\partial\bar{\sigma}_{qn}}{\partial x_j} = \frac{\partial\bar{\sigma}_{qn}}{\partial\lambda}\,\frac{\partial\lambda}{\partial x_j} + \frac{\partial\bar{\sigma}_{qn}}{\partial\lambda_{peak}}\,\frac{\partial\lambda_{peak}}{\partial x_j} = \frac{\partial\bar{\sigma}_{qn}}{\partial\lambda}\,\frac{\partial\lambda}{\partial X_p}\,\frac{\partial X_p}{\partial x_j} + \frac{\partial\bar{\sigma}_{qn}}{\partial\lambda_{peak}}\,\frac{\partial\lambda_{peak}}{\partial X_p}\,\frac{\partial X_p}{\partial x_j} \tag{3.30}$$

$$= \frac{\partial\bar{\sigma}_{qn}}{\partial\lambda}\,\frac{\partial\lambda}{\partial X_p}\,U^{-1}_{pt}\,R_{jt} + \frac{\partial\bar{\sigma}_{qn}}{\partial\lambda_{peak}}\,\frac{\partial\lambda_{peak}}{\partial X_p}\,U^{-1}_{pt}\,R_{jt}\,. \tag{3.31}$$

Using the definitions of λ, λ_{peak}, $\mathbf{U}$ and $\mathbf{A}$ and substituting (3.31) in (3.25), we have

$$\bar{f}_q = R_{iq}\,\frac{\partial\sigma_{ij}}{\partial x_j} = \frac{\beta}{H\lambda}(A_{q1}\,\bar{\sigma}_{12} + A_{q2}\,\bar{\sigma}_{22} + \lambda\,\frac{\partial\bar{\sigma}_{q1}}{\partial\lambda} + \frac{\lambda\beta_{\max}}{\beta}\,\frac{\partial\bar{\sigma}_{q1}}{\partial\lambda_{peak}} + \bar{\sigma}_{q1}). \tag{3.32}$$

Thus, the unrotated force components are

$$\bar{f}_1 = \frac{\beta}{H\lambda}(-\bar{\sigma}_{22} + \lambda\frac{\partial\bar{\sigma}_{11}}{\partial\lambda} + \frac{\lambda\beta_{\max}}{\beta}\,\frac{\partial\bar{\sigma}_{11}}{\partial\lambda_{peak}} + \bar{\sigma}_{11}), \tag{3.33a}$$

$$\bar{f}_2 = \frac{\beta}{H\lambda}(\bar{\sigma}_{12} + \lambda\frac{\partial\bar{\sigma}_{21}}{\partial\lambda} + \frac{\lambda\beta_{\max}}{\beta}\,\frac{\partial\bar{\sigma}_{21}}{\partial\lambda_{peak}} + \bar{\sigma}_{21}), \tag{3.33b}$$

$$\bar{f}_3 = \frac{\beta}{H\lambda}(\lambda\frac{\partial\bar{\sigma}_{31}}{\partial\lambda} + \frac{\lambda\beta_{\max}}{\beta}\,\frac{\partial\bar{\sigma}_{31}}{\partial\lambda_{peak}} + \bar{\sigma}_{31}). \tag{3.33c}$$

These apply even for an anisotropic constitutive model. For a special case case of an isotropic constitutive model, the unrotated stress will be diagonal, giving

$$\bar{f}_1 = \frac{\beta}{H\lambda}(-\bar{\sigma}_{22} + \lambda\frac{\partial\bar{\sigma}_{11}}{\partial\lambda} + \frac{\lambda\beta_{\max}}{\beta}\,\frac{\partial\bar{\sigma}_{11}}{\partial\lambda_{peak}} + \bar{\sigma}_{11}), \tag{3.34a}$$

$$\bar{f}_2 = 0, \tag{3.34b}$$

$$\bar{f}_3 = 0. \tag{3.34c}$$

These are the unrotated force components. To apply these in a calculation of the body force for the manufactured solution, the actual force vector can be computed by recalling that $\boldsymbol{f} = \mathbf{R} \cdot \bar{\boldsymbol{f}}$. In general, this comes out to be in the form

$$\boldsymbol{f} = f_r \boldsymbol{e}_r + f_\theta \boldsymbol{e}_\theta. \tag{3.35}$$

The force contribution from the material acceleration is relatively easy because we already have the relation between $\boldsymbol{x}$ and $\boldsymbol{X}$. Acceleration is simply

$$\boldsymbol{a} = \left(\frac{\partial^2 \boldsymbol{x}}{\partial t^2} \right)_{\boldsymbol{X}} = \frac{\partial^2 \boldsymbol{x}}{\partial \beta^2} \left(\frac{d\beta}{dt} \right)^2 + \frac{\partial \boldsymbol{x}}{\partial \beta} \frac{\partial^2 \beta}{\partial t^2} \, , \tag{3.36}$$

where the derivatives with respect to β are found by differentiating (3.15). The result gives the cartesian components of acceleration which must be converted to polar components to give a final acceleration of the form

$$\boldsymbol{a} = a_r \boldsymbol{e}_r + a_\theta \boldsymbol{e}_\theta \, . \tag{3.37}$$

Density is

$$\rho = \frac{\rho_0}{\lambda} \, . \tag{3.38}$$

Substituting (3.38), (3.36), and (3.35) in (3.13) after choosing the material model and material constants, the total body force required for this deformation is:

$$\boldsymbol{b} = b_r \boldsymbol{e}_r + b_\theta \boldsymbol{e}_\theta \, , \tag{3.39}$$

where

$$b_r = a_r - \frac{f_r}{\rho}, \quad b_\theta = a_\theta - \frac{f_\theta}{\rho} \, . \tag{3.40}$$

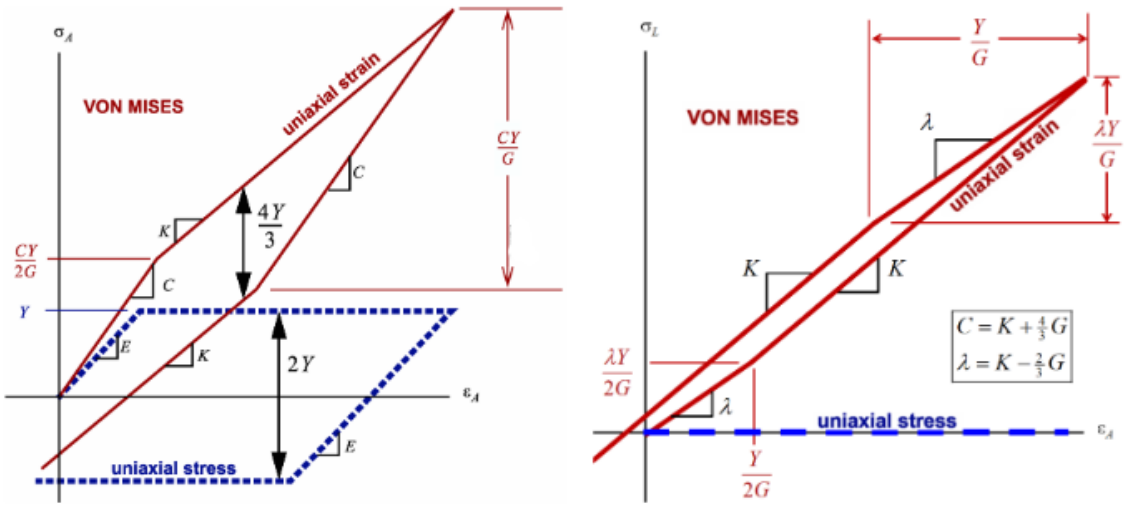

Figure 3.1: Analytical solutions under uniaxial strain/stress for a linear-elastic, perfectly-plastic material (*c.f.* [14])

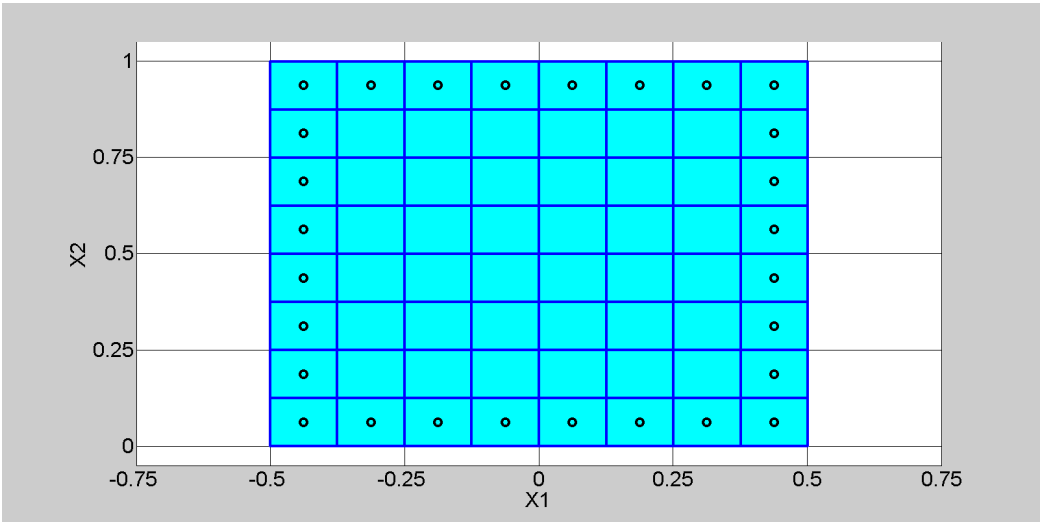

Figure 3.2: Initial configuration (corresponding to time $t = 0$s). Cyan indicates that particles are elastic

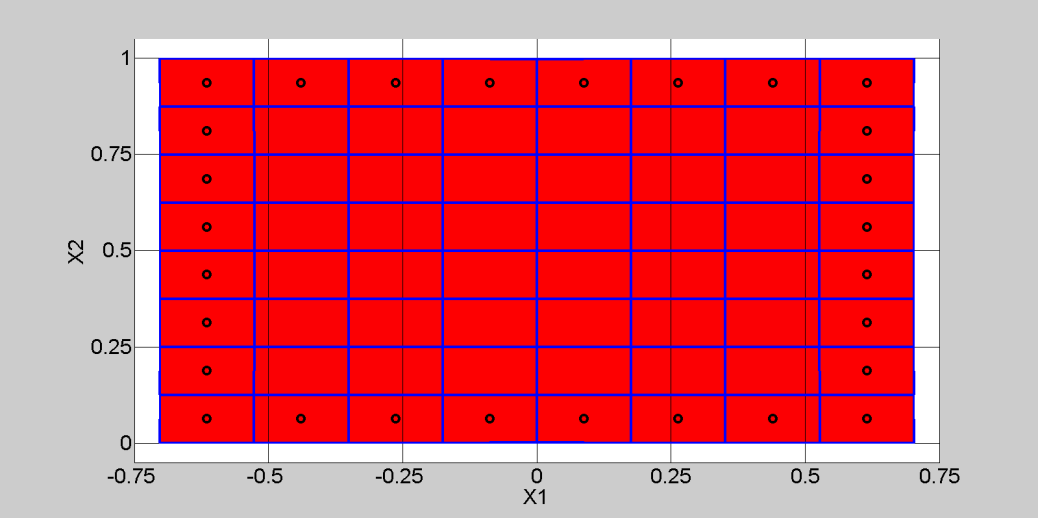

Figure 3.3: Final configuration at the end of loading phase (corresponding to time $t = 0.5$s). Red indicates plastic

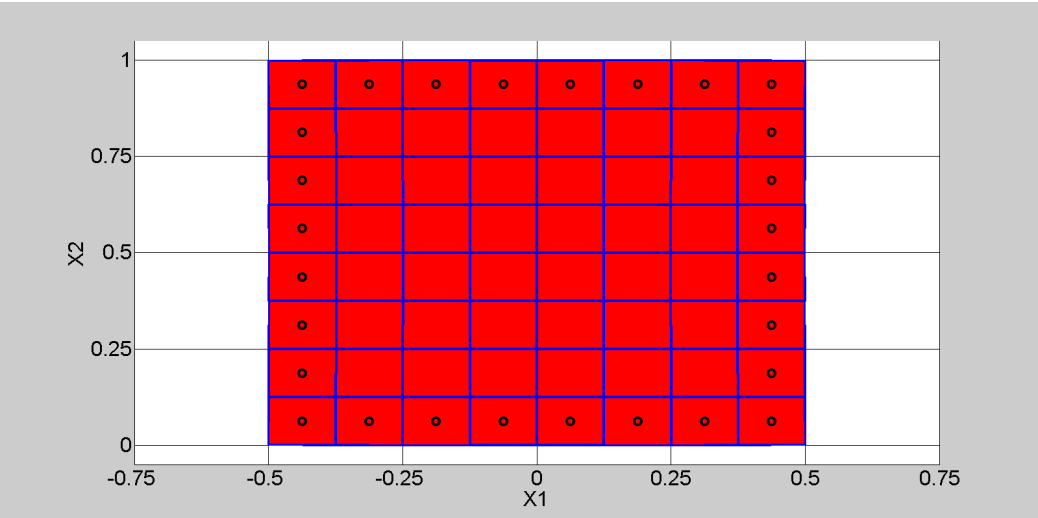

Figure 3.4: Final configuration at the end of unloading phase (corresponding to time $t = 1$s). Red indicates plastic residual stress

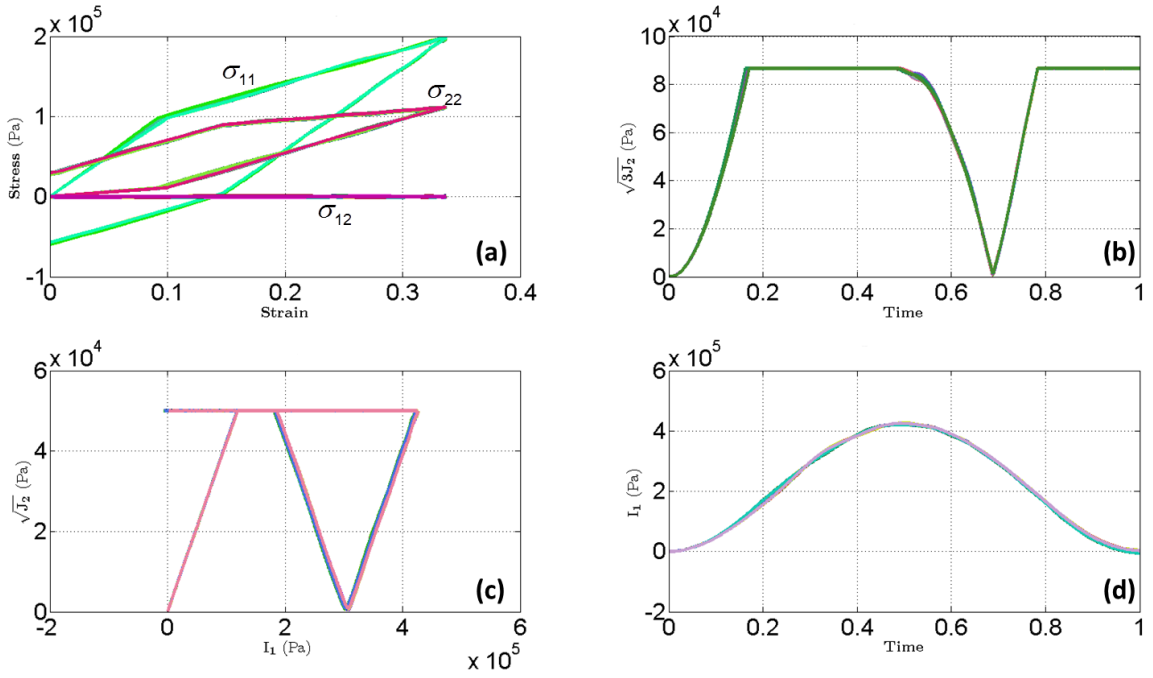

Figure 3.5: Plot of (a) stress components vs. axial strain (b) $\sqrt{3J_2}$ vs. time t (c) $\sqrt{J_2}$ vs. I_1 (d) I_1 vs. time t

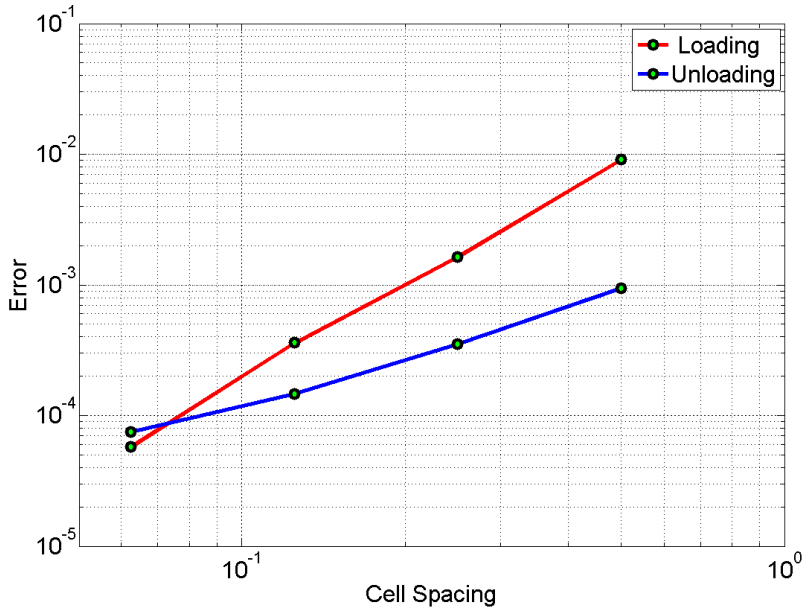

Figure 3.6: Convergence plot for displacement at the end of loading (corresponding to time $t = 0.5$s) and unloading (corresponding to time $t = 1$s)

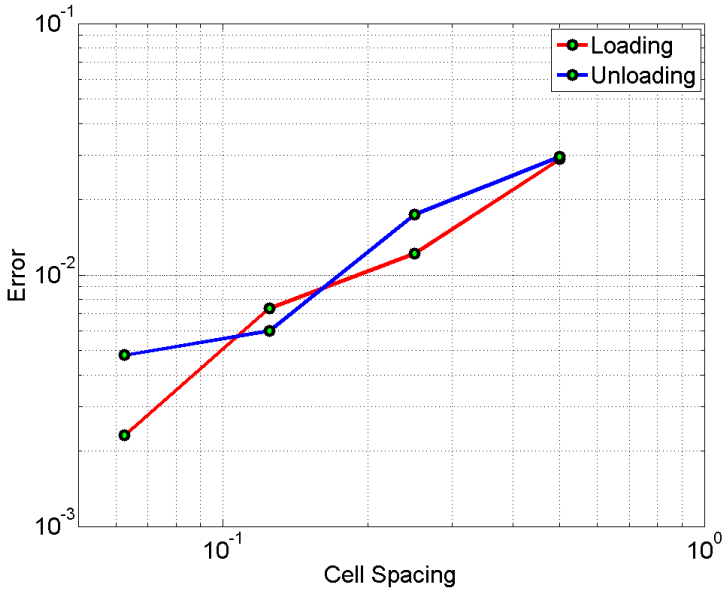

Figure 3.7: Convergence plot for stress at the end of loading (corresponding to time $t = 0.5$s) and unloading (corresponding to time $t = 1$s)

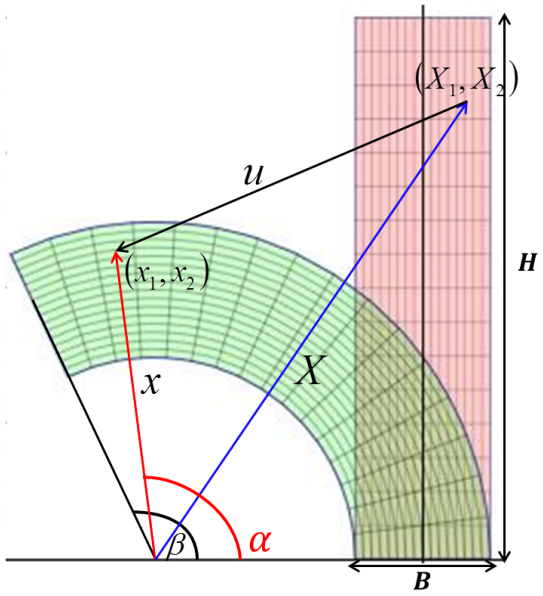

Figure 3.8: Snapshot of deformation in time for the bending bar problem

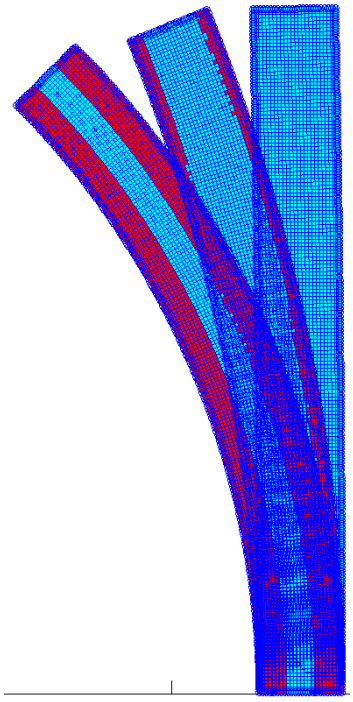

Figure 3.9: Snapshot of deformation during loading

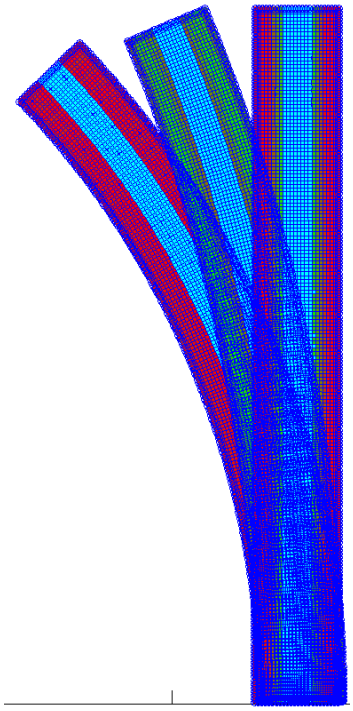

Figure 3.10: Snapshot of deformation during unloading

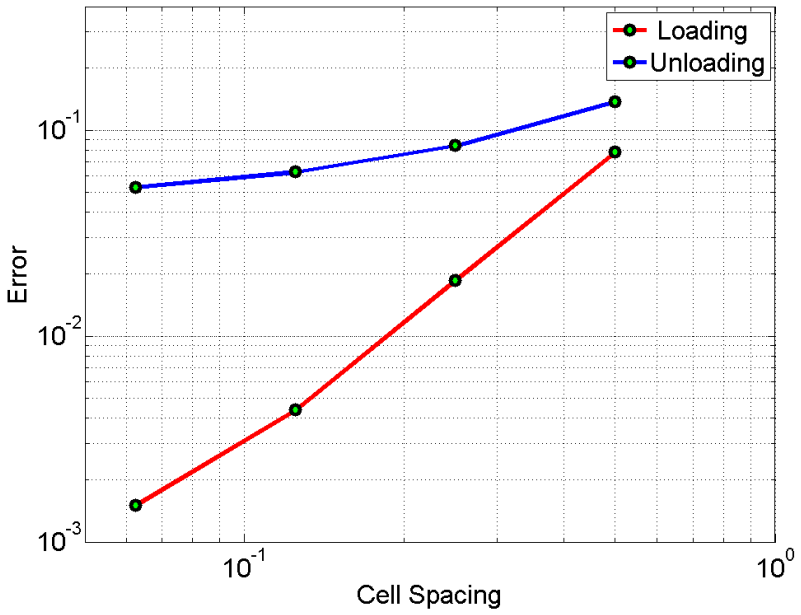

Figure 3.11: Convergence plot for displacement at the end of loading (corresponding to time $T = 0.5s$) and unloading (corresponding to time $T = 1s$) period

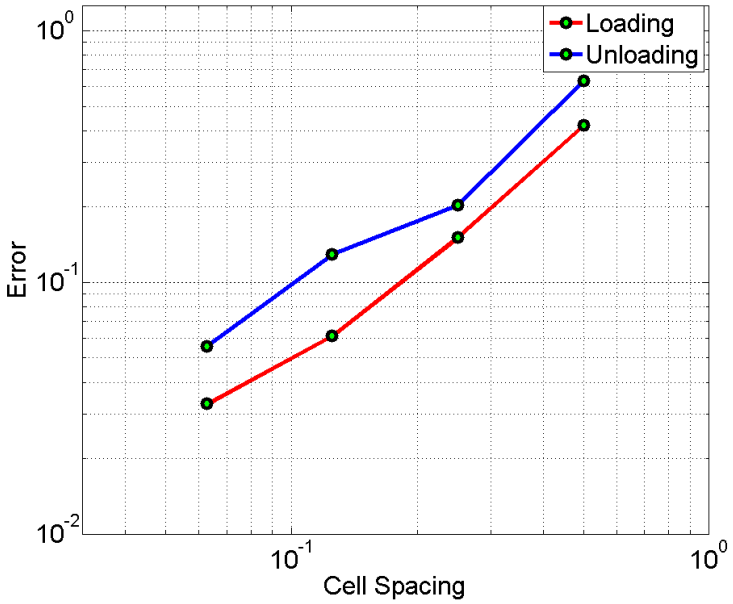

Figure 3.12: Convergence plot for stress at the end of loading (corresponding to time $T = 0.5s$) and unloading (corresponding to time $T = 1s$) period

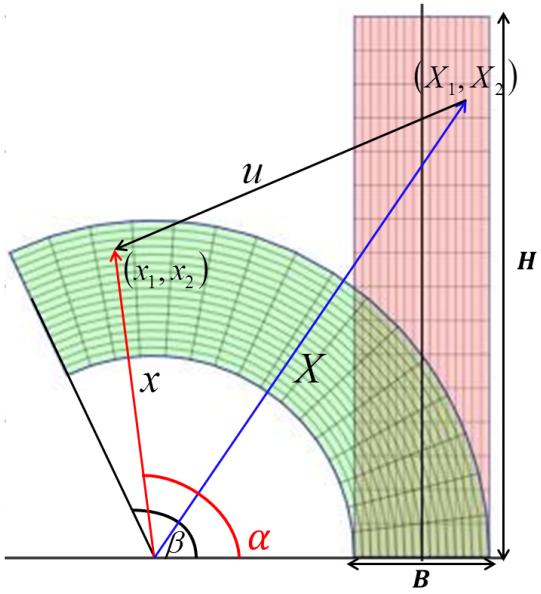

Figure 3.13: Snapshot of deformation in time for the bending bar problem

CHAPTER 4

VALIDATION STUDY OF UNNOTCHED CHARPY AND TAYLOR-ANVIL IMPACT EXPERIMENTS

4.1 Abstract

Validation of a single computational model with multiple available strain-to-failure fracture theories is presented through experimental tests and numerical simulations of the standardized unnotched Charpy and Taylor-anvil impact tests, both run using the same material model (Kayenta). Unnotched Charpy tests are performed on rolled homogeneous armor steel. The fracture patterns using Kayenta's various failure options that include aleatory uncertainty and scale effects are compared against the experiments. Other quantities of interest include the average value of the absorbed energy and bend angle of the specimen.

Taylor-anvil impact tests are performed on Ti6Al4V titanium alloy. The impact speeds of the specimen are 321 m/s and 393 m/s. The goal of the numerical work is to reproduce the damage patterns observed in the laboratory. For the numerical study, the Johnson-Cook failure model [44] is used as the ductile fracture criterion, and aleatory uncertainty is applied to rate-dependence parameters to explore its effect on the fracture patterns.

4.2 Introduction

Applications in defense, aerospace, *etc.* use high-strength metals and alloys that can resist penetration and damage. Rolled homogeneous armor (RHA) steel is one of the most commonly used materials in armored vehicles and ammunition testing because of its low cost and structural efficiency (*c.f.,* , [62]). Titanium alloys are primarily used in aerospace applications (*c.f.,* , [13]) because of their high strength at extreme temperatures and im-

This chapter has been submitted as INL lab report and is under review.

munity to corrosion. Predictive simulations of damage in such high-strength materials is of ongoing interest for the scientific community. Several strain-to-failure models, including void-growth models [35, 61, 71] and conventional damage models [97, 44, 6] have been proposed in the literature to quantify damage. In void-growth models, damage is assumed to initiate when the void volume reaches a critical value. Generally, in conventional damage models, a scalar damage variable increases from zero to unity (fully damaged state) under plastic loading, and these models assume no coupling between plasticity and damage. The disadvantage of these conventional models is that there is no loss of strength or stiffness until the scalar damage variable reaches unity. In Kayenta, softening is related to material strength, and the material progressively loses stiffness and load carrying capacity when it undergoes irreversible damage. The rate of damage progression can be controlled so that Kayenta can emulate a broad range of other conventional damage models, which facilitates deciding which of them (if any) appears to be imposing desirable model behaviors. This chapter provides a systematic validation study on damage for the unnotched Charpy test (performed on RHA steel) and the Taylor-anvil impact test (performed on Ti6Al4V alloy) using Kayenta. Sections 4.3 and 4.4 provide the experimental details and the numerical study performed on the unnotched Charpy test. And the subsequent Secs. 4.5 and 4.6 provide the details on the Taylor-anvil impact tests.

The Charpy test [21] is a standardized test used to determine impact toughness, which is quantified by the amount of energy absorbed by the specimen before fracture. The specimen is supported against two anvils, and a pendulum with a striker is released to impact the specimen. For validating the unnotched Charpy test, the quantities of interest for comparison are the bend angle of the specimen and the amount of energy absorbed by the specimen. As per ASTM E23 [1] standard, "the absorbed energy is taken as the difference between the energy in the striking member at the instant of impact with the specimen, and the energy remained after breaking the specimen." The Taylor-anvil impact test on the other hand, is used to determine the dynamic behavior of materials at high strain rates. Ref [89] first impacted a cylindrical specimen on a flat rigid target to determine the dynamic yield stress. Countless papers about the Taylor-anvil impact test may be found in the literature. Most of the experimental [100, 60], and numerical [32, 90] work for the Taylor-anvil impact test focused on determining the constitutive model coefficients and dynamic yield stresses, but relatively few papers presented the numerical predictions of fracture mechanisms [101, 69] observed in the Taylor-anvil impact tests. This chapter provides a validation study aimed at assessing which features in prevailing damage and

plasticity models appear to be important to reproduce fracture patterns observed in the laboratory for Taylor-anvil impact tests on Ti6Al4V.

4.3 Experimental data on unnotched Charpy test

Six unnotched Charpy experiments were conducted on RHA steel at Idaho National Laboratory. The RHA specimens were tested in a machine meeting the requirements of ASTM E23 [1]. The pendulum was a C-type, with anvil and striker geometry conforming to that of the standard [1]. The impactor mass was 60 lb (27.26 kg). Given the arm radius, the striker velocity was calculated to be 5.147 m/s. All tests were conducted with the same procedure (no striker or velocity changes). Striker kinetic energy was on the order of 361 J (266 ft-lbf), and the specimen dimensions were $5 \times 10 \times 55$ mm. The average value of the absorbed energy, and bend angle in these six experiments was taken as the measure for comparison of the experimental data and numerical simulations. Figure 4.1 shows the deformed specimens with the damage patterns at the bottom (convex side) of the specimen. Large plastic deformation with multiple cracks on the tension surface was observed. The average amount of energy absorbed in Fig. 4.2 was 106.833 ft-lbs (144.84 Joules), and the average bend angle was 95°. The definition used to calculate the amount of energy absorbed in the specimen from numerical simulations was

- Initial K.E. of the striker - Final K.E. of the striker

where K.E. is the kinetic energy. This is likely to be the upper bound on the *inelastic* absorbed energy since it does not remove reversible elastic stored energy. Bending angle definition was also taken from Ref [1].

4.4 Numerical simulations of unnotched Charpy test

All of the numerical simulations described herein use the open-source Uintah MPM framework [34] and Kayenta [15] as the constitutive model. In classical Kayenta softening routines, TFAIL and TGROW are the two parameters that control the softening. TFAIL is the material-specific characteristic failure time for a given loading condition and element size. When using the strain-to-failure option in Kayenta, TFAIL is set to an appropriate, dynamically adjusted, value that would produce failure at the designated strain if the the strain rate calculated in the problem were to be held constant. A numerical study was performed on the unnotched Charpy test using the following softening options available in Kayenta :

- Time-to-failure
- Constant strain-to-failure
- Johnson-Cook failure

2D and 3D damage simulations are presented in Sec. 4.4.1 using the deterministic scale-insensitive model, where nonconvergence is evident. Section 4.4.2 shows improved results when using statistical variability in strength and scale effects.

4.4.1 Simulations using deterministic model

Figure 4.3 shows the convergence study on damage for 2D plane-strain simulations using the different softening options in Kayenta. Mesh resolution increases from left to right. Red indicates damage and blue indicates intact material. For all softening options, damage zone does not converge with mesh refinement. Since these simulations were symmetric about the vertical axis, the results using this deterministic option should (and do) exhibit the same symmetry. Comparing these 2D simulations against the experiments, the Johnson-cook failure option was under-predicting damage in the specimen, and the time-to-failure option was over-predicting damage in the specimen. For the constant strain-to-failure softening option, the strain-to-failure was chosen to be 0.3.

When the same simulations were run in 3D (Fig. 4.4), similar predictions to the 2D simulations were observed with the time-to-failure softening option over-predicting the damage and Johnson-Cook softening under-predicting the damage compared to the experiments. The prediction using a constant strain-to-failure softening option was closer to the experiments, but convergence issues persisted. Ref [17] considerably reduced mesh sensitivity in axisymmetric dynamic sphere-indentation problems using statistical variability of strength and scale effects. The same features were therefore explored on unnotched Charpy simulations, which are detailed in the next section.

4.4.2 Simulations using statistical variability of strength and scale effects

Verification of the implementation of statistics in strength was performed using trend tests by running 2D plane-strain simulations of the unnotched Charpy test.

Figure 4.5 shows the variable strength assigned to each particle. The simulations in the top row of Fig. 4.3 were re-run using statistical variability in strength. Since these simulations were run with variability, as expected, the results predicted the loss of symmetry

which can be seen in Fig. 4.6. Once the implementation of statistics in strength was verified using these trend tests, 3D simulations were run using this feature.

To make the simulations complete faster, and also to investigate the rate effects on the specimen damage patterns, the initial research was conducted by running these simulations at a striker velocity 10 times that used in the experiments. Results using realistic striker speeds are discussed later in this section. Figure 4.7 shows the plot of damage using constant strain-to-failure of 0.3. Moving from top to bottom in that figure corresponds to tripling the fracture speed, and moving from left to right corresponds to tripling the Weibull modulus (*i.e.,* a decrease in variability). All of these simulations were run at the same mesh resolution. Figure 4.8 is the same as Fig. 4.7, except the strain-to-failure was chosen to be 0.4. As seen in these figures, increasing FSPEED noticeably increases the size of the damage zone, whereas increasing the Weibull modulus (*i.e.,* reducing variability) decreases the size of the damage zone.

A similar investigation was performed using Johnson-Cook damage parameters provided by INL, using both Uintah's Johnson-Cook model and Kayenta with the Johnson-Cook option. In both cases, the Johnson-Cook damage model was predicting failure at total accumulated strain values close to 1.0. Since those values were actually not reached in the simulation, complete damage of the specimen was not predicted. Figure 4.9 shows the plot of scalar damage predicted by the Johnson-Cook fracture model. Moving from left to right corresponds to tripling the Weibull modulus. These parameters do not have any significant effect on the damage pattern.

Figure 4.10 shows the damage patterns, the amount of energy absorbed, and the bend angle for the simulations that were run at 10 *times the striker speed* that was used in the experiments. The simulations were run using the constant-strain-failure softening model in Kayenta. Moving from left to right corresponds to tripling the Weibull modulus (*i.e.,* a decrease in variability of strength), and moving from top to bottom corresponds to increasing failure strain from 0.3 to 0.4. As seen in this figure, increasing the Weibull modulus or increasing failure strain decreases the size of the damage zone. The average bend angle calculated from these simulations was 7.7% higher than those observed in the experiments. The average amount of energy absorbed (Initial K.E. Striker - Final K.E. Striker) was 24% higher compared to the experiments. Keep in mind, however, that these simulations were run using a higher striking speed than were used in the actual experiments.

The Kayenta parameter called FSPEED controls the rate of loss in strength in the material after softening starts to occur. A large value of FSPEED makes Kayenta emulate the first Johnson-Holmquist (JH-1) model, while a lower value emulates the JH-2 model [45].

Below, it is shown that realistic striker speeds give much better agreement with the data. Unsurprisingly, this shows that impact speeds have significant influence on absorbed energy and bend angle.

Figure 4.11 shows the same simulations as in Fig. 4.10, except the striker speed is the actual speed ($5.147\frac{m}{s}$) calculated in the experiments. The trend in damage patterns is similar to Fig. 4.10, but quantitative results were much closer to experimental values. The average bend angle calculated from these simulations was 0.4% higher than those observed in the experiments. The average amount of energy (Initial K.E. Striker - Final K.E. Striker) absorbed was 1.2% lower compared to the experiments.

All of the simulations presented so far were run at one mesh size. When refining the mesh, scale effects are expected to be needed for convergence with mesh refinement. In particular, smaller domains (*e.g.,* smaller elements) are stronger on average and also more variable so that, in principle, the probability of failure initiation of a given domain is insensitive to whether that domain is subdivided into few or many elements [86]. Scale effects for progression of failure following initiation remains a subject of active research [33]. In light of a known tendency for damage simulations to be mesh sensitive [91, 16], two convergence studies were performed on the unnotched Charpy problem using Kayenta's strain-to-failure option (with the failure strain chosen to be 0.3). The speed of the striker was the same as in the experiments. In the first convergence study, strength was statistically variable, but no scale effects were imposed. The three cell spacings and the absorbed energy are listed in the Table 4.1. The second convergence study includes scale effects in order to assess whether or not they tend to at least mitigate mesh sensitivity.

The plot for the time history of the K.E. of the striker in the convergence study without scale effects can be seen in Fig. 4.12. The rate of K.E. absorbed by the specimen is almost constant for mesh 1 and mesh 2. For mesh 3, the rate of absorbed K.E. decreases during the simulation and tends towards a steady-state value, thus indicating that the fine mesh is predicting less striker K.E. being absorbed by the specimen. The results show mesh convergence prior to specimen damage, but nonconvergence during the softening phase. Such behavior is a typical and as-yet unresolved problem for softening models that lack scale effects, thus motivating us to perform the convergence study again using both statistical variability in strength and scale effects to see if this issue could be resolved. The resulting time histories of the K.E. of the striker can be seen in Fig. 4.13.

Both cases show similar trends, with inclusion of scale effects only slightly mitigating nonconvergence during the later times. To illustrate the influence of scale effects, Fig.

4.14 shows the color plots of damage for both cases. Mesh resolution increases from top to bottom. The left column corresponds to the simulations using statistical variability in strength without scale effects, and the right column corresponds to the simulations using both statistical variability in strength and scale effects. For lower and medium mesh resolutions, the influence of scale effects is negligible, but the influence of scale effects can be clearly seen in the highly refined case. The damage appears to be concentrating at the bottom-center of the specimen using scale effects. It is evident that further mesh refinement is warranted to check if this trend persists.

4.5 Experimental data on Taylor-anvil impact test

Taylor-anvil impact tests were run for two different specimen speeds (321 m/s and 393 m/s). The material was Ti6Al4V and the specimen dimensions were 4.21 cm long and 1.27 cm in diameter. The average mass of the specimen was 24.21 gm. Figures 4.15–4.16 show the damage patterns observed in the experiments. At 321 m/s, a couple of cracks at approximately 45° and two small fragments were separated from the bottom of the specimen, and at 393 m/s, all material originally separated from the remainder of the specimen, again with the failure surface angled at approximately 45°.

4.6 Numerical simulations of Taylor-anvil impact test

As this test involves large plastic deformations and damage at high rates, the constitutive model should be rate-dependent. Kayenta includes two forms of rate dependence. For softening, a scale-dependent time-to-failure option provides user control for the rate at which damage propagates. The plasticity component of Kayenta further provides a conventional Duvaut-Lions viscoplastic formulation [24] to account for rate effects at high-rate loading. Since Kayenta's Duvaut-Lions rate dependence option had not been previously tested or used in combination with softening, a verification of the implementation of rate-dependence was performed before using both features for validation.

4.6.1 Verification of rate dependence, hardening and softening in Kayenta

An uniaxial-strain single-element test was run at low and high strain rates for von-Mises plasticity to verify the effect of strain rates on the results. The following cases were used for the trend tests:

- Strain-to-failure softening with no rate dependence
- No softening with rate dependence
- Strain-to-failure softening with rate dependence
- Strain-to-failure softening with rate dependence and hardening

For the verification tests described below, the pertinent parts of the input deck are shown in Table 4.2.

4.6.1.1 Strain-to-failure softening without rate dependence

This section discusses the uniaxial-strain single-element test for von-Mises plasticity with *strain-to-failure softening* and *no rate dependence*. The element was stretched until it failed. From Fig. 4.18, it can be seen that the slope discontinuity happens at the right location when it yields, and as COHER (which is the ratio of the current strength to the initial strength) goes from 1 to zero, shown in Fig. 4.17, the element loses strength accordingly. A similarly appropriate trend can be seen for the same problem at higher strain rates in Figures 4.19 and 4.20. The plots at the two different strain rates are identical because this problem is with *strain-to-failure softening* only, and *not rate dependence*.

4.6.1.2 No softening with rate dependence

This section discusses the same test but with *rate dependence* and *no softening*. Figures 4.21 and 4.22 verify that, under very small strain rates, the effect of rate dependence is negligible. Since there is no softening, the COHER ISV will stay at unity, and the normalized stress difference stays at yield. When run at higher strain rates, Fig. 4.23 shows no change in COHER, which is correct as there is no softening, and Fig. 4.24 shows the apparent increase in yield.

4.6.1.3 Strain-to-failure softening with rate dependence

This section discusses the results of the single-element test with both *rate dependence* and *strain-to-failure softening*. At low strain rates where rate dependence is negligible, Fig.

That is, noting that the axes are nondimensionalized by the values of stress and strain at yield, the graph should exhibit a slope discontinuity exactly at the point (1,1)

This is seen by the fact that the ordinate values exceed unity. Also, the post-yield decrease in stress is an artifact of running the simulations at a constant stretch rate, which results in a nonconstant strain rate that is higher at the beginning of loading than at the end (so the model is showing an appropriate decrease in apparent strength).

4.26 is similar to Fig. 4.18 where both lose strength in unison as COHER drops, according to Fig. 4.25.

At higher strain rates and with large enough deformation for the element to get damaged, both softening and rate dependence play a significant role. Figure 4.27 shows the normalized time history of COHER at higher strain rates, where the element is completely damaged (COHER approaches zero). Figure 4.28 shows that the normalized stress difference yields above the value of 1, which indicates a higher apparent yield strength compared to the quasistatic yield strength. Also, the element loses strength according to COHER. These trends tests were performed to build confidence in the implementation of rate dependence with softening in Kayenta.

4.6.1.4 Strain-to-failure softening with rate dependence and hardening

Figures 4.29–4.30 show the single-element test results using hardening, rate dependence, and softening. The figures show COHER (ratio of damaged strength to initial strength) vs. normalized time, and normalized stress difference vs. normalized strain using hardening, rate dependence, and softening, respectively. The stress response exhibits rate dependence (*i.e.,* has an apparent normalized yield stress greater than 1), hardening (nonzero slope post-yield), and softening (reduction in strength and stiffness). Also, as COHER approaches zero, the stress-difference approaches the failed strength, as desired.

After the constitutive model was verified using the single-element tests, Taylor-anvil impact simulations were run switching on each of the features *i.e.,* softening, rate dependence, and hardening. Figure 4.31 shows the simulation results when each feature was activated. Moving from left to right shows qualitatively expected trends. In particular, at high rates, when rate dependence is activated, the specimen should predict less yielding and less damage compared to one without rate dependence. Additionally, when hardening is activated, the specimen should (and does) predict even less damage as evident in Fig. 4.31. These are trend tests only; a more realistic simulation must naturally include statistics and scale effects of failure properties.

4.6.2 Calibrating rate-dependence parameters for Kayenta

Experimental data for rate-dependence of strength of Ti6Al4V is abundantly available in the literature [55, 26, 49, 58]. For metals, the yield and flow stresses are shown to be sensitive to hydrostatic pressures [80, 81]. For Ti6Al4V, up to confining pressures of 0.3 GPa, there

was almost negligible effect of hydrostatic pressures on the material response [37, 48]. To calibrate Kayenta for rate-dependence parameters, the experimental data were taken from Ref [36], where the plastic deformation and ductile fracture investigations were performed on Ti6Al4V for a variety of loading conditions (namely: tension, compression, shear) at different strain rates. In the present build of Kayenta, rate-dependence parameters, T_1 and T_2 are used to assign a value of the characteristic time according to the following formula

$$\tau = f\left(\dot{\varepsilon}\right) = T_1 \left(\frac{1}{\dot{\varepsilon}}\right)^{T_2} \tag{4.1}$$

Taking the log of both sides, Eq. (4.1) becomes

$$\log \tau = \log T_1 - T_2 \log \dot{\varepsilon} \tag{4.2}$$

Based on the unconfined compressive strength vs. strain rate data from Ref [36], a single-element test was first run by tuning the hardening parameters to match the quasistatic stress-strain curve. Then, the simulations were run at the strain rates provided in the experiment, and the characteristic time τ was tuned for the results to match the experimental stress-strain curves. These simulations were run using $T_2 = 0$, thus providing the value of τ needed at each different strain rate. Figure 4.32 shows the plot of $\log \tau$ vs. $\log \dot{\epsilon}$, from which a linear fit then gave the values for T_1 and T_2 by fitting to Eq. (4.2).

4.6.3 Validation simulations using deterministic model

After Kayenta was parameterized for rate dependence and hardening, deterministic simulations were run at the experimental speeds (*i.e.,* 321 m/s and 393 m/s) for two different Johnson-Cook failure parameter sets published in Ref [36, 55]. The pertinent input parameters for Kayenta are provided in Tables (4.3) through (4.5). Figures 4.33–4.34 show the color plot of damage, where red is damaged and blue is intact material. At 321 m/s, the published parameter set 1 [36] was under-predicting damage, and published parameter set 2 [55] was over-predicting damage compared to the experiments. At 393 m/s, both failure parameter sets over-predicted damage. Also, the response was more ductile compared to the experiments. These simulations did not include the Johnson-Cook effect of temperature on the material strength.

At high rates, thermal effects are not negligible, and they need to be considered. An equation of state (EOS), which describes the pressure as a function of the density and temperature, characterizes the material response under such loading. Mie-Grüneisen is the most commonly used EOS, and the parameters for various metals are readily available in the literature. For Ti6Al4V, the EOS parameters were taken from Ref [83].

Figures 4.35–4.36 are the same simulations as Figs. 4.33–4.34 except run with Mie-Grüneisen EOS. When using the EOS, the damage zones are considerably reduced using both the failure parameter sets. Figure 4.37 shows the convergence study for the Taylor-anvil impact problem using a deterministic model. For all meshes, the snapshots of the deformation are taken at the same instant in time. Convergence issues persist with the damage zone echoing mesh texture and failing to converge with mesh refinement. Similar simulation shortcomings have been shown to be significantly alleviated for dynamic indentation problems by including realistic strength variability and scale effects [17], so a natural next step in systematic verification and validation is to investigate whether or not inclusion of such modeling features can likewise improve results for Taylor-anvil problems.

4.6.4 Validation simulations using variability applied to rate-dependence parameters

Failure parameters published by Ref (*c.f.,* [55]) were used in this study. Previous work [17] statistically perturbed the quasistatic strength, but similar changes did not mitigate nonconvergence of the Taylor-Anvil problem, at least not when using a strain-to-failure damage criterion. The previous work, however, was using a time-to-failure damage criterion, which also included scale effects. The current Taylor-anvil study instead used a strain-to-failure option, which lacks the intrinsic rate effect of a time-to-failure option. To explore effects of variability on rate sensitivity, this Taylor-anvil study set variability of rate dependence parameters T_1 and T_2 so that low rates would show ductile response while high rates would (in principle) exhibit more brittle behavior. The T_2 parameter controls the slope of the line in Fig. 4.32, while T_1 controls the intercept. An article has recently appeared in the literature [50] that uses microphysical arguments and dimensional analysis to identify a universal curve for rate dependence of strength for a wide range of brittle nonmetallic solids. For metals, a different article [20] also reports typical statistical variability of rate effects that is similar to observations for nonmetallics. To investigate if the universal curve from Ref [50] also applies to rate-dependence data for Ti6Al4V, an analysis was performed to best fit the data on the curve defined by

$$\frac{\sigma_f}{\sigma_0} = 1 + \left(\frac{\dot{\varepsilon}}{\dot{\varepsilon_0}}\right)^{\frac{2}{3}} \tag{4.3}$$

where σ_0 and $\dot{\varepsilon_0}$ are the characteristic stress and strain rates defined in terms of the material and the microstructural properties, both treated as fitting parameters. From the compression strain rate test data [36], a method of least squares was used to fit the model in Eq. (4.3). Figure 4.38 shows the least squares fit of the experimental data to the model

with the characteristic stress and strain rates for the Ti6Al4V material, where the best-fit parameters for Ti6Al4V were found to be $\sigma_0 = 1495$MPa and $\dot{\varepsilon_0} = 6.004 \times 10^4 s^{-1}$.

This section explores the effect of statistically variable rate effects in the Duvaut-Lions component of the Kayenta model. Aside from material parameters, Taylor-impact simulations are known to be sensitive to the properties of the specimen-anvil contact surface. In the literature, choices for the friction coefficient (μ) are not always justified. Simulations presented in this section use the common choice, $\mu = 0.1$ (*c.f.,* [90, 69]), but only because research on contact theories falls outside the scope of this study.

Figure 4.39 shows the comparison of damage with and without variability for the specimen speed of 393 m/s. No EOS was used in these simulations. A Weibull modulus (m) of 1 (meaning very high variability) was applied on T_1. Figure 4.40 shows the same simulations as Fig. 4.39, except that a Mie-Grüneisen EOS was also used. Snapshots are taken at the same instant in time for all simulations. The results using variability show an appropriate and realistic break in symmetry, while the deterministic simulations exhibit typical mesh texture bias. The level of damage and ductility observed when using a statistically variable T_1 was not significantly different from the results in the deterministic simulations. In other words, despite this high level of variability in the T_1 parameter, for the specimen speed of 393 m/s, noticeably brittle response was still not observed in the simulations.

A similar study was performed for the specimen speed of 321 m/s. With no EOS, the results were again similar to the results in the deterministic simulation (see Fig. 4.41). With the inclusion of an EOS, Fig. 4.42 shows the damage propagating at approximately 45° which is a desired trait prior to fragmentation. However, at this speed, the numerical simulations did not predict fragments as observed in the experiment. Next, statistics were put on T_2, and simulations with an EOS were run for a low Weibull modulus of 10 (moderately high variability in T_2), a higher Weibull modulus of 20 (medium variability in T_2), and a very high Weibull modulus of 30 (low variability in T_2).

Figure 4.43 shows the snapshot of the simulations for different levels of variability in T_2 (with no variability or scale effects in any other parameter). As expected, when the variability decreases, the results approach the deterministic model results. For a Duvaut-Lions model, a nonzero value of T_1 provides a rate sensitive material response. A nonzero value of T_2 (which is the exponent on strain rate) provides even greater rate sensitivity as the strain rate is increased. Since Taylor impact is a very high-rate test, and since we are seeking ductile behavior at low rates, but brittle behavior at high rates, this observation suggests that the T_2 parameter may play a significant role. A similar sensitivity study was

performed on the simulations without an EOS for both specimen speeds to narrow down the best set of parameters that predict results closer to the experiments.

Figure 4.44 shows the results of the sensitivity study for the specimen speed of 321 m/s. For a higher Weibull modulus, the specimen was exhibiting localized damage, and for lower Weibull modulus, the bottom of the specimen was completely damaged. Also, the amount of ductility was decreased with the increase in variability.

The simulations presented so far used cylinder object that had stair-stepped descriptions of the angled boundaries. To investigate the associated errors, the simulations were re-run using a smooth cylinder object, where the particles are conformed with the boundary using the CPDI integrator. Figure 4.45 shows the same simulation as Fig. 4.44, except run with a Weibull modulus (m) of 12. For the damage plot, red is damaged material, and blue is intact material. For the equivalent plastic strain plot, red is maximum equivalent plastic strain (value of 0.5), and blue is zero plastic strain.

Figure 4.46 shows the same results as Fig. 4.45, except run with particles that are conformed with the boundary. The effect of smooth cylinder object on the damage patterns was negligible because all these simulations were run with considerable mesh refinement.

Particle deletion has become a common approach to accommodate fragmentation in numerical simulations [69, 101], but its lack of a physical basis is why Kayenta's ability to induce loss of strength without particle deletion is preferred. The particle deletion technique was nevertheless explored in our framework to establish a basis of comparison against what is done in the literature [69, 101].

Figure 4.47 shows the damage plot with the specimen speed of 393 m/s and no particle deletion (*i.e.,* material separation is a pure constitutive response). Row A corresponds to simulation run with Weibull modulus (m) 30 and with the Mie-Grüneisen EOS. The top views of the specimen indicate several damaged zones oriented at 45°, which is desired (although these angled damage zones are not as large in size as evident in the experimental data). Rather than hiding the fully damaged particles in postprocessing, the damaged material is shown in light gray. Row A of Fig. 4.48 is the same as row B of Fig. 4.47. For comparison, row B of Fig. 4.48 corresponds to the same simulation as row A and at the same instant in time, except particle deletion was activated when the Kayenta's COHER value reached 0.005. It is evident that particle deletion gives different answers compared to that without particle deletion, yet this technique is adopted in the literature to validate constitutive models. The comparison study in Fig. 4.48 demonstrates that particle deletion is nonphysical and hence inappropriate for model validation.

To check if more localized damage zones and fragmentation can be predicted in the numerical simulations, variability was simultaneously put on the melt temperature and the Johnson-Cook failure parameter D_5 (parameter associated with thermal softening). Figure 4.49 shows the comparison study of damage for the best prediction achieved so far in the numerical study. The effect of putting variability simultaneously on the melt temperature and the Johnson-Cook failure parameter D_5 had almost negligible effect on the damage patterns.

4.6.5 Locking in Taylor-anvil impact test

Like conventional finite-element methods, the material point method can potentially exhibit anomalous (*i.e.,* nonphysical) kinematic locking because of the use of linear shape functions on a rectangular grid. The nonphysical checker-boarding of the vertical component of stress seen in row A of Fig. 4.50 is because of the locking issue. This locking is alleviated by implementing standard antilocking algorithms [59]. Row B corresponds to the same simulation as row A except run with one of these algorithms, called pressure stabilization. Though the checker-boarding is alleviated, the effect of pressure stabilization on the damage patterns is negligible.

4.7 Conclusions

For the unnotched Charpy test, the energy absorbed by the specimen, the bend angle of the specimen, and the damage patterns using Kayenta's various failure options that include aleatory uncertainty and scale effects were compared against the experiments. Initially, the simulations were run at *10 times the experimental striker speeds* to make the simulations complete faster, and also to investigate the rate effects on the specimen damage patterns. The average bend angle was 7.7% higher than the experimental observation, and the average amount of energy absorbed was 24% higher. Not surprisingly, when the simulations were run at the same speeds as the experiments, the results gave much better agreement with the data: the average bend angle was 0.4% higher than observed in the experiment, and the average amount of energy absorbed was 1.2% lower. However, mesh refinement is required to see if the results converge. The fracture patterns did not converge using only statistical variability in strength, but results improved when using both statistical variability in strength and scale effects to give damage patterns concentrated at the bottom-center of the specimen. For the amount of energy absorbed by the specimen, statistical variability in strength and scale effects using strain-to-failure softening option did not eliminate convergence issues during the softening phase. Therefore, it is prudent to

investigate if scale-dependent time-to-failure softening option with statistical variability in strength and scale effects could mitigate the convergence issue during softening.

For the Taylor-anvil impact test, the damage patterns using aleatory uncertainty applied to rate-dependence parameters were compared against the experiments. Since rate dependence was never used simultaneously with softening in Kayenta before, a systematic verification study was presented. Mesh sensitivity using a deterministic model was demonstrated. Aleatory uncertainty was applied to the rate-dependence parameters T_1 and T_2. Though improved results were demonstrated, the results still do not adequately capture the experimental observations. At the specimen speed of 321 m/s, the simulations with statistics put on T_1 with EOS were predicting results closer to the experiments. In these simulations, though the damage was propagating at 45°, that did not induce fragments in the specimen as observed in the experiment. At higher speeds of 393 m/s, fragmentation was observed, but the fragments were not as large in size as evident in the experimental data.

In the numerical study presented for Taylor-anvil impact test, strength was taken to be pressure independent based on the available experimental data (up to confining pressures of 0.3 GPa). However, the actual impact pressures reached in the numerical simulations fall well outside the experimental range. Therefore, it is recommended to run the simulations with pressure-dependent strength to explore the sensitivity of damage patterns to this feature.

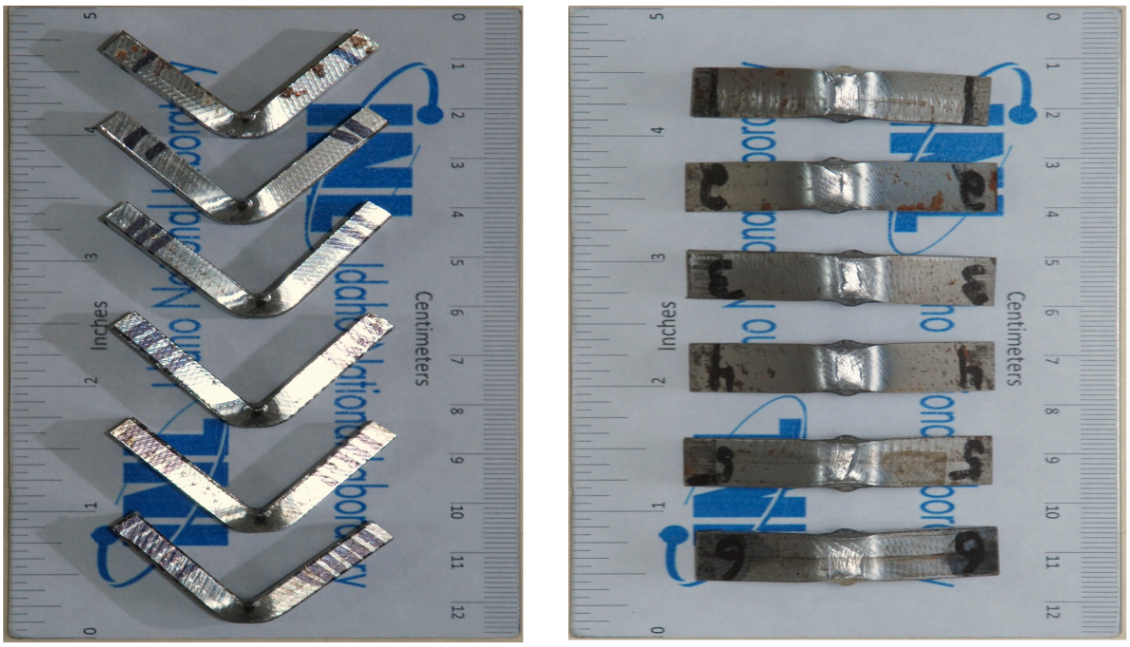

Figure 4.1: Experimental observations of damage patterns provided by INL. Used with permission from INL (INL/MIS-14-31639)

Date	Sample ID	Length	Width	Thickness	Orientation	Absorbed Energy	Bend Angle
#1	RHA	2.011	.392	.197	N/A	99.3	92
#2	RHA	2.163	.392	.197	N/A	110.7	95
#3	RHA	2.166	.391	.196	N/A	107.9	97
#4	RHA	2.170	.394	.197	N/A	112.0	98
#5	RHA	2.155	.393	.197	N/A	108.3	96
#6	RHA	2.044	.392	.197	N/A	102.8	92

Figure 4.2: Experimental observations provided by INL. Lengths are in inches, energy is in ft-lbs, and the bend angle is in degrees. Used with permission from INL (INL/MIS-14-31639)

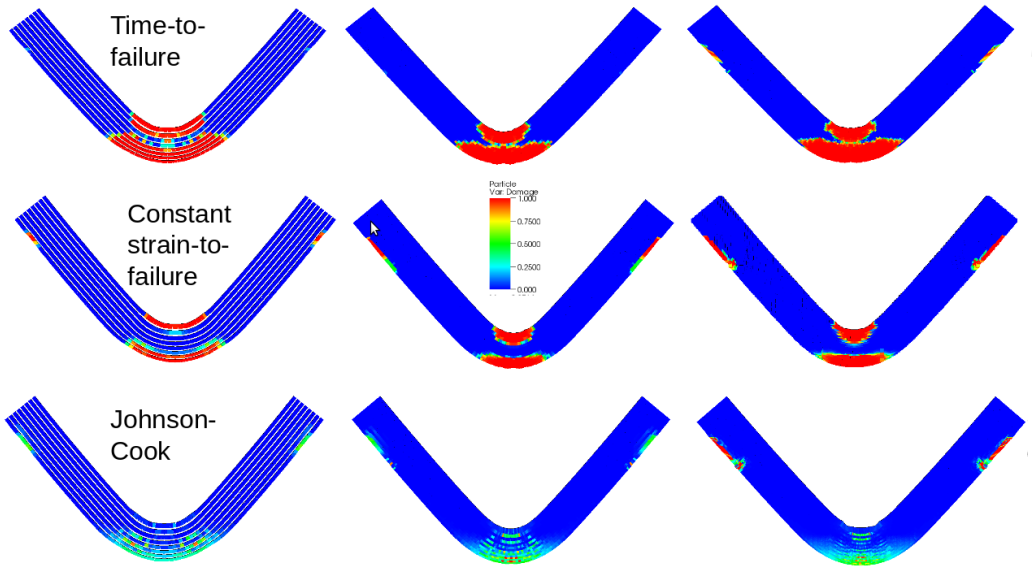

Figure 4.3: Convergence study using 2D plane-strain simulations. Mesh resolution increases from left to right. Color plot of damage. Red indicates damaged and blue indicates intact material

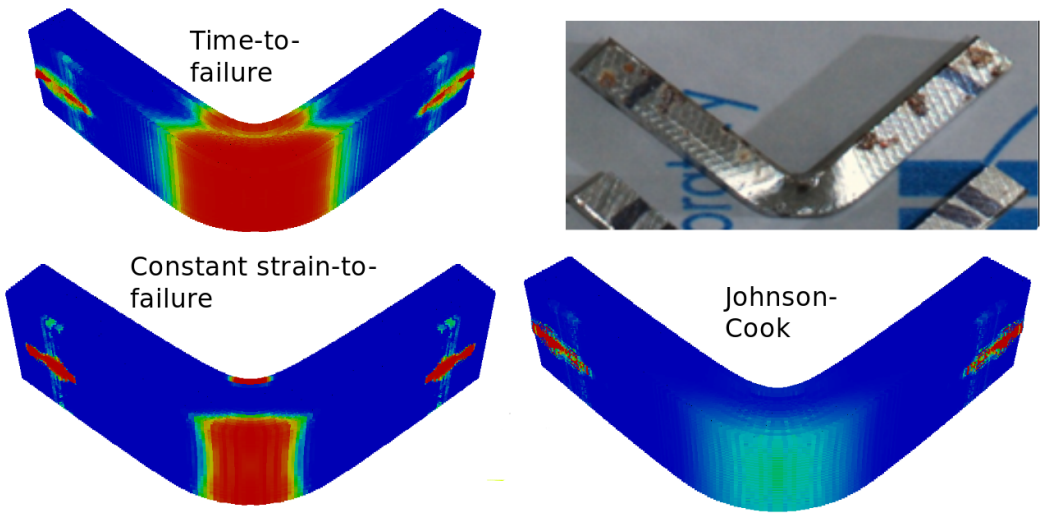

Figure 4.4: 3D simulations using different softening options. Color plot of damage. Red indicates damaged and blue indicates intact material

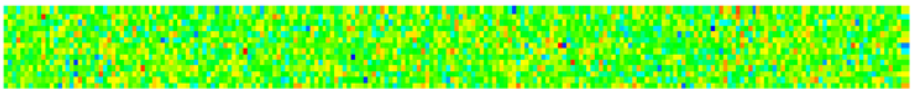

Figure 4.5: Variability in the strength of the specimen

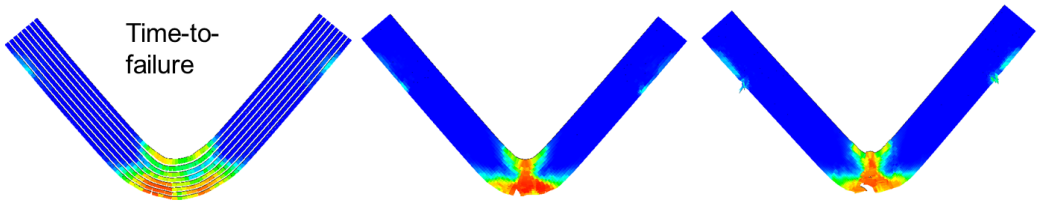

Figure 4.6: The same simulations as in Fig. 4.3 except run using Kayenta's option for statistical variability and scale effects in strength. Mesh resolution increases from left to right

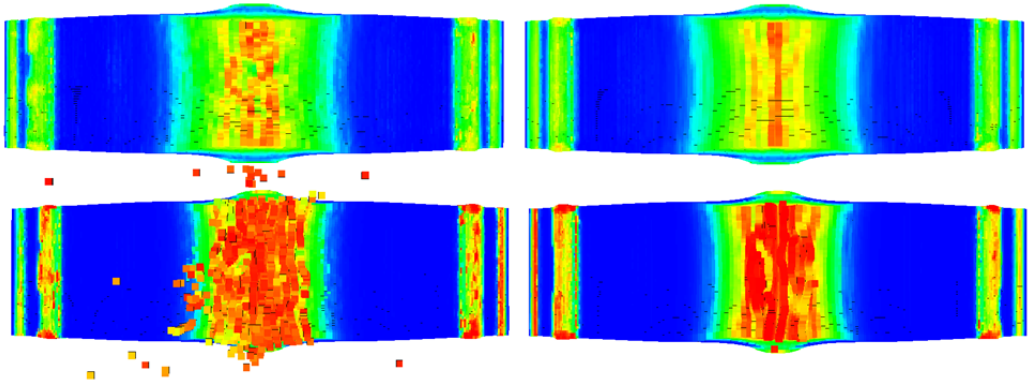

Figure 4.7: Plots of damage (red is damaged, and blue is intact material) using constant strain-to-failure softening model in Kayenta. Strain at failure is 0.3. Moving from top to bottom corresponds to tripling the fracture speed (FSPEED parameter in Kayenta controls the rate of loss in strength in the material after softening starts to occur), and moving from left to right corresponds to tripling the Weibull modulus

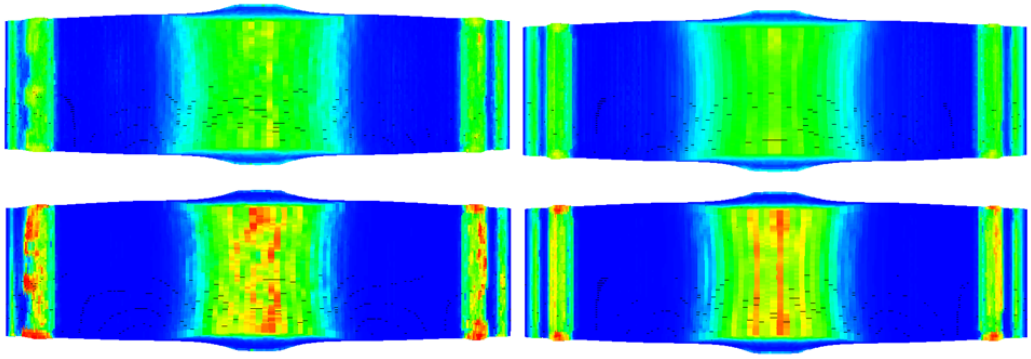

Figure 4.8: Plots of damage (red is damaged, and blue is intact material) using constant strain-to-failure softening model in Kayenta. Strain at failure is 0.4. Moving from top to bottom corresponds to tripling the fracture speed (FSPEED parameter in Kayenta controls the rate of loss in strength in the material after softening starts to occur), and moving from left to right corresponds to tripling the Weibull modulus

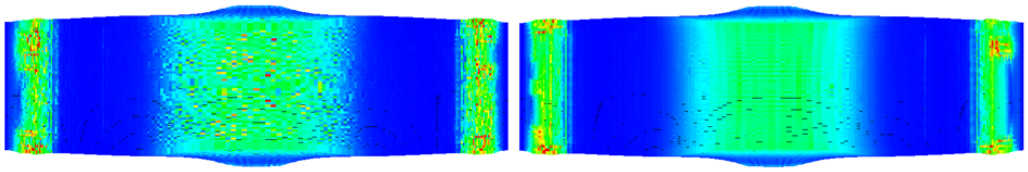

Figure 4.9: Plots of damage (red is damaged material, and blue is intact material) using Johnson-Cook softening model in Kayenta. Moving from left to right corresponds to tripling the Weibull modulus

Bend Angle (Degrees)	$K.E_{initial}$-$K.E_{final}$(Striker) (Joules)
103.1	176

Bend Angle (Degrees)	$K.E_{initial}$-$K.E_{final}$(Striker) (Joules)
101.4	181

Bend Angle (Degrees)	$K.E_{initial}$-$K.E_{final}$(Striker) (Joules)
101.7	181

Bend Angle (Degrees)	$K.E_{initial}$-$K.E_{final}$(Striker) (Joules)
101.3	183

Figure 4.10: Plots of damage (red is damaged material, and blue is intact material) using constant strain-to-failure softening with an artificially increased striker speed of 51.47 m/s. Moving from left to right corresponds to tripling the Weibull modulus (*i.e.*, making the material more deterministic in its response), and moving from top to bottom corresponds to increasing failure strain from 0.3 to 0.4

Bend Angle (Degrees)	$K.E_{initial}$-$K.E_{final}$(Striker) (Joules)
95.5	143.2

Bend Angle (Degrees)	$K.E_{initial}$-$K.E_{final}$(Striker) (Joules)
95.4	140.7

Bend Angle (Degrees)	$K.E_{initial}$-$K.E_{final}$(Striker) (Joules)
95.3	144.2

Bend Angle (Degrees)	$K.E_{initial}$-$K.E_{final}$(Striker) (Joules)
95.6	144.4

Figure 4.11: Plots of damage (red is damaged material, and blue is intact material) using constant strain-to-failure softening model with striker speed of 5.147 m/s. Moving from left to right corresponds to tripling the Weibull modulus, and moving from top to bottom corresponds to increasing failure strain from 0.3 to 0.4

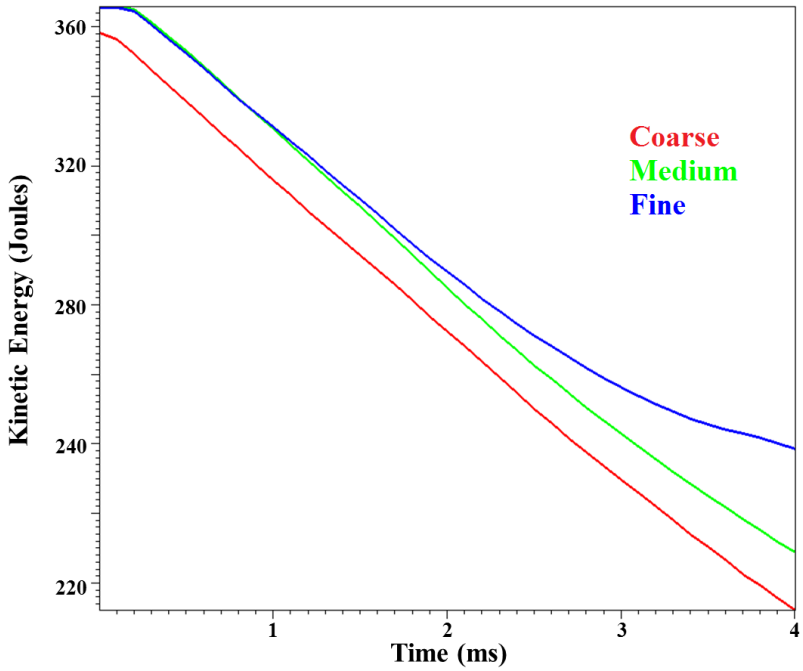

Figure 4.12: Time history of the K.E. of the striker for three meshes using statistical variability in strength with *no scale effects*

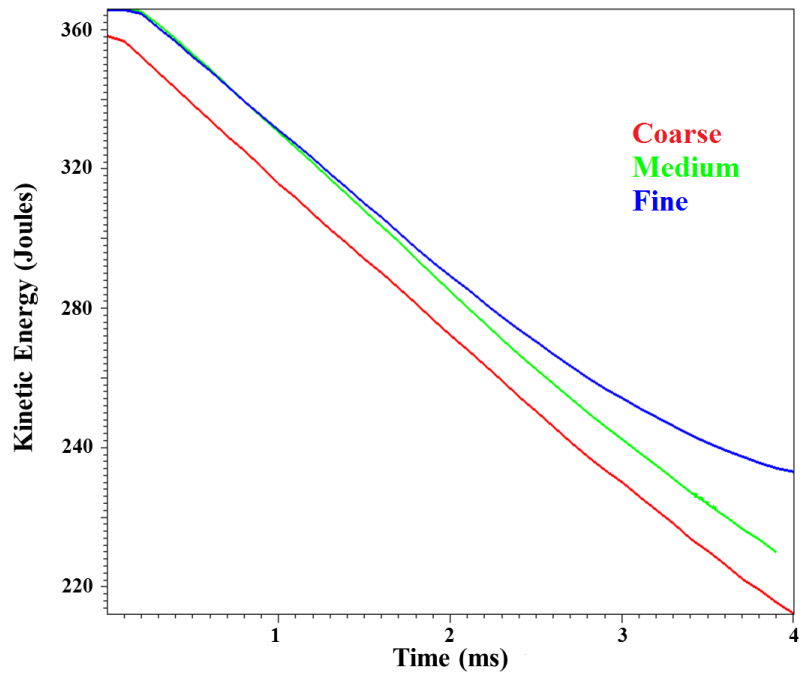

Figure 4.13: Time history of the K.E. of the striker for three meshes using statistical variability in strength and scale effects

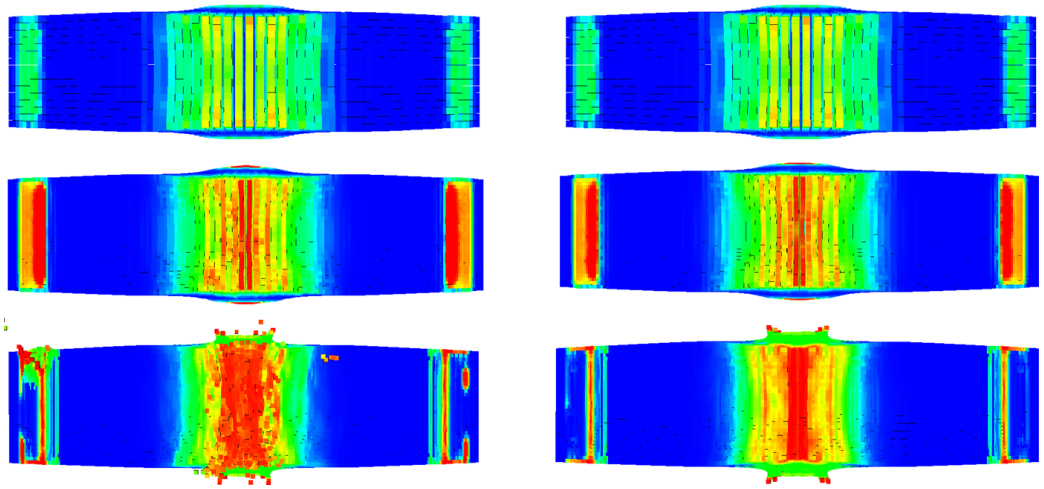

Figure 4.14: Color plots of damage. Blue is intact material and red is completely damaged material. Mesh resolution increases from top to bottom. The left column corresponds to the simulations using statistical variability in strength without scale effects and the right column corresponds to the simulations using both statistical variability in strength and scale effects

Figure 4.15: Experimental observations of damage patterns at specimen speed of 321 m/s. Used with permission from INL (INL/MIS-14-31639)

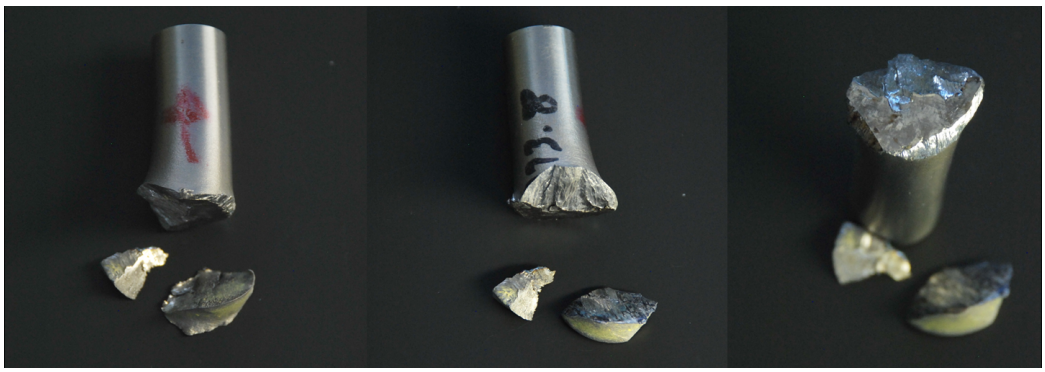

Figure 4.16: Experimental observations of damage patterns at specimen speed of 393 m/s. Used with permission from INL (INL/MIS-14-31639)

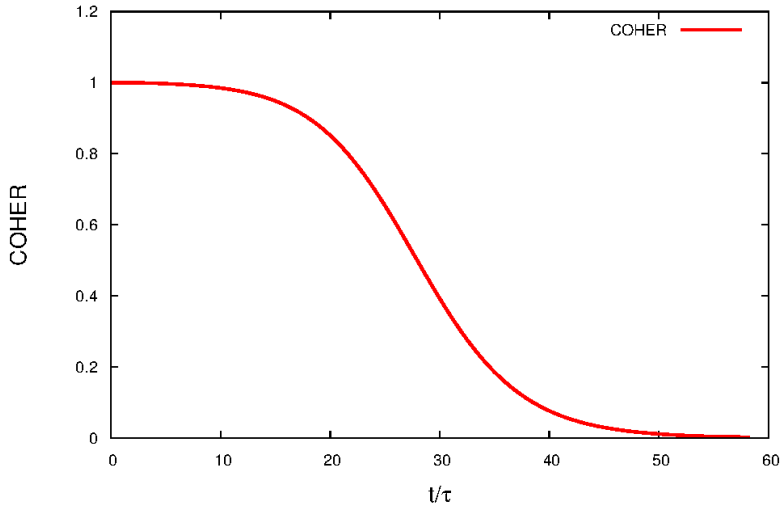

Figure 4.17: Normalized time history of the COHER at low strain rates (softening only)

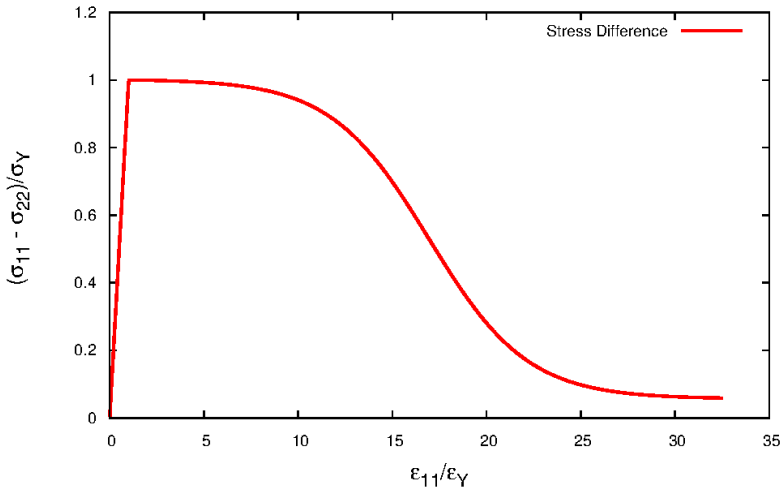

Figure 4.18: Normalized stress difference vs. normalized strain at low strain rates (softening only)

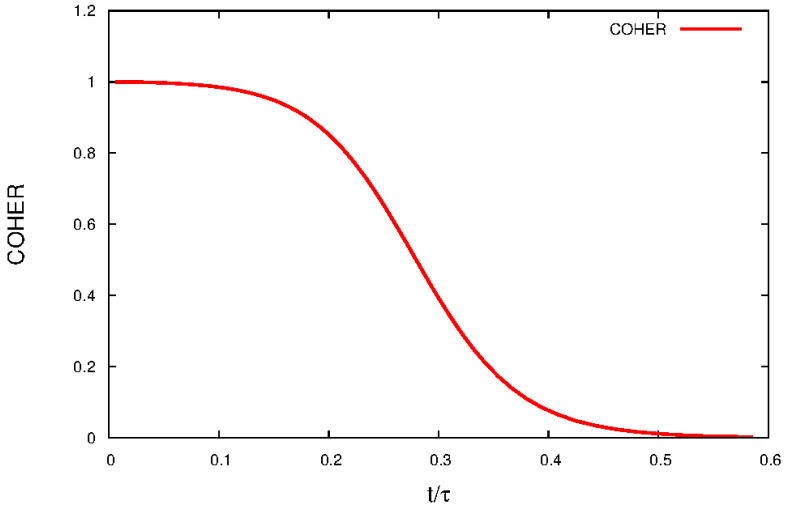

Figure 4.19: Normalized time history of the COHER at high strain rates (softening only)

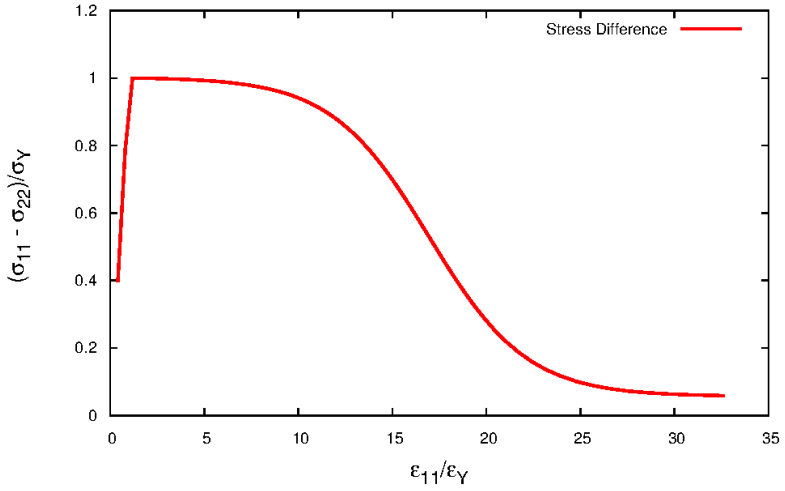

Figure 4.20: Normalized stress difference vs. normalized strain at high strain rates (softening only)

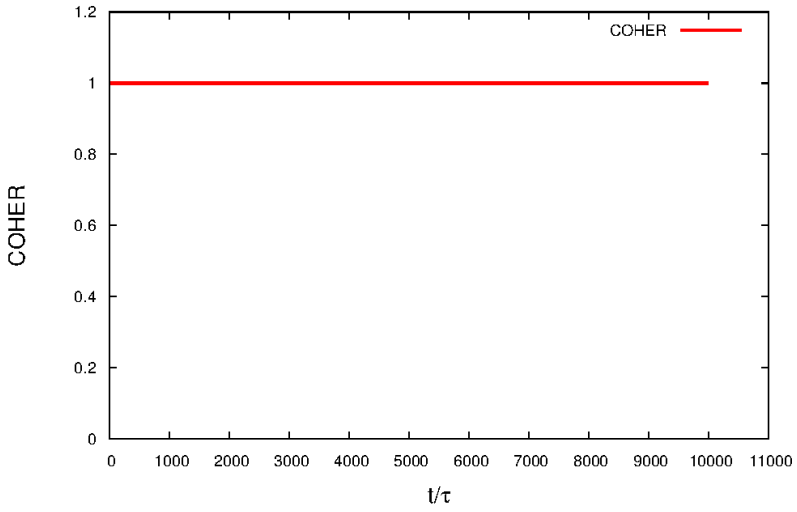

Figure 4.21: Normalized time history of the COHER at low strain rates (rate dependence only)

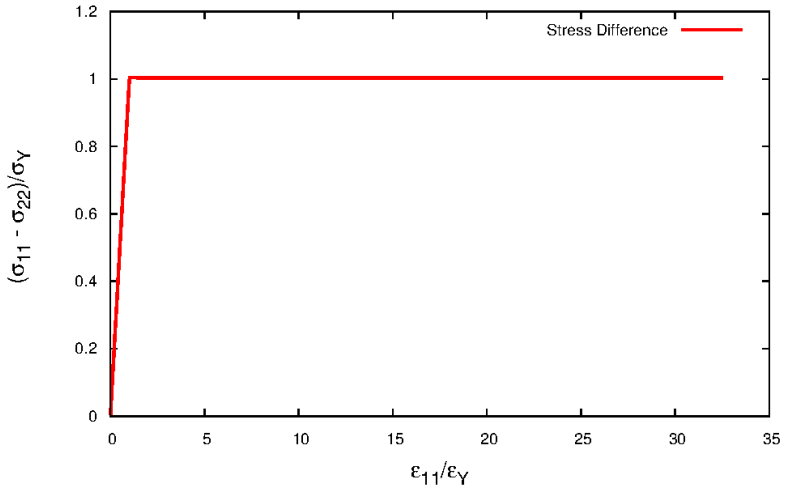

Figure 4.22: Normalized stress difference vs. normalized strain at low strain rates (rate dependence only)

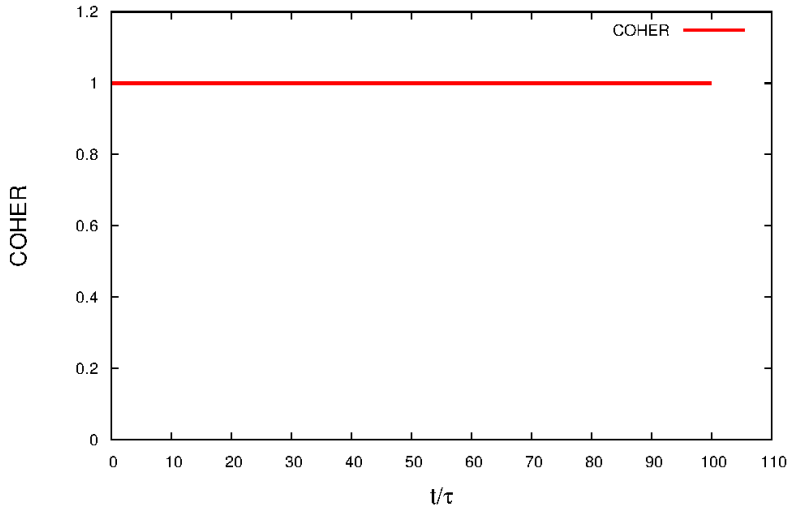

Figure 4.23: Normalized time history of the COHER at high strain rates (rate dependence only)

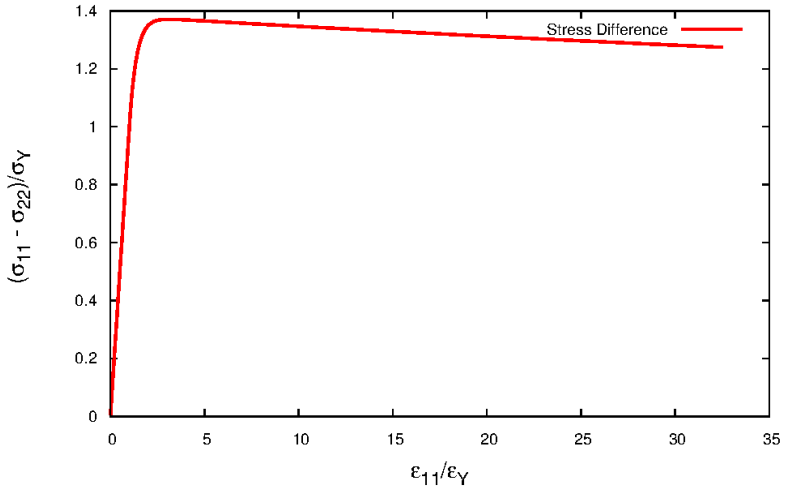

Figure 4.24: Normalized stress difference vs. normalized strain at high strain rates (rate dependence only)

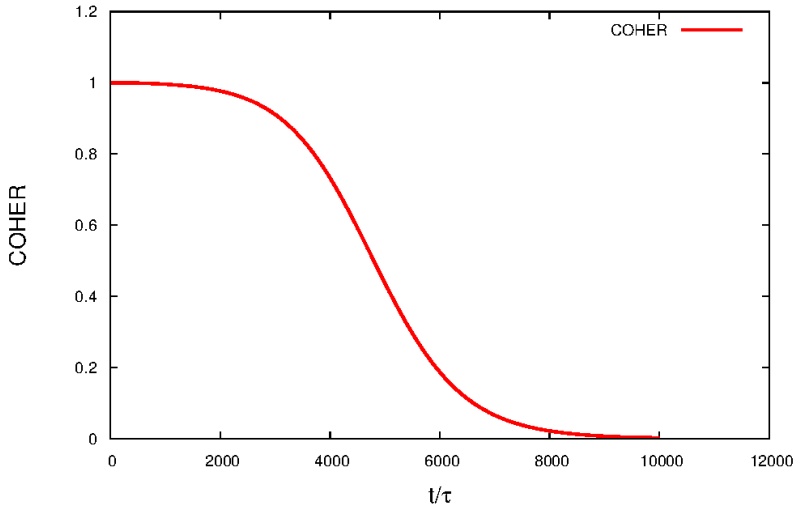

Figure 4.25: Normalized time history of the COHER at low strain rates (both rate dependence and strain-to-failure softening)

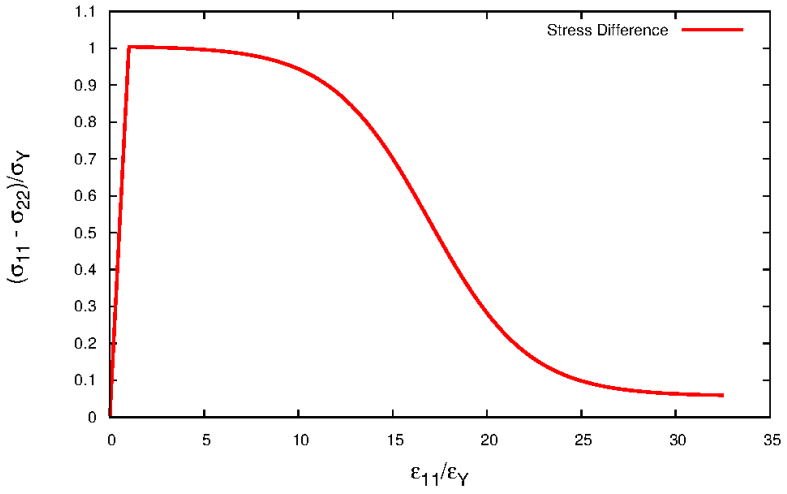

Figure 4.26: Normalized stress difference vs. normalized strain at low strain rates (both rate dependence and strain-to-failure softening)

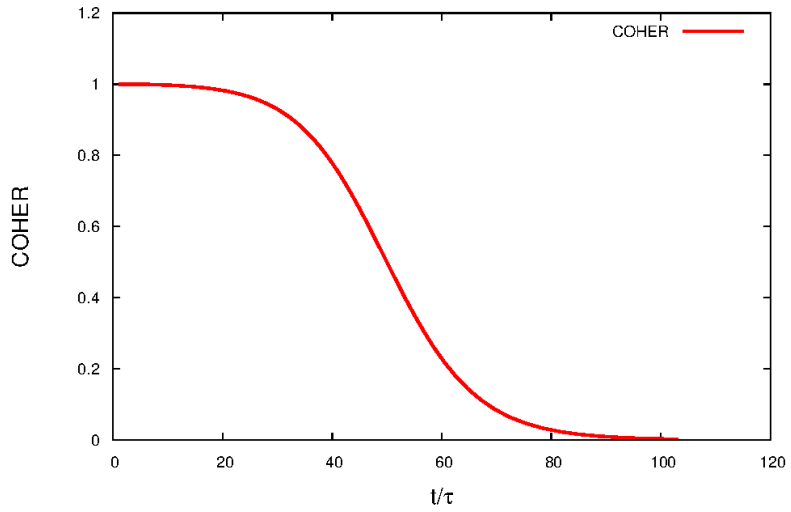

Figure 4.27: Normalized time history of the COHER at high strain rates (both rate dependence and strain-to-failure softening)

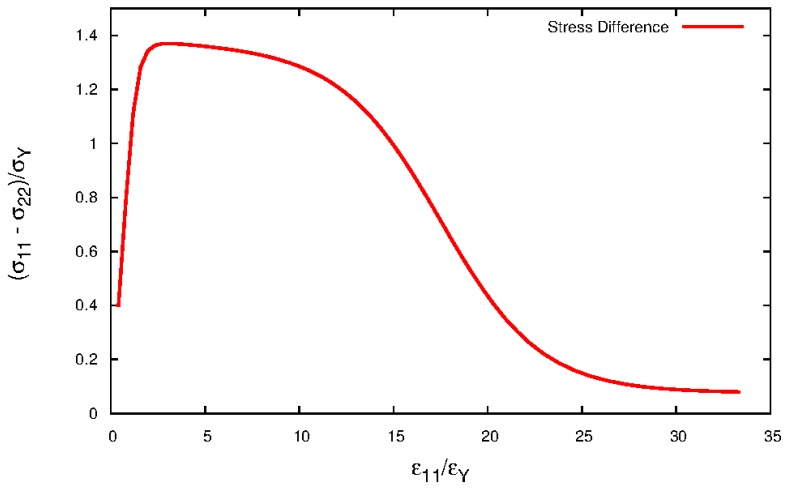

Figure 4.28: Normalized stress difference vs. normalized strain at high strain rates (both rate dependence and strain-to-failure softening)

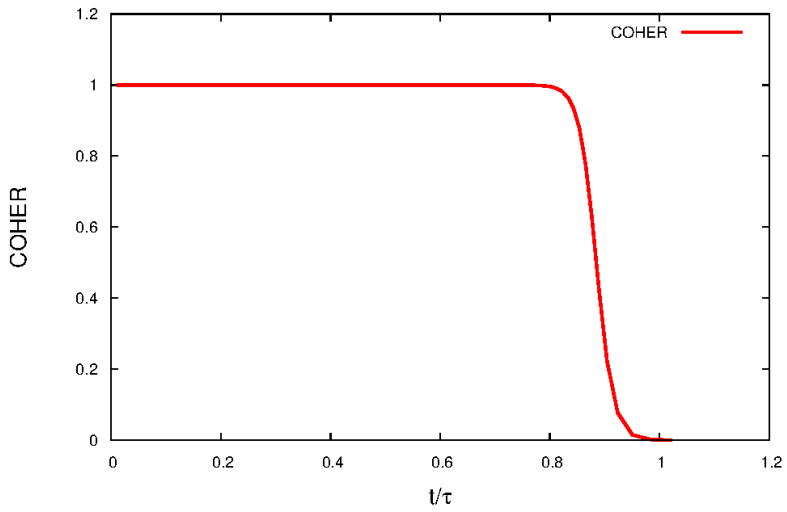

Figure 4.29: Normalized time history of the COHER at high strain rates (rate dependence, hardening and softening)

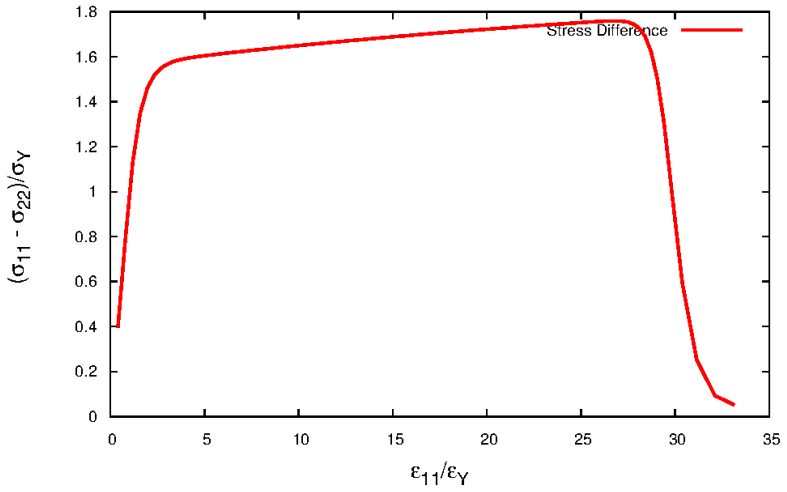

Figure 4.30: Normalized stress difference vs. normalized strain at high strain rates (rate dependence, hardening and softening)

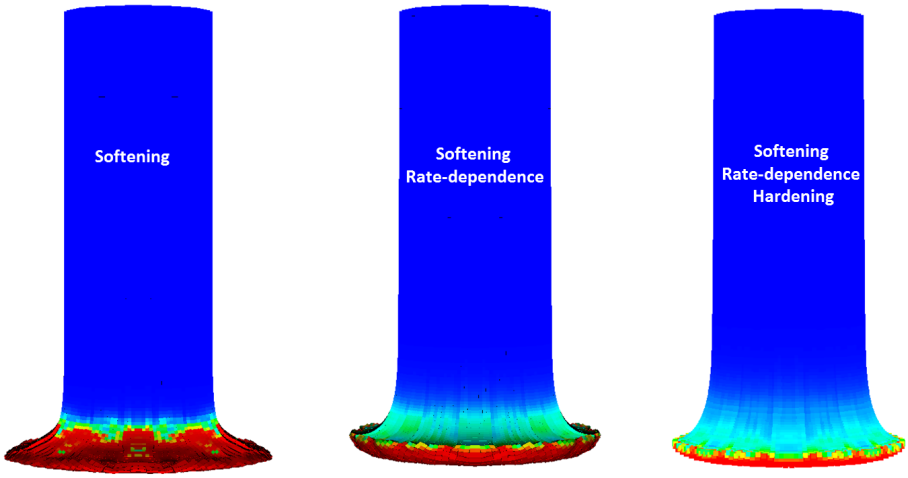

Figure 4.31: Trend tests on Taylor-anvil impact simulations using deterministic material properties (*i.e.*, no statistical variability or scale effects). Blue is intact material and red is damaged material

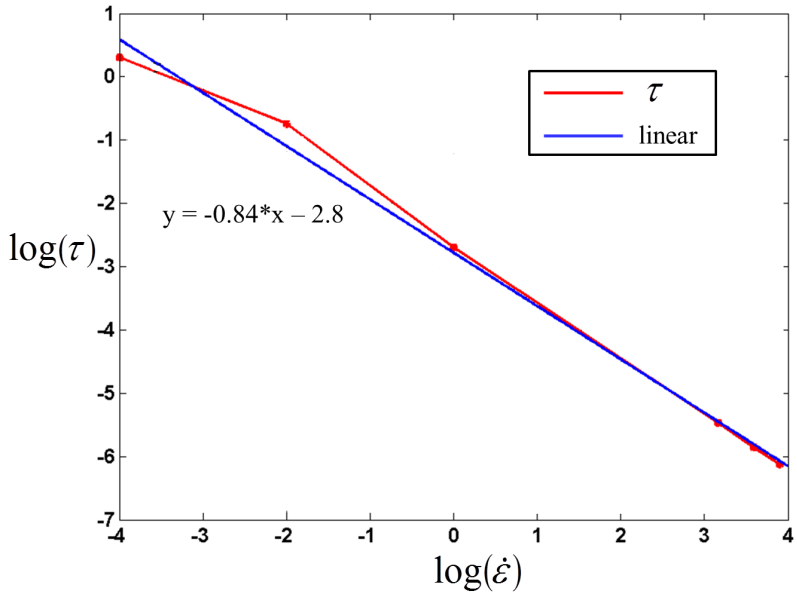

Figure 4.32: τ as a function of strain rate

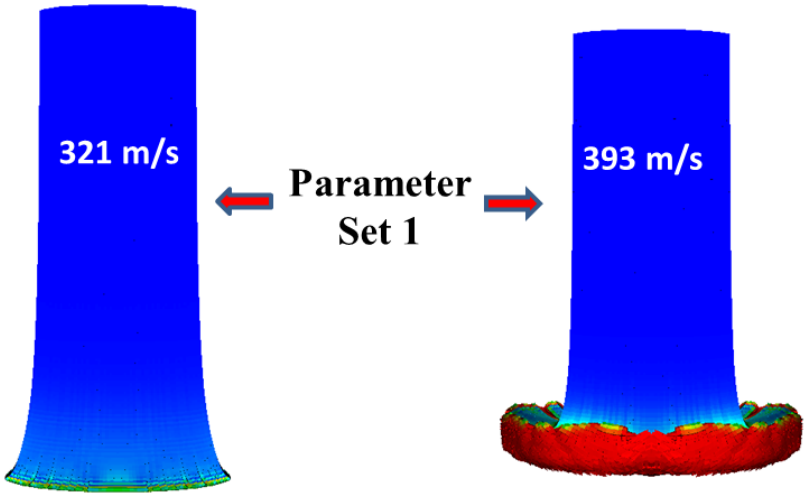

Figure 4.33: Plot of damage using Johnson-Cook failure model without thermal effects. Parameter set published by Ref [36]

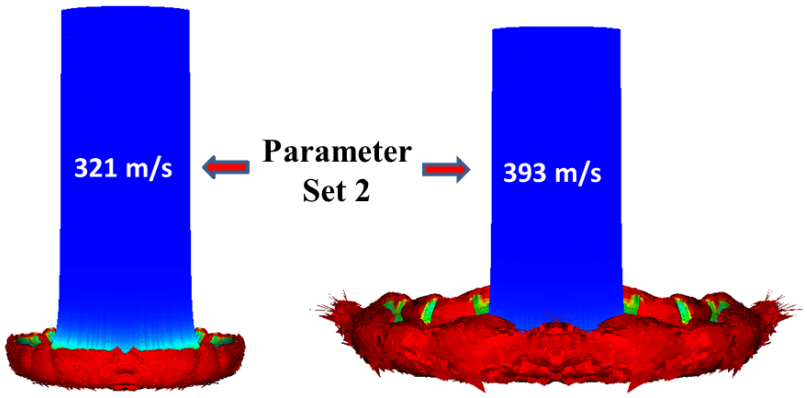

Figure 4.34: Plot of damage using Johnson-Cook failure model without thermal effects. Parameter set published by Ref (*c.f.,* [55])

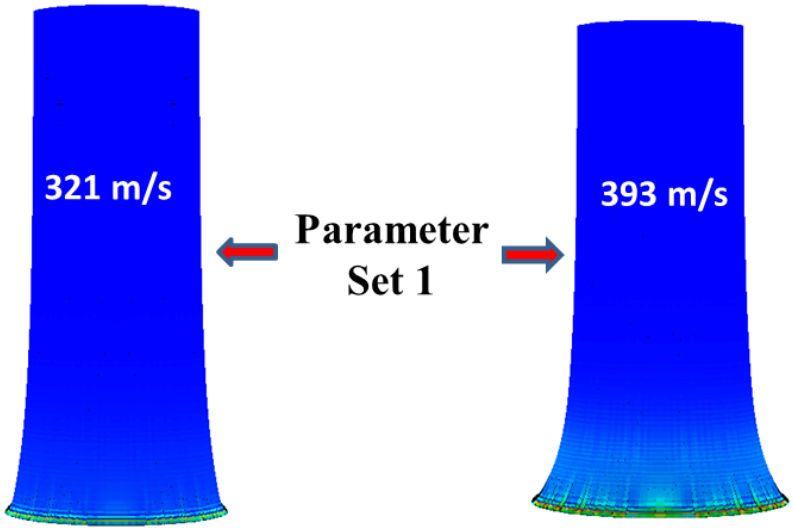

Figure 4.35: Plot of damage using Johnson-Cook failure model with thermal effects. Parameter set published by Ref [36]

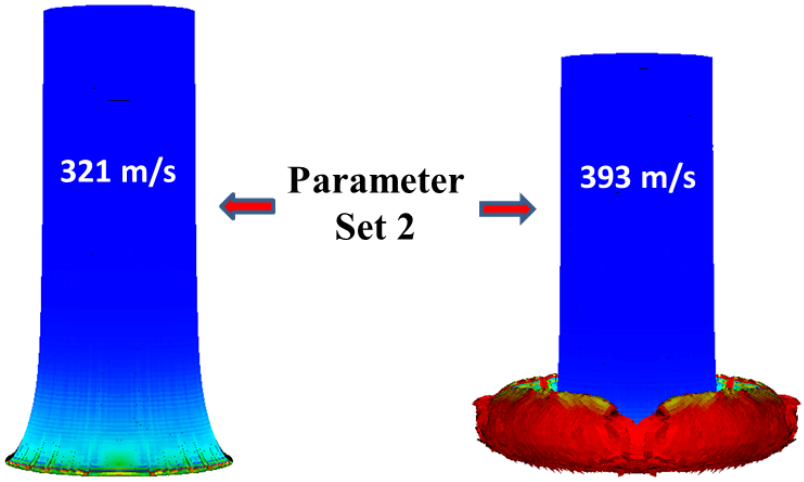

Figure 4.36: Plot of damage using Johnson-Cook failure model with thermal effects. Parameter set published by Ref [55]

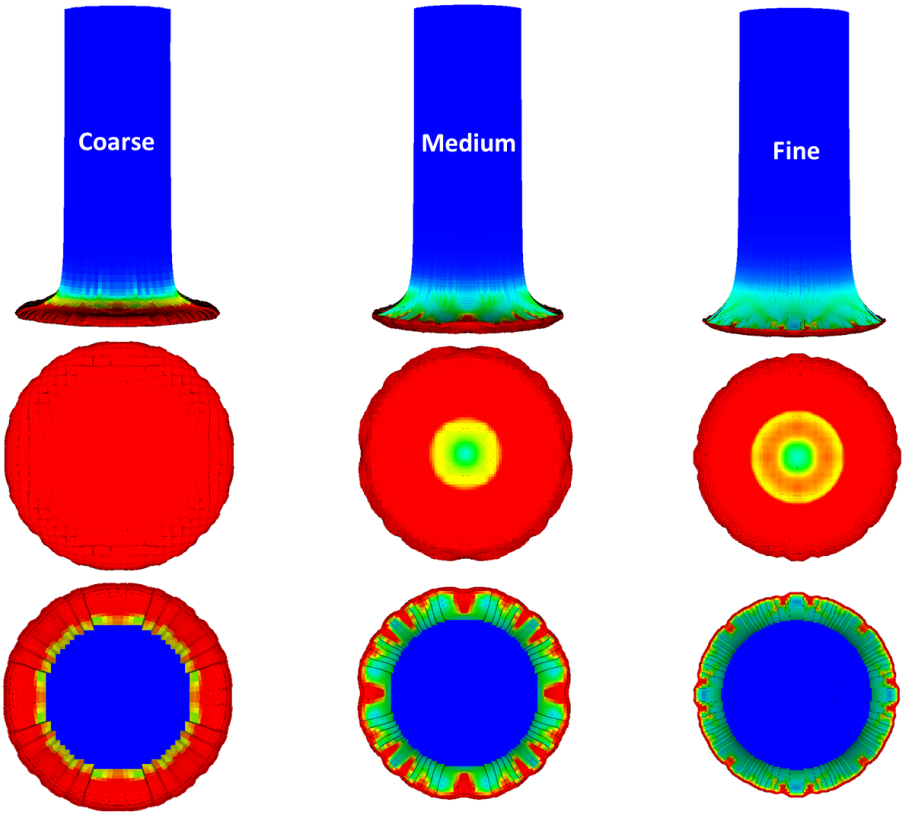

Figure 4.37: Severe mesh dependency for damage using a deterministic scale-insensitive model. Mesh resolution increases from left to right. Red is damaged and blue is intact material. Each column indicates the front view, the bottom view, and the top view of the damaged specimen, respectively

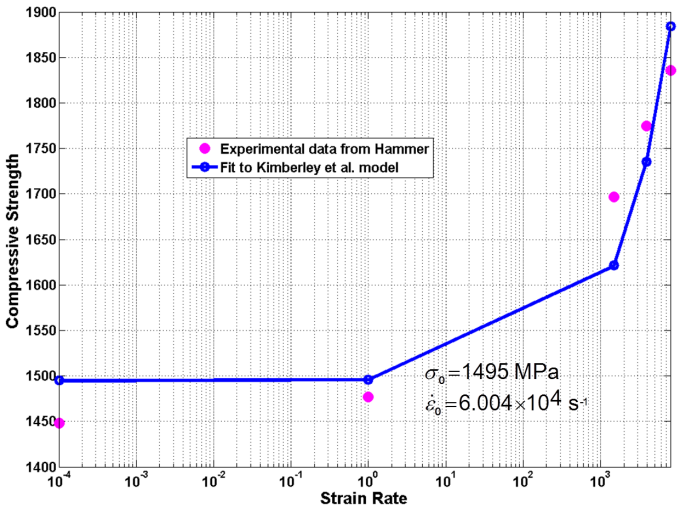

Figure 4.38: Least squares fit of Ti6Al4V experimental data [36] to Eq. (4.3)

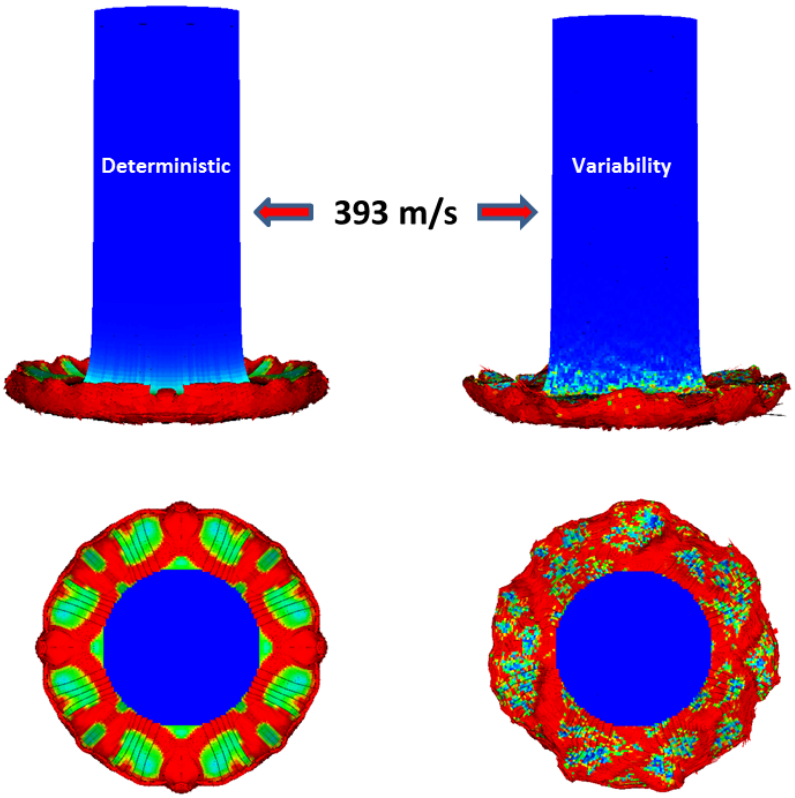

Figure 4.39: Sensitivity of rate-dependence parameter T_1 on damage without EOS. The top row corresponds to the front view of the specimen and the bottom row corresponds to the top view of the specimen. Specimen speed is 393 m/s and Weibull modulus (m) is 1. Red is damaged material, and blue is intact material

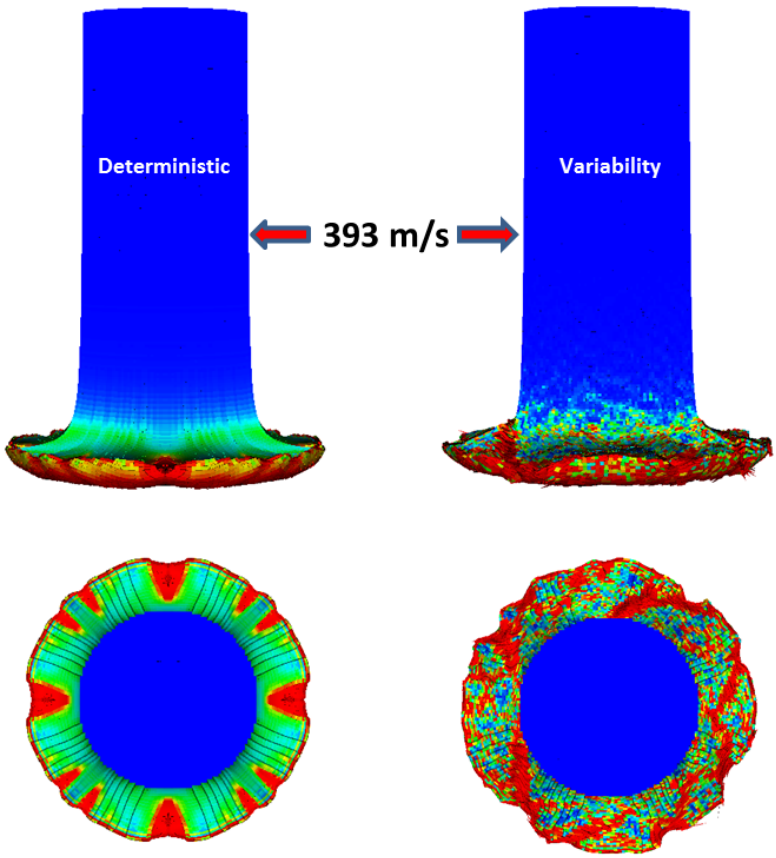

Figure 4.40: Sensitivity of rate-dependence parameter T_1 on damage with EOS. The top row corresponds to the front view of the specimen and the bottom row corresponds to the top view of the specimen. Specimen speed is 393 m/s and Weibull modulus (m) is 1. Red is damaged material, and blue is intact material

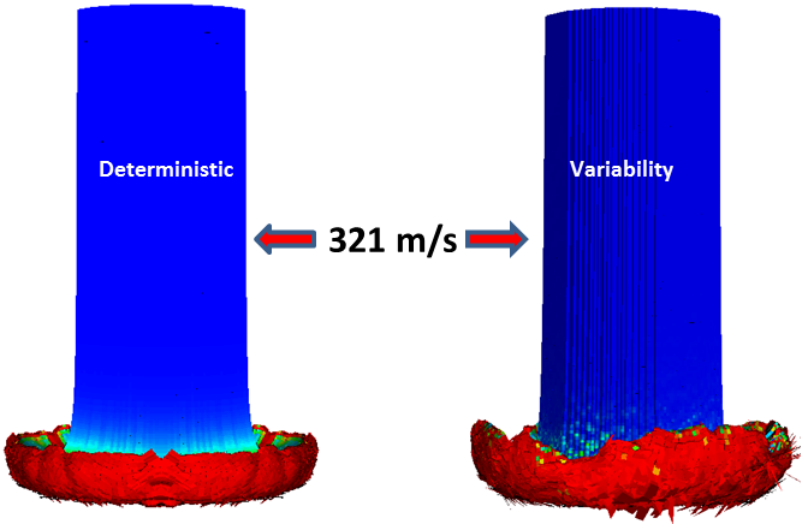

Figure 4.41: Sensitivity of rate-dependence parameter T_1 on damage without EOS. Specimen speed is 321 m/s and Weibull modulus (m) is 1. Red is damaged material, and blue is intact material

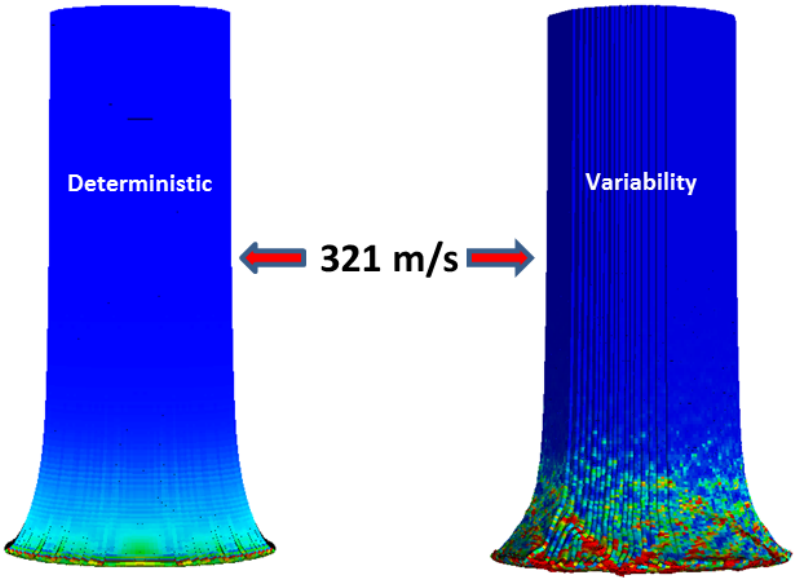

Figure 4.42: Sensitivity of rate-dependence parameter T_1 on damage with EOS. Specimen speed is 321 m/s and Weibull modulus (m) is 1. Red is damaged material, and blue is intact material

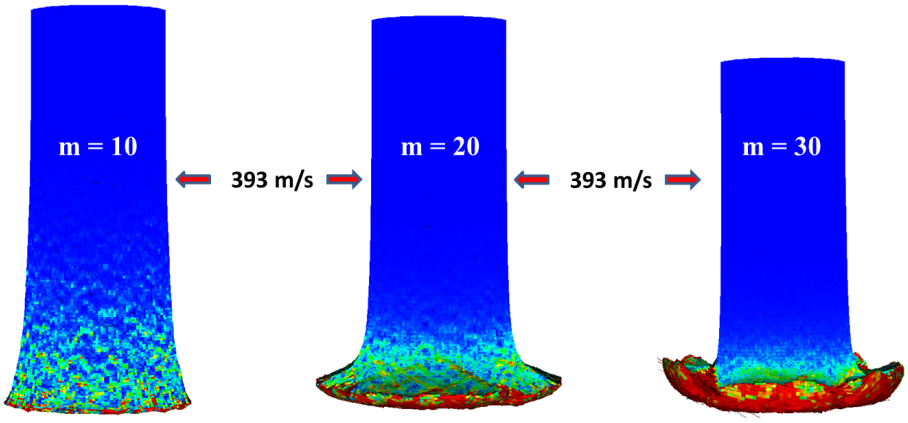

Figure 4.43: Color plot of damage with statistics put on T_2. Blue is intact material and red is completely damaged material. The specimen impact speed was 393 m/s. The Weibull modulus (m) increases from left to right *i.e.,* variability decreases from left to right

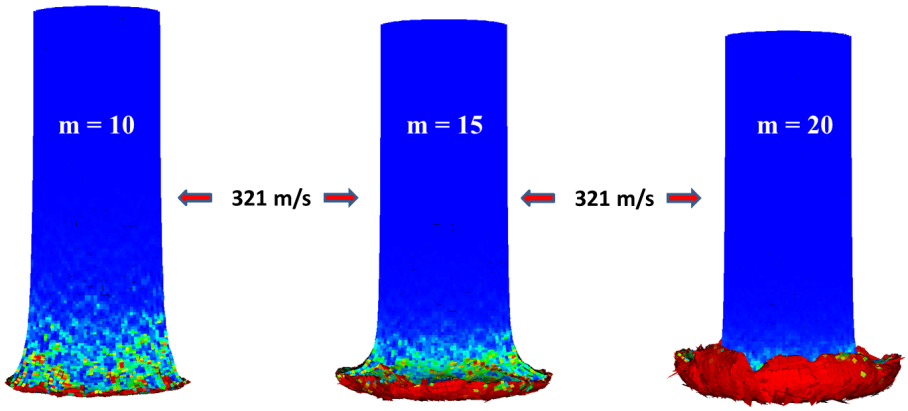

Figure 4.44: Color plot of damage with statistics put on T_2. Blue is intact material and red is completely damaged material. Weibull modulus (m) increases from left to right *i.e.,* variability decreases from left to right

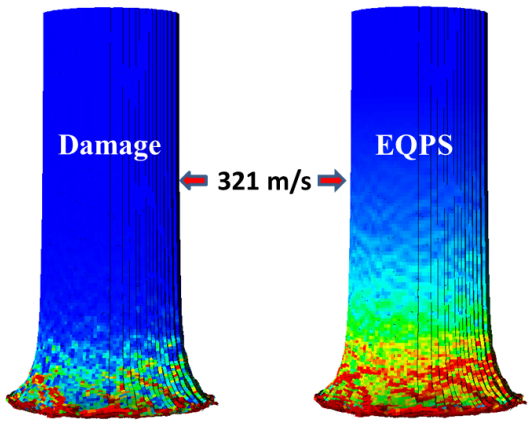

Figure 4.45: Color plot of damage and equivalent plastic strain with statistics put on T_2. Weibull modulus (m) is 12

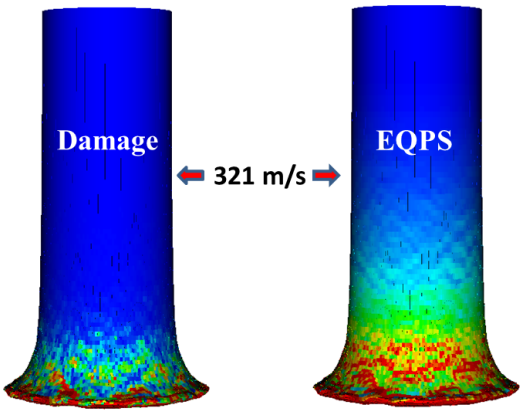

Figure 4.46: Same simulation as Fig. 4.45 except run with particles conforming with the boundary

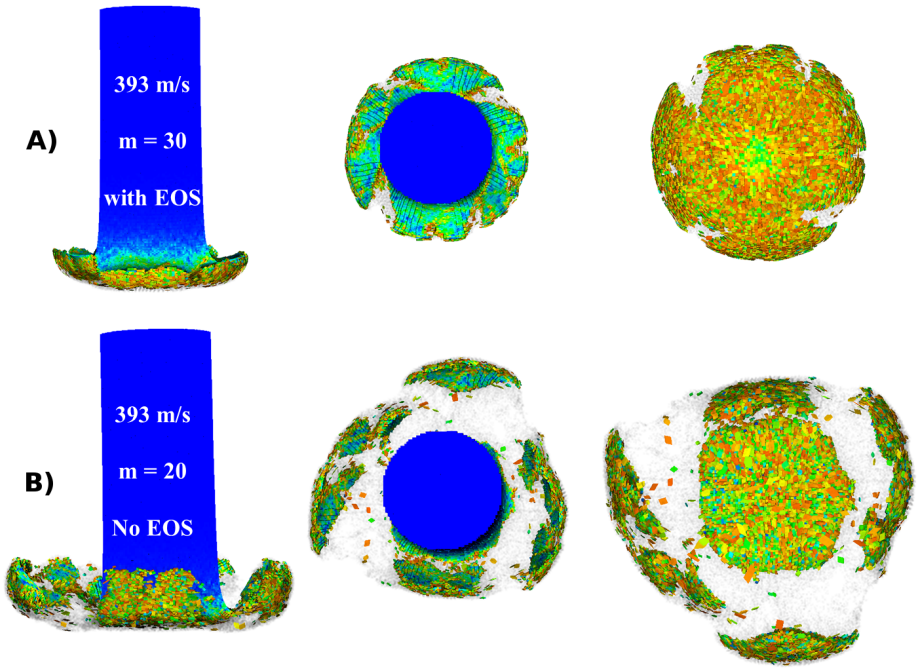

Figure 4.47: Results without particle deletion. A) Simulation with the Mie-Grüneisen EOS. Each row represents the front view, the top view, and the bottom view of the damaged specimen, respectively. Damaged material is shown in gray. B) corresponds to the same simulation as row A, except run without an EOS, and the Weibull modulus (m) is 20 to encourage discrete fragmentation. Impact speed is 393 m/s.

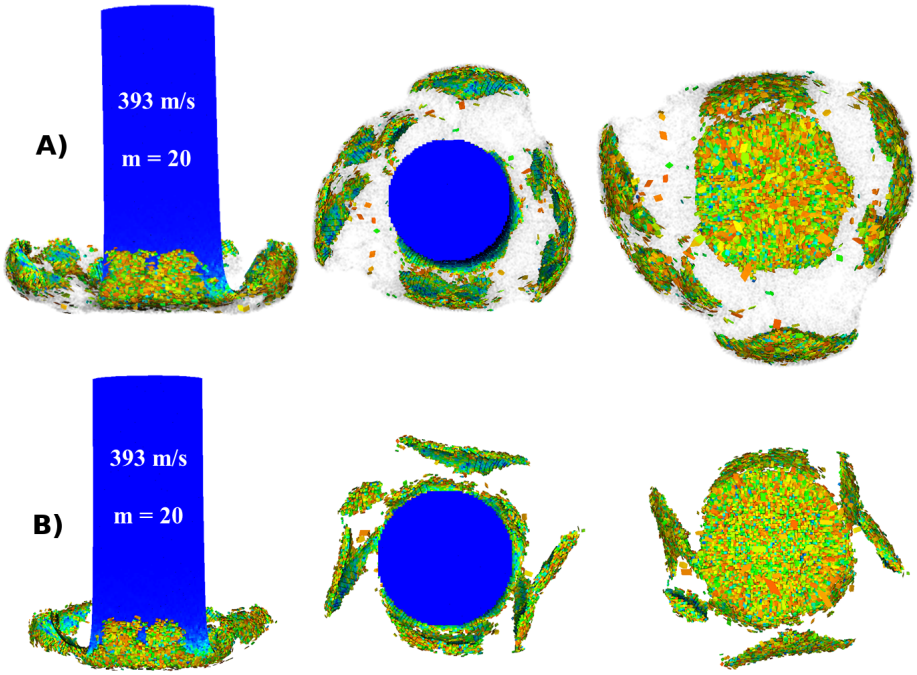

Figure 4.48: Effect of particle deletion technique on the damage patterns. A) Simulation without the Mie-Grüneisen EOS. Each row represents the front view, the top view, and the bottom view of the damaged specimen, respectively, which used constitutive softening *without* particle deletion. B) Same simulation as row A except run *with* particle deletion

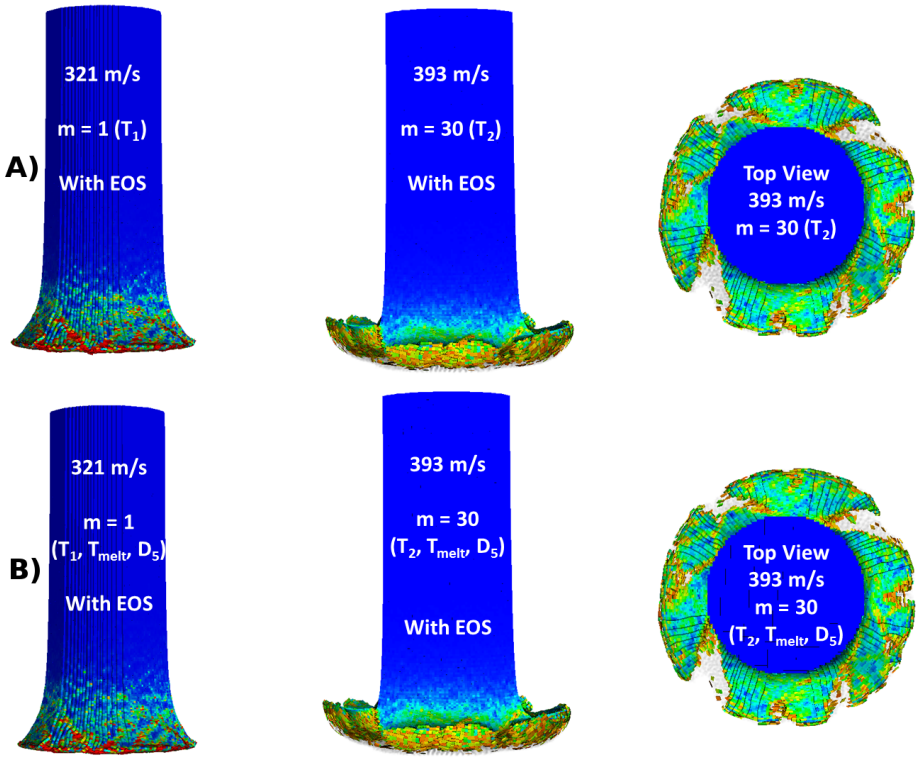

Figure 4.49: Effect of variability on melt temperature and Johnson-Cook failure parameter D_5 on the damage patterns. A) Simulations with variability put on just rate-dependence parameters. B) Same simulation as row A, except variability was also put on the melt temperature and the Johnson-Cook failure parameter D_5

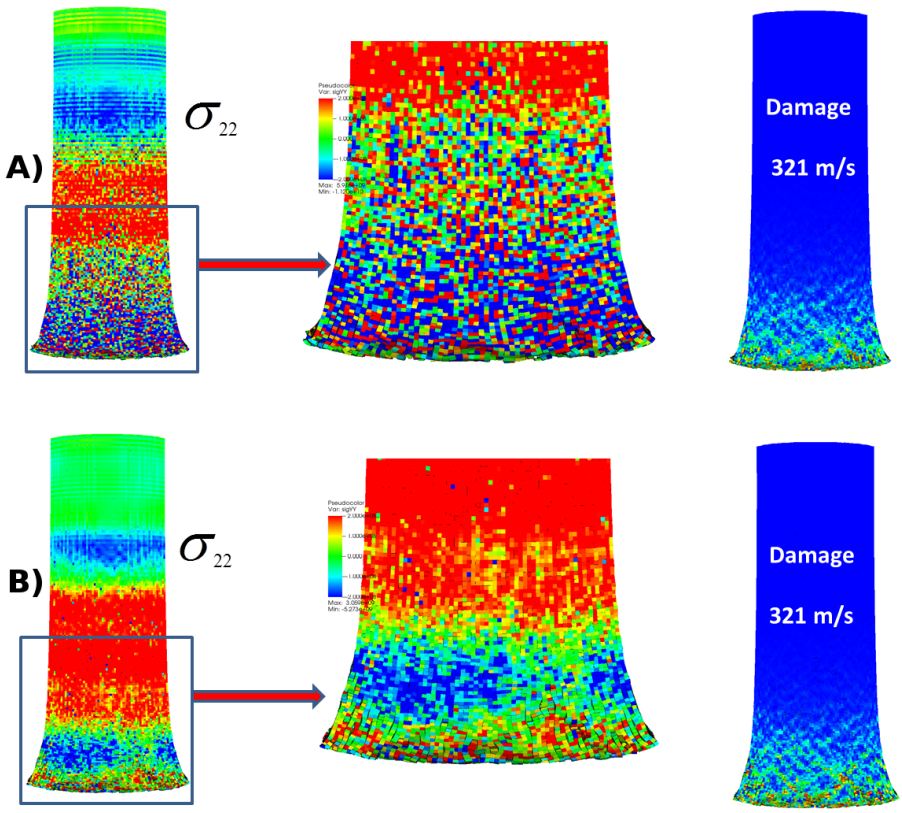

Figure 4.50: Effect of pressure stabilization on the damage patterns. A) Simulation without pressure stabilization technique. Color plot of σ_{22} where the checker-boarding is the symptom of locking. B) Same simulation as row A, except run with pressure stabilization

Table 4.1: Mesh configurations and the amount of energy absorbed using statistical variability in strength with *no scale effects*.

Mesh	Cell spacing $[x, y, z]$ (cm)	Initial K.E. (Joules)	Final K.E. (Joules)	ASTM Energy absorbed by the specimen (Joules)
Mesh1	0.125, 0.125, 0.125	358	192	166
Mesh2	0.0625, 0.0625, 0.0625	365	208	157
Mesh3	0.03125, 0.0625, 0.0625	365	238	127

Table 4.2: Input data used for single-element verification tests.

Yield stress in shear	Rate dependence	Softening (Johnson-Cook Failure model)	Hardening
$A_1 = 570$ MPa	$T_1 = 1 \times 10^{-6}$s, $T_2 = 0$	D_1 = -0.81, $D_2 = 1.18$, D_3 = -0.15, D_4 = -0.012, D_5 = 2.10	HC = 1 GPa, RN = -0.25 GPa

Table 4.3: Input data used for Taylor-impact tests.

Material Properties	Rate dependence	Hardening
ρ=4430 kg/m^3, G = 44 GPa, K = 91.7 GPa	$T_1 = 16 \times 10^{-4}$ s, $T_2 = 0.84$	HC = 1 GPa, RN = -0.25 GPa

Table 4.4: Johnson-Cook failure model parameter sets.

Johnson-Cook Failure model	D_1	D_2	D_3	D_4	D_5
Hammer (Parameter set 1)	-0.81	1.18	-0.15	-0.012	2.10
Johnson (Parameter set 2)	-0.09	0.25	-0.5	-0.014	3.87

Table 4.5: Mie-Grüneisen EOS inputs.

SNDSP0 (Initial sound speed) m/s	CV (Specific heat) J/kg.C	γ (Grüneisen parameter)	S_1
5130	570	1.23	1.28

CHAPTER 5

DATA RELOCALIZATION TO ACCELERATE CONVERGENCE FOR FAILURE INITIATION IN COMPUTATIONAL DAMAGE MECHANICS

5.1 Abstract

Nonlocal theories are often regarded as necessary to achieve mesh-insensitive predictions of ceramic damage, while purely numerical sources of abnormally slow convergence have been largely ignored. An alternative stress field regularization technique compensates for under-resolution of the stress field by preserving the probability of failure initiation regardless of whether the domain is discretized into few or many elements. This method, called data relocalization, effectively replaces the uniform stress state assigned to a low-order finite element with the m-norm of the actual (spatially varying) stress field, where m is the Weibull modulus. As an example, a ceramic Brazilian indirect tension test (for which the prefailure stress field is known) is shown to exhibit intolerably slow convergence when run with only scale-dependent and statistically variable strength. Nearly convergent solutions are then achieved even on a very coarse mesh using data relocalization, thus proving a purely numerical (nonphysical) source of mesh sensitivity.

5.2 Introduction

Achieving mesh independent results in damage simulations has been a persistent unsolved challenge to model developers. Lab data show a compelling size effect for strength, in which large specimens are weaker on average [29, 47]. When analyzing lab data for strength, the experimentalists need to report the specimen size that goes with that strength, which

K. Kamojjala and R. Brannon. Data relocalization to mitigate slow convergence caused by under-resolved stress fields in computational damage mechanics *J. Eur. Ceram. Soc.*, 2014. Reprinted with permission from Elsevier.

is a nontrivial requirement if the stress field is not constant over the specimen. Ref [40] proposed an "effective volume" [22] approach given as a stress-weighted m-norm average of the volume, where m is the Weibull modulus. Specifically, the effective volume is given by

$$V_{\text{eff}} = \int_V \left(\frac{\sigma}{\sigma_{\text{peak}}} \right)^m \mathrm{d}V, \tag{5.1}$$

where σ is a stress invariant (*e.g.,* maximum principal stress), and σ_{peak} is the maximum value of σ in the domain V. This approach, called *data delocalization* [11, 10], appropriately gives high stress regions higher weight.

Conventional plasticity theories fail to capture this size effect because there is no length scale associated with the constitutive model. An alternative route to capture these size effects is to use gradient plasticity theory [64] or nonlocal theory [25, 27], but their formulations currently are based on overly simplistic constitutive models. Previous work [17] using statistical variability of strength and scale effects has considerably reduced mesh sensitivity in dynamic sphere indentation problems. The same features provided much more realistic qualitative statistical variability of strength and scale effects [54], but failed to exhibit similar benefits with respect to convergence. Achieving convergence on failure initiation is a necessary pre-requisite to predicting mesh-insensitive failure progression.

This chapter addresses a numerical technique (which from here on is termed as "data relocalization") to achieve the first requirement *i.e.,* convergence on failure initiation. Sec. 5.3 reviews the theory that an m-norm of the actual (spatially varying) stress field needs to be applied to the element to preserve probability of failure initiation of a finite subdomain of the body regardless of whether the domain is discretized into few or many elements. A 1D exploratory problem is designed to test this technique. Sec. 5.4 solves a 1D problem using the method of manufactured solutions in a finite-element code. With conventional methods, significant mesh dependency is demonstrated for the onset of failure using low-order shape functions, with only slight improvement using higher-order shape functions. Data relocalization, on the other hand, provides a substantial improvement of convergence. Sec. 5.5 illustrates this technique on a more complicated Brazilian test problem.

5.3 Data relocalization

Based on classical Weibull theory [95] for a uniform stress field σ within a specimen of volume V (considered as a single-element mesh), the probability that the sample is safe from failure initiation is

$$P^{\text{safe}} = 2^{-\left(\frac{V}{\bar{V}}\right)\left(\frac{\sigma}{\bar{\boldsymbol{\sigma}}}\right)^m}, \tag{5.2}$$

where $\bar{\boldsymbol{\sigma}}$ is the median strength associated with a reference volume $\bar{V}$, and m is the Weibull modulus. For piecewise constant stresses, σ_1 and σ_2, applied to volumes V_1 and V_2 (considered as a 2-element mesh) covering the same total volume V, the whole volume is taken to be safe if each individual volume is safe. This assertion implicitly neglects spatial correlation of strength, which is appropriate if the volumes V_1 and V_2 are large in comparison to imperfections such as microcracks that give rise to failure. Accordingly, the probability that the whole volume V is safe is

$$P^{\text{safe}} = 2^{-\left(\frac{V_1}{\bar{V}}\right)\left(\frac{\sigma_1}{\bar{\boldsymbol{\sigma}}}\right)^m} 2^{-\left(\frac{V_2}{\bar{V}}\right)\left(\frac{\sigma_2}{\bar{\boldsymbol{\sigma}}}\right)^m}. \tag{5.3}$$

The goal is to preserve probability of failure initiation. Setting Eqs. (5.2) and (5.3) equal and solving for σ , we have

$$\sigma^m = \frac{V_1{\sigma_1}^m + V_2{\sigma_2}^m}{V}, \tag{5.4}$$

which implies

$$\sigma = \left(\frac{V_1{\sigma_1}^m + V_2{\sigma_2}^m}{V}\right)^{\frac{1}{m}}. \tag{5.5}$$

Extending the concept to continuous fields,

$$\sigma_{\text{eff}} = \left(\frac{\int\limits_V \sigma^m \, \mathrm{d}V}{V}\right)^{\frac{1}{m}}. \tag{5.6}$$

This is the effective uniform stress that would need to be applied to a specimen of volume V to produce the same probability of failure as the actual nonuniform stress field on V. This is an important observation because low-order shape functions effectively treat stress as constant over each element. If the actual nonuniform stress field is known, we will demonstrate that Eq. (5.6) gives an artificially intensified uniform stress that preserves the failure probability. Rather than changing the stress itself (which would inappropriately change elastic strain), we use Eq. (5.6) to artificially reduce the element strength based on our assumed knowledge of the exact nonuniform stress field over the element domain. We call this approach *data relocalization* because it accounts for the stress concentrations that cannot be resolved on the grid, essentially reversing the data delocalization in Eq. (5.1). Of course, an exact prefailure stress field is not known in practice, so this work is merely serving as a demonstration that under-resolved stress fields caused by low-order shape functions clearly contribute to mesh sensitivity of failure.

To explore the consequences of a piecewise-constant stress representation, a problem was designed having a large stress gradient. The new method to compensate for under-resolved stress fields was tested using an exploratory problem under the assumption that we know the actual prefailure stress field over a specimen *a priori*. The following sequence of steps explain the method to draw Weibull plots from strength testing data (whether acquired though actual or virtual experiments).

1. Obtain a table of measured stresses at failure initiation: $\{\sigma_1, \sigma_2, \sigma_3, ...\sigma_n\}$.
2. Sort the failure stresses: $\sigma_1 < \sigma_2 < \sigma_3.... < \sigma_n$.
3. Set $\bar{\boldsymbol{\sigma}}$ to be the median of the data.
4. Create a table of abscissa values defined by $x_k = \log\left(\frac{\sigma_k}{\bar{\boldsymbol{\sigma}}}\right)$.
5. For the k^{th} point in a set of measured data points, set $P_k^{\text{safe}} = 1 - \frac{k-\frac{1}{2}}{n}$. This is a conventional complementary cumulative distribution estimator [38], which we have found gives the best accuracy for small data sets.
6. Create a table of ordinate values defined by $y_k = \log\log\frac{1}{P_k^{\text{safe}}} - \log\log 2$
7. Plot y_k vs. x_k, which is the Weibull plot.
8. Optional: set $\bar{V}$ equal to the effective specimen volume defined in Eq. (5.1). In practice this usually requires analytical or numerical simulation to obtain the prefailure stress field.

For the exploratory problem, we imagine generating virtual strength data by running the finite element code a total of n times, each time noting the value of stress that resulted in failure. By setting $\bar{\boldsymbol{\sigma}}$ and $\bar{V}$ equal to 1, we are defining the failure stress on the abscissa to be multiples of $\bar{\boldsymbol{\sigma}}$. The left plot in Fig. 5.1 shows five different nonlinear stress fields (green lines), and their corresponding ordinary (1-norm) average approximations (blue lines) for a two-element mesh. The plot on the right is the corresponding Weibull plot, where green lines are the analytical failure probability curves, and blue lines are the corresponding numerical failure probability curves found by assigning a standard Weibull scale-dependent distributed strength to each element. The numerically computed failure probability curves do not overlap with the analytical curves for this coarse mesh resolution. Figure 5.2 shows the same analysis, except that the m-norm approximation of the actual stress field was used to compute the numerical failure probability curves. Even though this is an extremely

coarse mesh, the m-norm allows the simulated failure probability curves to nearly overlap the analytical failure probability curves, as desired.

Figure 5.3 shows that an ordinary average requires an intractably high level of mesh refinement in order to cause the numerical failure probability curves to converge to the analytical failure probability curves. Our new m-norm relocalization method provides convergence on significantly coarser meshes. The next section describes a similar verification problem solved using a finite-element code.

5.4 Method of manufactured solutions

The method of manufactured solutions (MMS) is a rigorous verification technique used in many engineering fields [75, 72, 18, 12]. "MMS is the process of deriving the analytical body forces, tractions, and the initial conditions required to achieve a predetermined deformation field. These analytical solutions for the forcing functions are supplied as inputs to the codes, and error is then quantified by comparing the predicted and predetermined displacement and stress fields" [46]. Continuum momentum balance in 3D is

$$\operatorname{div}(\boldsymbol{\sigma}) + \rho\boldsymbol{b} = \rho\boldsymbol{a}\ , \qquad \text{or, in indicial notation,} \qquad \frac{\partial \sigma_{ij}}{\partial x_j} + \rho b_i = \rho a_i, \tag{5.7}$$

where $\boldsymbol{\sigma}$ is the Cauchy stress tensor, ρ is the spatial mass density, $\boldsymbol{b}$ is the body force per unit mass, $\boldsymbol{a}$ is the material acceleration (equal to the material rate of velocity), and $\operatorname{div}\boldsymbol{\sigma}$ is the spatial divergence of the stress.

After data relocalization was seen to be effective in the exploratory problem of Sec. 5.3, a simple 1D problem was designed using MMS to run in a finite-element code. Given that we are ultimately interested in understanding the mesh dependency of the Brazilian problem, the stress field in this 1D test was chosen to be the x-component of the stress across the diameter of the Brazilian problem:

$$\sigma\left(x,t\right) = -\frac{2P\left(-2. + \frac{0.5x^2}{(0.0625+x^2)^2}\right)}{\pi}; \tag{5.8}$$

where SI units are used; P is the applied load which is a function of time given by $P = 4 \times 10^{12}\ t$ and the length of the domain was chosen to be 0.5.

Reducing Eq. (5.7) to 1D gives

$$\frac{\partial \sigma\left(x,t\right)}{\partial x} + \rho b(x,t) = \rho a(x,t) \tag{5.9}$$

To get the body force $b(x,t)$ in Eq. (5.9), we need the acceleration. Using the stress field from Eq. (5.8), its corresponding displacement field can be obtained by the following set of equations

$$\sigma(x,t) = E\frac{\partial u(x,t)}{\partial x} \qquad \Rightarrow \frac{\partial u(x,t)}{\partial x} = \frac{\sigma(x,t)}{E} \qquad \Rightarrow u(x,t) = \int \frac{\sigma(x,t)}{E}\mathrm{d}x \tag{5.10}$$

Given a predetermined and time-varying displacement field, the initial velocity and acceleration on the right-hand side of Eq. (5.9) can be evaluated by

$$v(x,t) = \frac{\partial u(x,t)}{\partial t}; \qquad a(x,t) = \frac{\partial^2 u(x,t)}{\partial t^2} \tag{5.11}$$

Substituting Eqs. (5.11) and (5.8) in Eq. (5.9), the body force is evaluated as

$$b(x,t) = -\frac{tx\left(-1.59155 \times 10^{11} + 2.54648 \times 10^{12}x^2\right)}{\left(0.0625 + x^2\right)^3 \rho} \tag{5.12}$$

Simulations were run in the open-source **Uintah** computational framework [34], providing the initial conditions and the body force as inputs to the code. Kayenta [15] was used as the constitutive model. Kayenta is a stress-based plasticity model applicable to a broad class of materials including rocks, rock-like engineering materials, and metals. Verification was performed by running the 1D simulations for various mesh resolutions under linear elasticity. Young's modulus, density, and Poisson's ratio were chosen to be 453 GPa, 3227 $\frac{kg}{m^3}$, and 0.0, respectively. Simulations were run for five different mesh resolutions. Figure 5.4 compares the analytical solution and the numerical solution at the end of the simulation for the highest mesh resolution with 160 particles. The spatial L_2 error is defined as

$$\mathrm{L}_2 \text{ error} = \sqrt{\frac{1}{N_p}\sum_{N_p}\left\|\frac{\sigma_{\text{exact}}(x,t)}{\sigma_{\text{ref}}} - \frac{\sigma_{\text{app}}(x,t)}{\sigma_{\text{ref}}}\right\|^2} \tag{5.13}$$

where $\sigma_{\text{exact}}(x,t)$ and $\sigma_{\text{app}}(x,t)$ are, respectively, the analytical and numerical stress values at location x, N_p is total number of particles in the domain, and σ_{ref} is a reference stress (introduced to avoid overflow from large stress values) taken as $\sigma_{\text{ref}} = \max|\sigma_{\text{exact}}(x,t)|$. The L_2 error was calculated at the end of the simulation, t=0.001s. Figure 5.5 shows the convergence plot, where the error decreases with the increase in mesh resolution with the rate of convergence 1.1.

After verifying the elasticity solution, simulations were run using statistical variability in strength and scale effects using low-order shape functions. For each of four mesh resolutions, 25 different seeds (each providing different spatial realizations of strength, as shown in Fig. 5.6) were used to generate the data points on the Weibull plot. To focus exclusively on the mesh dependence for the *onset* of failure, these simulations were terminated at the instant that the first element became damaged inside the domain. The results from Fig. 5.7 demonstrate that a standard approach (*i.e.*, using a low-order shape function without m-norm relocalization) exhibits noticeable mesh dependence. The abscissa is normalized by

the median value of the most refined mesh resolution (black line). As seen by the black and blue (left-most) lines being closer to each other than any other pair of lines in Fig. 5.7), the solution does eventually converge. However, the degree of mesh refinement needed to achieve convergence would make this scale-dependent statistical damage theory impractical in large-scale engineering problems. A faster-converging method is needed.

As we are attributing the slow convergence to the inability of low-order shape functions to capture stress concentrations, it is natural to first investigate the benefit of using higher-order shape functions. Hence, the same simulations (using the same 25 seeds) were rerun using 3^{rd}-order BSplines [23]. Running them with the same seeds is important because we need to generate the same random realizations of strengths to have a fair comparison when using different techniques. The results in Fig. 5.8 show only minor improvement for the coarse mesh resolution compared to Fig. 5.7, but still not enough to warrant the increased computational cost of high-order shape functions.

To demonstrate that under-resolution of the stress field is indeed a major contributor to slow mesh convergence of the onset of failure, knowledge of the exact stress field prior to failure was exploited with data relocalization using low-order shape functions. At each particle and time step, a stress intensification factor α was calculated using:

$$\alpha = \left[\frac{1}{V}\int_V \left(\frac{\sigma_{\text{x-exact}}}{\sigma_{\text{x-app}}}\right)^m \mathrm{d}V\right]^{\frac{1}{m}} \tag{5.14}$$

Here, $\sigma_{\text{x-exact}}$ is value of the exact stress in Eq. (5.8), V is the volume of the element, $\sigma_{\text{x-app}}$ is the numerical prediction of the stress from the constitutive model, and m is the Weibull modulus. At each time step, the peak strength of each particle was reduced by the above α factor, effectively compensating for under-resolved stress concentrations with regard to material failure while allowing all other aspects of the model (such as elastic strain) to remain unchanged. Figure 5.9 demonstrates mesh independence for the onset of failure even at the coarsest resolution. This case study exploits a knowledge of the exact prefailure stress field to demonstrate that slow convergence of probabilistic failure theories can be at least partially attributed to a purely numerical problem of under-resolution of the stress field. Eliminating this source of error when an exact stress field is unknown would naturally require a nonlocal examination of the stress field, but such considerations are here attributed purely to numerical shortcomings and not to any physical need for nonlocality. All the failure probability curves nearly overlap with each other which is a much improved

---

Here and in all subsequent plots, stress is normalized by the median (sigbar) of the most refined mesh.

result compared to Figs. 5.7–5.8. The next section explores the effect of data relocalization on a more complicated Brazilian test problem.

5.5 Brazilian test

Stress analysis for an isotropic linear-elastic disc under diametrical compression has been developed in [92, 30]. The analytical stress components are [39]

$$\begin{aligned}
\sigma_x &= \frac{-2P}{\pi t}\left\{\frac{(R-y)\,x^2}{\beta_1^4}+\frac{(R+y)\,x^2}{\beta_2^4}-\frac{1}{D}\right\}\\
\sigma_y &= \frac{-2P}{\pi t}\left\{\frac{(R-y)^3}{\beta_1^4}+\frac{(R+y)^3}{\beta_2^4}-\frac{1}{D}\right\}\\
\tau_{xy} &= \frac{2P}{\pi t}\left\{\frac{(R+y)^2\,x}{\beta_1^4}-\frac{(R-y)^2\,x}{\beta_2^4}\right\}
\end{aligned} \tag{5.15}$$

where $\beta_1^2 = (R-y)^2+x^2$, $\beta_2^2 = (R+y)^2+x^2$, P is the applied load, D, R, and t are, respectively, the diameter, the radius, and the thickness of the disc.

Figure 5.10 shows the problem set up for the Brazilian test, where each material particle is assigned different strengths. A 2D plane-strain version of this problem was run in **Uintah** using Kayenta [15] as the constitutive model and with force applied through a rigid platen with prescribed displacement control. A linear Drucker-Prager was used as the strength model and the strength was perturbed by assigning a variability on PEAKI1 (which is the hydrostatic tensile limit of the intact material). The Brazilian simulations were run for three different mesh resolutions with statistical variability in strength and scale effects using low-order shape functions for the onset of failure (*i.e.*, simulations were stopped once any element inside the specimen was damaged). Weibull plots were generated for three different mesh resolutions. For each mesh, 25 simulations (using 25 different random seeds) were run to generate Monte-Carlo virtual test data that were then analyzed in the same manner as real test data to construct the Weibull plot for statistically variable strength.

Figure 5.11 shows the Weibull plot for the failure probability curves. As the mesh resolution is increased, the strength of the specimen is decreased with clear lack of convergence at the finest resolution. The results show a similar trend as the 1D MMS problem mentioned in Sec. 5.4. In particular, noting that the gap between the medium and fine mesh resolution is less than that of the coarse and medium mesh resolution, the Brazilian results indicate that perhaps convergence might be eventually achieved on an extraordinarily fine mesh (but which is too fine to be practical for nontrivial engineering applications).

Using the exact solution from Eq. (5.15), the data-relocalization technique was implemented to determine if the method could indeed increase the convergence rate so that good

results might be obtained on practical mesh resolutions. The relocalization stress intensifier (which, recall, is actually used as a strength reducer) was calculated using

$$\alpha = \left\{ \frac{1}{V} \int_V \left[\frac{\|\sigma\|_{\text{exact}}}{\|\sigma\|_{\text{app}}} \right]^m \mathrm{d}V \right\}^{\frac{1}{m}} \tag{5.16}$$

where $\|\sigma\|_{\text{exact}}$ is the norm of the exact stress tensor, V is the volume of the particle, $\|\sigma\|_{\text{app}}$ is the norm of the numerical prediction of stress from the constitutive model, and m is the Weibull modulus. The same simulations were rerun with data relocalization (using the same seeds), and the results in Fig. 5.12 show significantly faster convergence (the failure probability curves nearly overlap with each other even at the coarsest mesh).

5.6 Conclusions

This chapter presented an alternative numerical stress-field regularization technique to improve rate of convergence for failure initiation statistics. By applying an m-norm strength reduction factor that effectively reverses data delocalization methods commonly used to to analyze experimental data, our new "data relocalization" scheme eliminated mesh sensitivity (slow convergence) for the onset of failure in 1D statistically variable and scale-dependent strength simulations. Similar benefits of data relocalization were demonstrated in a more complicated Brazilian test problem. These exercises exploited knowledge of the prefailure stress field in order to demonstrate clearly that under-resolution of the stress field is a significant contributor to mesh sensitivity even when high-order shape functions are used. Applying data relocalization to realistic problems for which the prefailure stress field is unknown will require a nonlocal examination of neighboring stress states in order to estimate stress concentrations, but a key difference of such work is that the nonlocal considerations would then be mitigating a numerical shortcoming, rather than imposing any underlying *physical* requirement of nonlocality.

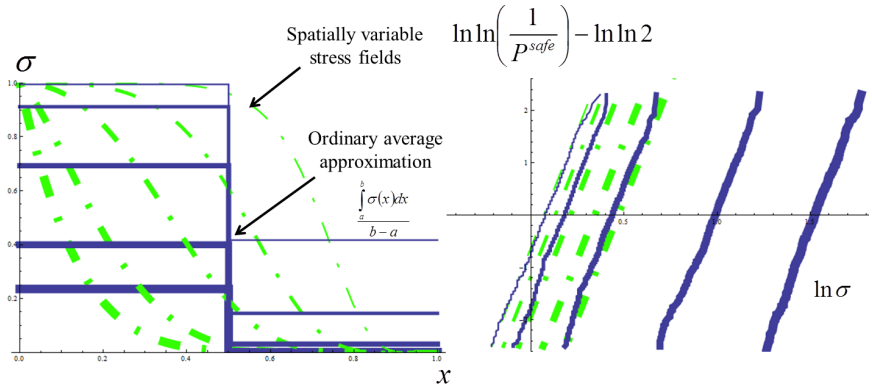

Figure 5.1: The two-element exploratory problem. Left: Green dashed lines are the known stress fields over the element. Solid blue lines are the corresponding ordinary (1-norm) average approximation over the element (*i.e.*, thick blue line corresponds to thick green line). Right: Green lines are the analytical Weibull lines. Blue lines are the corresponding numerical failure probability curves

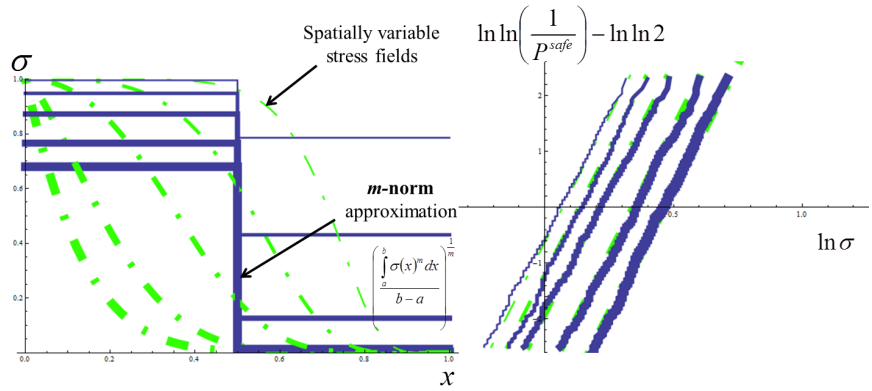

Figure 5.2: The same analysis as in Fig. 5.1 except the ordinary average is replaced with the "relocalized" m-norm average

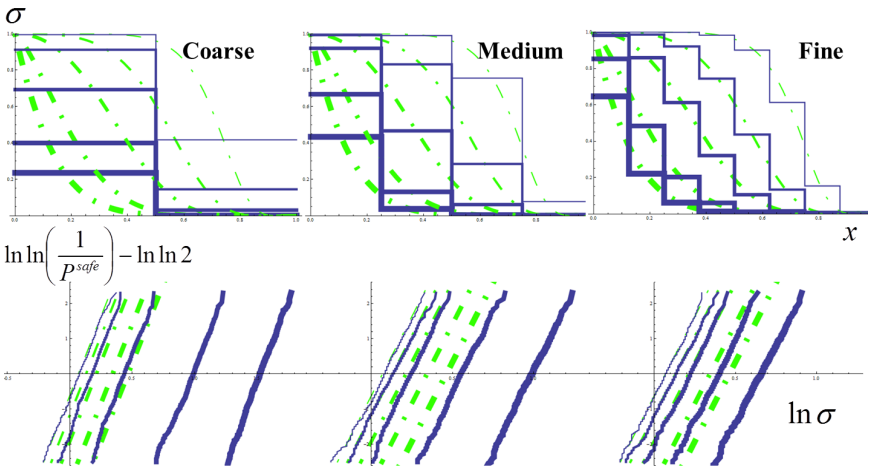

Figure 5.3: Mesh resolution increases from left to right. With mesh refinement, the numerical failure probability curves approach the analytical failure probability curves

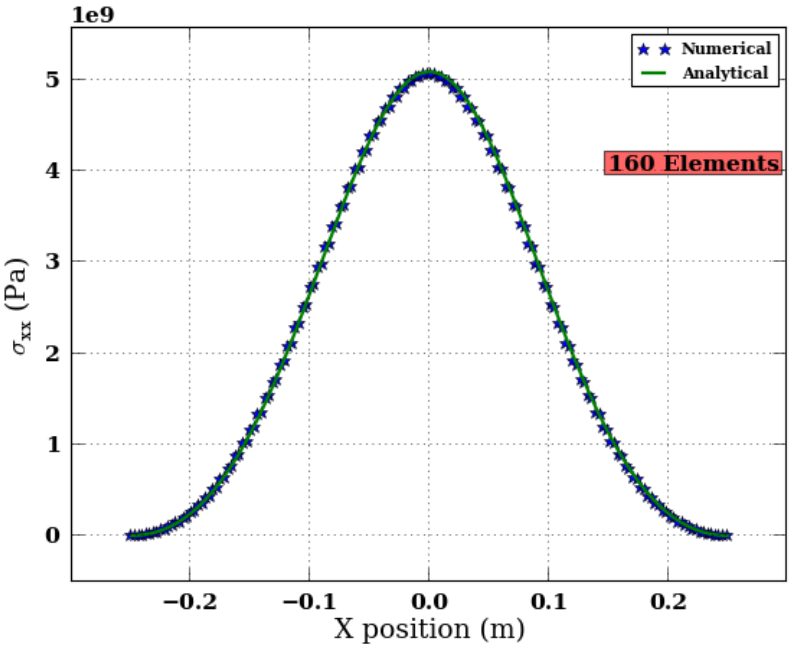

Figure 5.4: The analytical solution and the simulation at the highest mesh resolution

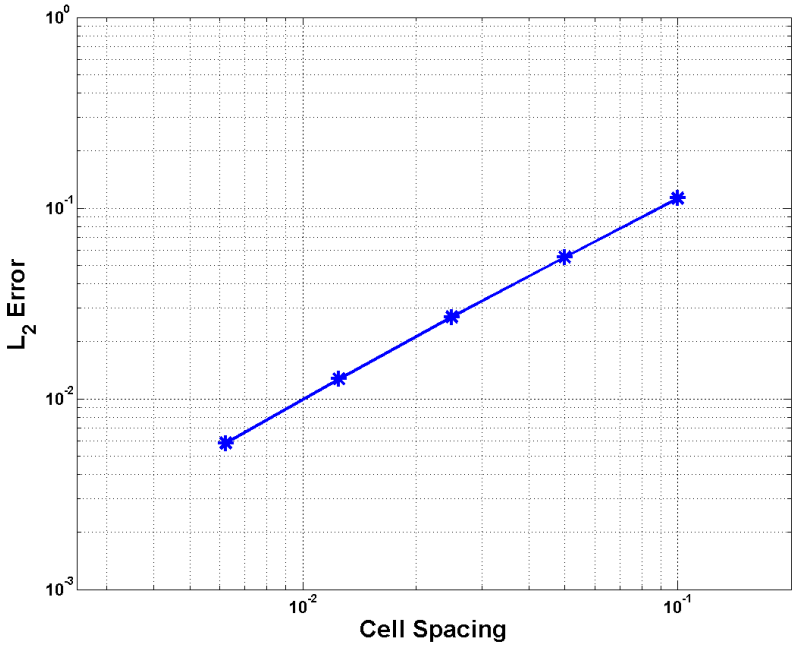

Figure 5.5: Convergence plot for the elasticity solution

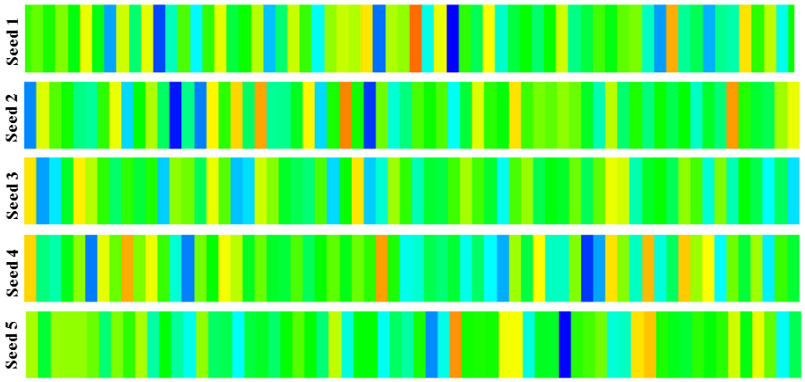

Figure 5.6: Weibull strength realizations at locations on the 1D bar using different seeds. Blue is 2.5×10^8 Pa and red is 8×10^8 Pa

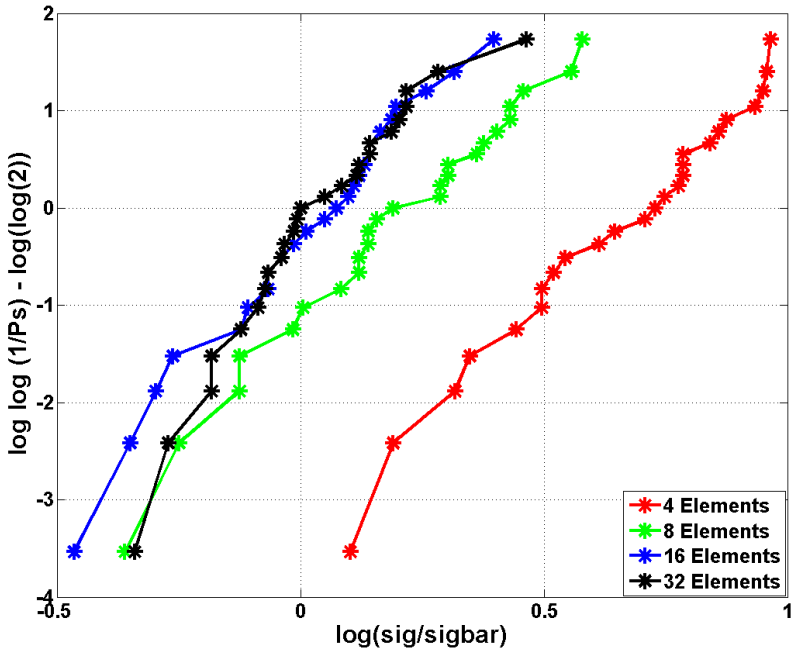

Figure 5.7: Slow convergence for the onset of failure when using low-order shape functions

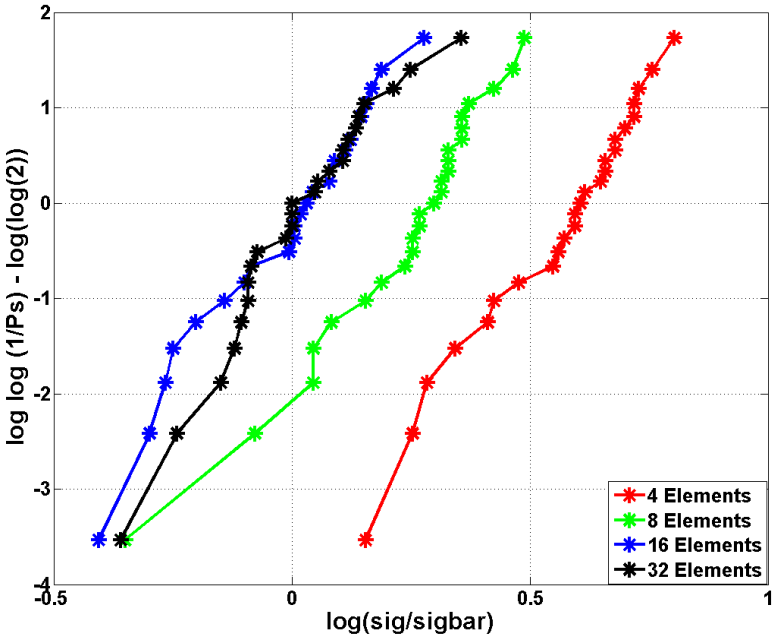

Figure 5.8: Weibull plot using higher-order shape functions also exhibiting slow convergence for the onset of failure

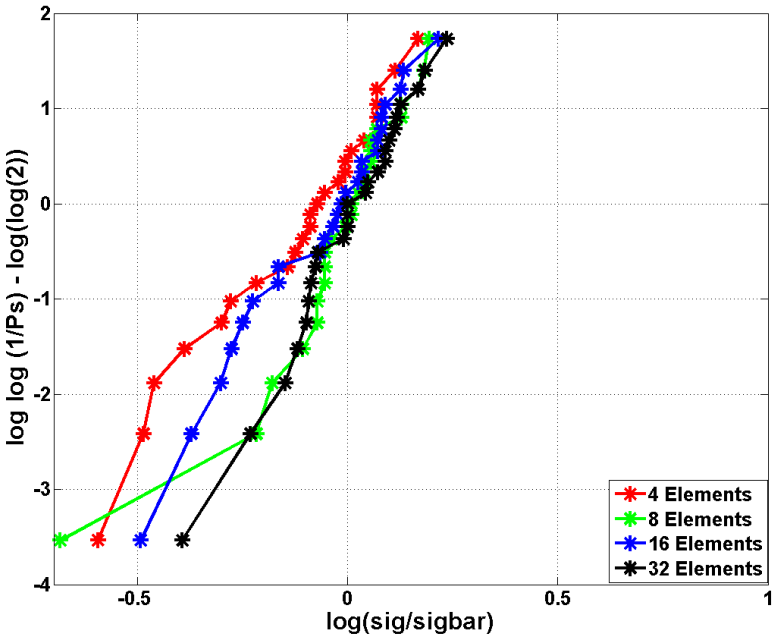

Figure 5.9: Weibull plot using data relocalization demonstrating mesh independence for the onset of failure

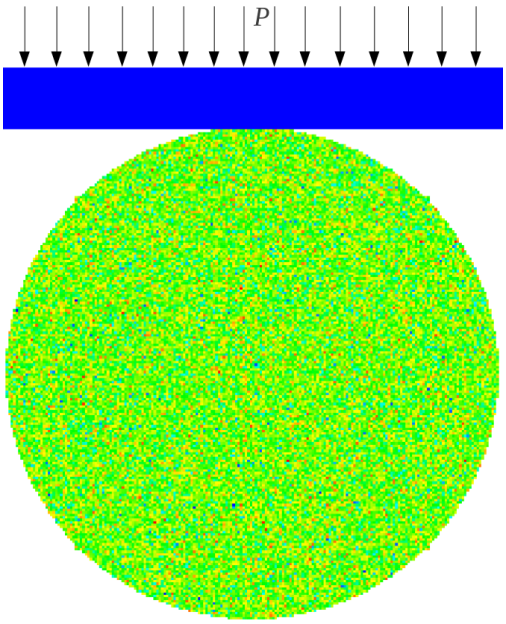

Figure 5.10: Problem set up for the Brazilian test. Colors depict homogeneous statistical variability in strength

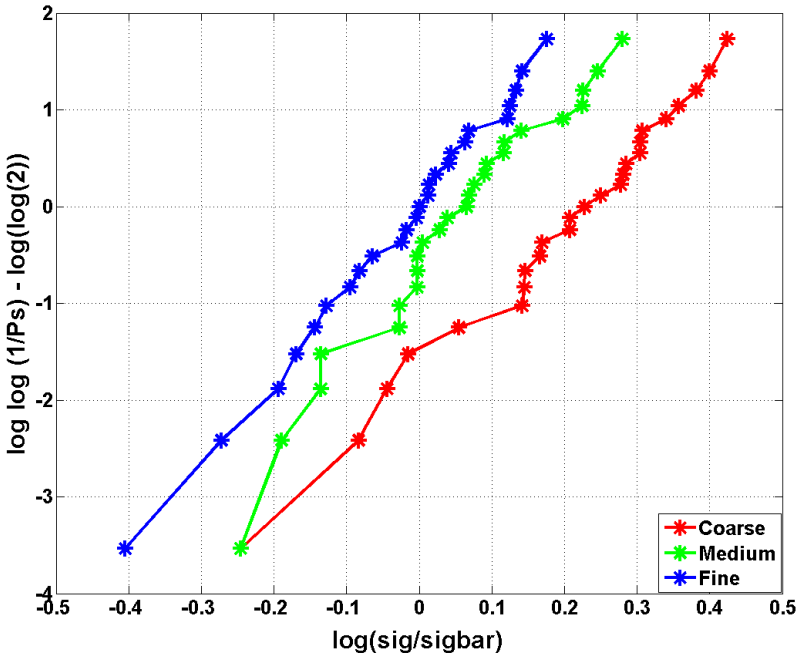

Figure 5.11: Weibull plot using low-order shape functions. As the mesh resolution is increased the strength of the specimen is decreased with a clear lack of convergence

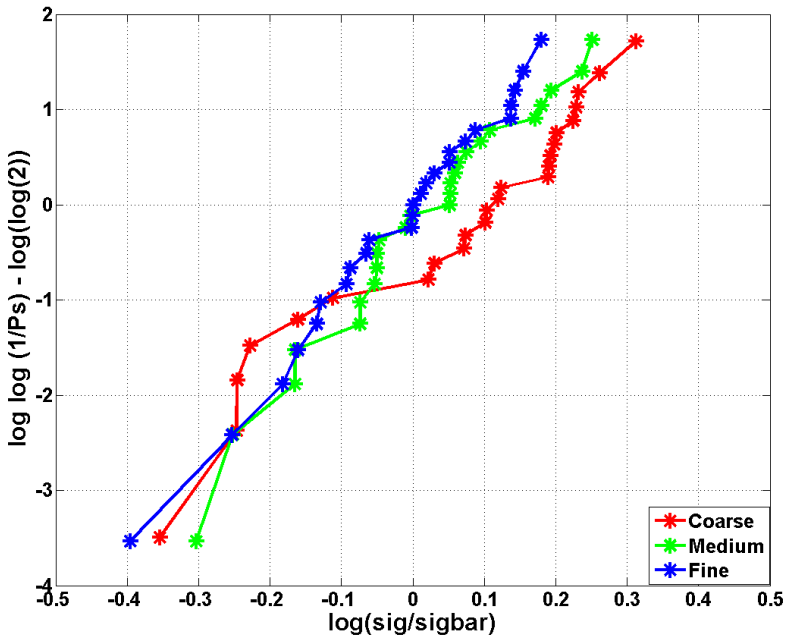

Figure 5.12: Weibull plot using data relocalization, demonstrating a markedly improved convergence rate compared to Fig. 5.11

CHAPTER 6

CONCLUSIONS

6.1 Novel contributions to the current state of knowledge

This dissertation has advanced the current state of knowledge of verification and validation in solid-mechanics. Each subsection below describes one of these areas.

6.1.1 Code verification tests for nonlinear elastic constitutive models under large deformations

As described in Chapter 2, code verification in solid mechanics lags behind other scientific communities. To address this gap, several increasingly complicated verification tests were presented for nonlinear elastic constitutive models. Previous researchers had designed manufactured solutions for solid-mechanics codes, but the solutions were designed for simpler cases *i.e.,* small-strain settings, no material rotations, *etc.* Two nonhomogeneous large-deformation verification problems with varying levels of superimposed rotations were designed using the well-established verification technique called the "method of manufactured solutions (MMS)." These tests might serve as standards suitable to quantify accuracy, robustness, and convergence of momentum solvers used in solid-mechanics codes. Though these verification tests were illustrated using the material point method (MPM), they are suitable to test the finite-element method (FEM) as well.

6.1.2 Code verification tests for plastic constitutive models under large deformations

Applications in aerospace, defense, automotive, safety, *etc.*, often entail large deformations with plasticity and damage. Therefore, verification of such complicated constitutive models is crucial before using them in the validation process. This is addressed in Chapter 3. MMS deformation fields are designed for both homogeneous and nonhomogeneous large deformations using von-Mises plasticity *with load reversals*. These tests can be used to verify the implementation of a von-Mises plasticity model or any model that includes

von-Mises plasticity as a special case [43, 15]. Also, by running them for loading only, these problems can be used to verify a simpler case of constant strain-to-failure damage option (*c.f.*, [44, 96]). To our knowledge, these manufactured solutions are the first of their kind designed for plasticity with load reversals.

6.1.3 Modeling damage and fragmentation using aleatory uncertainty

Chapter 4 describes a detailed validation study performed on unnotched Charpy and Taylor-anvil impact simulations using a single material model (Kayenta). For the unnotched Charpy test, statistical variability was applied to quasistatic strength, and good agreement was observed between the experimental and numerical results. The inclusion of scale effects improved the fracture patterns in the simulations. Since Taylor-anvil impact involves high rates, a verification suite was designed to test the implementation of rate dependence used simultaneously with softening (this combined capability required modifications to Kayenta). Statistically perturbing the quasistatic strength did not alleviate nonconvergence in Taylor-anvil impact simulations. Therefore, this study instead put the statistical variability on the rate dependence parameters T_1 and T_2 so that low rates would show ductile response while high rates would (in principle) exhibit more brittle behavior. Improved results using statistics on rate-dependence parameters were achieved, although the results still fall short of adequately reproducing experimental observations of discrete fragmentation. A critical assessment of validation studies on similar Taylor-anvil tests in the literature is provided.

6.1.4 Data relocalization

Chapter 5 presents a novel numerical alternative stress field regularization technique called "data relocalization" to preserve the probability of failure initiation of a finite subdomain of the body regardless of whether it is discretized into few or many elements. This technique effectively makes use of the known analytical prefailure stress and assigns the m-norm of the actual stress field over the element to a low-order finite element. Though convergence on failure initiation statistics was demonstrated for a fine mesh using variability in strength and scale effects on a 1D MMS problem and a more complicated Brazilian test, the rate of convergence was very slow. Data relocalization significantly accelerated the rate of convergence for both problems with low-order elements when the prefailure stress field is known. This work demonstrated (for the first time) a purely numerical source of nonconvergence associated with scale effects.

6.2 Suggestions for future work

This dissertation describes new developments in the area of verification and validation for solid mechanics, and several suggestions are proposed for further research. In the area of verification, the manufactured solutions provided in Chapters 2 and 3 are for nonlinear elastic and perfectly plastic constitutive models. The loading leg of these plasticity MMS problems can also be used to verify constant strain-to-failure damage models. These solutions are directly applicable only to rate-independent constitutive models that do not include hardening. However, starting with the simpler case of homogeneous deformation, these MMS problems can be extended to von-Mises plasticity with hardening laws. For applications that include high strain rates and damage (*e.g.,* impact, penetration, *etc.*), the constitutive models have to be rate dependent. In principle, these MMS problems may also be extended to such rate-dependent constitutive models including damage.

Three-dimensional Charpy impact simulations are computationally very expensive. In the long term, it would be prudent to use dimensional analysis (*e.g.,* Buckingham-Pi theorem) to identify dimensionless groups applicable to Charpy impact problems. This might, for example, ultimately allow running simulations at an increased impact speed that also have other input data scaled appropriately so that the fast-impact simulation is a predictive surrogate for the actual problem of interest. When using strain-to-failure softening with statistical variability in strength and scale effects, nonconvergence was observed in the energy absorbed by the specimen during the softening phase. This convergence study can be re-analyzed using a scaled time-to-failure softening option with statistical variability in strength and scale effects in Kayenta, which has previously reduced mesh dependency during softening in a particular dynamic sphere indentation problem.

For the Taylor-anvil impact simulations in Chapter 4, based on the available experimental data, the yield strength was chosen to be pressure independent. The confining pressures used in these experiments were in the range of 0 - 300 MPa. However, the impact pressures in the numerical simulations of Taylor-anvil impact are of the order of 8 GPa, which are well outside the available experimental data. Therefore, these simulations may be rerun using pressure-dependent strength to investigate the sensitivity of the results to this feature.

In the open literature, numerical predictions of fragmentation in Taylor-anvil impact simulations use modified conventional plasticity models and statistics on failure models. First using these models to reproduce the published results, and then applying them to the Taylor-anvil impact simulations of Ti6Al4V may provide insight into the importance of features not in Kayenta that are needed to predict fragmentation.

The data relocalization concept explained in Chapter 5 assumes that the analytical solution for prefailure stress is known. For the 1D MMS problem, 3^{rd}-order BSplines showed only minor improvement on the convergence rate compared to low-order shape functions. That analysis, however, did not evaluate the m-norm of the higher-order description of the stress field. The same problem can be re-analyzed by taking the m-norm of the higher-order description of the stress field and then calculating the convergence rate. If this improves the convergence rate, then this technique can be used for problems where analytical solutions for the prefailure stress are not known.

REFERENCES

[1] Standard test methods for notched bar impact testing of metallic materials. E-23 07a, ASTM International, 2007.

[2] D. F. Aldridge. Elastic wave radiation from a pressurized spherical cavity. Technical report, Sandia National Laboratories, 2002.

[3] D. Appelo, J. W. Banks, W. D. Henshaw, and D. W. Schwendeman. Numerical methods for solid mechanics on overlapping grids: linear elasticity. *J Comput Phys*, preprint submitted:45, 2012.

[4] D. Appelo and N. A. Petersson. A stable finite difference method for the elastic wave equation on complex geometries with free surfaces. *J Comput Phys*, 5:84–107, 2009.

[5] I. Babuska and J. T. Oden. Verification and validation in computational engineering and science: basic concepts. *Comput. Methods Appl. Mech. Engrg.*, 193:(10)4057–4066, 2004.

[6] Y. Bai and T. Wierzbicki. A new model of metal plasticity and fracture with pressure and lode dependence. *Int. J. Plasticity*, 24(6):1071 – 1096, 2007.

[7] B. Banerjee. Method of manufactured solutions. http://www.eng.utah.edu/ banerjee/notes/mms.pdf, October 2006.

[8] S. Bardenhagen and E. Kober. The generalized interpolation material point method. *Comput. Model. Eng. Sci.*, 5:477–495, 2004.

[9] R. Batra and X. Liang. Finite dynamic deformations of smart structures. *Comput. Mech.*, 20:427–438, 1997.

[10] Z. Bažant, Y. Xiang, M. Adley, P. Prat, and S. Akers. Microplane model for concrete. II: data delocalization and verification. *J. Eng. Mech.*, 122(3):255–262, 1996.

[11] Z. Bažant, Y. Xiang, and P. Prat. Microplane model for concrete. I: stress-strain boundaries and finite strain. *J. Eng. Mech.*, 122(3):245–254, 1996.

[12] M. Benes and K. Matous. Asynchronous multi-domain variational integrators for nonlinear hyperelastic solids. *Comput. Method. Appl. M.*, 199:1992–2013, 2010.

[13] R. Boyer and G. Welsch. *Material properties handbook - titanium alloys.* ASM International, 1994.

[14] R. Brannon. *Elements of phenomenological plasticity: geometrical insight, computational algorithms, and applications in shock physics.* Chapter 6, Springer - New York, 2007.

[15] R. Brannon, A. Fossum, and O. Strack. Kayenta: theory and user's guide. Technical Report SAND2009-2282, USDOE, Mar 2009.

[16] R. Brannon and S. Leelavanichkul. Survey of four damage models for concrete. Technical Report SAND2009-5544, USDOE, 2009.

[17] R. Brannon, J. Wells, and O. Strack. Validating theories for brittle damage. *Metall. Mater. Trans. A.*, 38:2861–2868, 2007.

[18] T. Brunner. Development of a grey nonlinear thermal radiation diffusion verification problem. *Trans Am Nucl Soc*, 95:876–878, 2006.

[19] M. M. Carroll and A. C. Holt. Static and dynamic pore-collapse relations for ductile porous materials. *J. Appl. Phys*, 43, 1972.

[20] D. Casem, H. Meyer, and J. Cardenas-Garcia. Re-examining the taylor impact test using a finite-element-based inverse problem methodology. In *Proceedings of the 2005 Society for Experimental Mechanics Annual Conference and Exposition on Experimental and Applied Mechanics*, 2005.

[21] A. Charpy. Note sur lessai des mtaux la flexion par choc de barreaux entaills. *Soc. Ing. Civ. de*, pages 848–877, 1901.

[22] D. G. S. Davies. The statistical approach to engineering design in ceramics. *Proc. Brit. Ceram. Soc*, 22:429–452, 1973.

[23] C. De Boor. *A practical guide to splines / Carl de Boor*. Springer-Verlag, New York, 1978.

[24] G. Duvaut and J. Lions. Les inequations en mecaniquie et en physique. Technical report, Dunod, Paris, 1972.

[25] D. Edelen and N. Laws. On the thermodynamics of systems with nonlocality. *Arch. Ration. Mech. An.*, 43(1):24–35, 1971.

[26] E. El-Magd and M. Abouridouane. Characterization, modelling and simulation of deformation and fracture behaviour of the light-weight wrought alloys under high strain rate loading. *Int. J. Impact. Eng.*, 32(5):741 – 758, 2006.

[27] A. C. Eringen. Theories of nonlocal plasticity. *Int. J. Impact. Eng.*, 21:741–751, 1983.

[28] L. Ea and M. Hoekstra. Evaluation of numerical error estimation based on grid refinement studies with the method of the manufactured solutions. *Comput. A. Fluids.*, 38(8):1580 – 1591, 2009.

[29] N. A. Fleck, G. M. Muller, M. F. Ashby, and J. W. Hutchinson. Strain gradient plasticity: theory and experiment. *Acta. Metall. Mater.*, 42(2):475–487, Feb. 1994.

[30] M. Frocht. *Photoelasticity*. John Wiley & Sons, NewYork, 1947.

[31] X. L. Gao. Elasto-plastic analysis of an internally pressurized thick-walled cylinder using a strain gradient plasticity theory. *Int. J. Solids. Struct.*, 40(23):6445 – 6455, 2003.

[32] S. S. Gautam, R. Babu, and P. Dixit. Ductile fracture simulation in the taylor rod impact test using continuum damage mechanics. *Int. J. Damage. Mech.*, 20:347–369, 2011.

[33] L. Graham-Brady. Statistical characterization of meso-scale uniaxial compressive strength in brittle materials with randomly occurring flaws. *Int. J. Solids. Struct.*, 47(1819):2398 – 2413, 2010.

[34] J. Guilkey, T. Harman, J. Luitjens, J. Schmidt, J. Thornock, J. D. de St. Germain, S. Shankar, J. Peterson, and C. Brownlee. *Uintah user guide.* SCI Institute Technical Report, 2009.

[35] A. L. Gurson. Continuum theory of ductile rupture by void nucleation and growth: part i. yield critetria and flow rules for porous ductile media. *J. Eng. Mater.*, 99:2–15, 1977.

[36] J. T. Hammer. Plastic deformation and ductile fracture of ti-6al-4v under various loading conditions. Master's thesis, The Ohio State University, 2012.

[37] E. Hanina, D. Rittel, and Z. Rosenberg. Pressure sensitivity of adiabatic shear banding in metals. *App. Phy. Letters.*, 90(2), 2007.

[38] A. Hazen. Storage to be provided in impounding reservoirs for municipal water supply. *Trans. Am. Soc. Civ. Eng.*, 77:1547–1550, 1914.

[39] H. Hertz. *Stresses and deflections of cylindrical bodies.* Leipzig, 1895.

[40] F. Hild, P. Forquin, C. Denoual, and X. Brajer. Probabilistic-deterministic transition involved in a fragmentation process of brittle materials: application to a high performance concrete. *Lat. Am. J. Solids. Stru.*, 2:41–56, 2005.

[41] R. Hill. *The mathematical theory of plasticity.* Oxford, 1950.

[42] I. Jassim, D. Stolle, and P. Vermeer. Two-phase dynamic analysis by material point method. *Int. J. Numer. Anal. Met.*, 37(15):2502–2522, 2013.

[43] G. Johnson and W. Cook. A constitutive model and data for metals subjected to large strains, high strain rates and high temperatures. In *Proc. of the 7th International Symposium on Ballistics, The Netherlands*, pages 541–547, 1983.

[44] G. Johnson and W. Cook. Fracture characteristics of three metals subjected to various strains, strain rates, temperatures and pressures. *Eng. Fract. Mech.*, 21(1):31 – 48, 1985.

[45] G. Johnson and T. Holmquist. An improved computational constitutive model for brittle materials. *AIP. Conf. Proc.*, 309(1):981–984, 1994.

[46] K. Kamojjala, R. Brannon, A. Sadeghirad, and J. Guilkey. Verification tests in solid mechanics. *Eng. Comput.*, pages 1–21, 2013.

[47] A. Kelly and R. Nicholson. Precipitation hardening. *Prog. Mater. Sci*, 10(3):149–391, 1963.

[48] A. S. Khan. Responses and modeling of electron beam single melt ti-6al-4v alloys. Technical report, U.S Army Research, 2010.

[49] A. S. Khan, R. Kazmi, and B. Farrokh. Multiaxial and non-proportional loading responses, anisotropy and modeling of ti6al4v titanium alloy over wide ranges of strain rates and temperatures. *Int. J. Plasticity.*, 23(6):931 – 950, 2007.

[50] J. Kimberley, K. Ramesh, and N. Daphalapurkar. A scaling law for the dynamic strength of brittle solids. *Acta. Mater.*, 61(9):3509 – 3521, 2013.

[51] P. Knupp and K. Salari. *Verification of computer codes in computational science and engineering.* Chapman and Hall/CRC, 2003.

[52] J. E. Kozdon, E. M. Dunham, and J. Nordstrom. Simulation of dynamic earthquake ruptures in complex geometries using high-order finite difference method. *J Sci Comput*, 55:92–124, 2013.

[53] C. S. Kuo, H.-T. Hu, R.-M. Lin, K.-Y. Huang, P.-C. Lin, Z.-C. Zhong, and M.-L. Hseih. Biomechanical analysis of the lumbar spine on facet joint force and intradiscal pressure - a finite element study. *BMC Musculoskeletal Disorders*, 151:11, 2010.

[54] R. B. Leavy, R. M. Brannon, and O. E. Strack. The use of sphere indentation experiments to characterize ceramic damage models. *Int. J. Appl. Ceram. Tec.*, 7:606–615, 2010.

[55] D. Lesuer. Experimental investigations of material models for Ti-5Al-4V titanium and 2024-T3 aluminum. Technical report, FAA Report DOT/FAA/AR-00/25, Sep 2000.

[56] E. Love and D. Sulsky. An unconditionally stable, energy momentum consistent implementation of the material-point method. *Comput. Methods. Appl. M.*, 195:3903–3925, 2006.

[57] L. E. Malverin. *Introduction to the mechanics of a continuous medium.* Prentice-Hall, Inc., 1969.

[58] M. Martin, T. Shen, and N. Thadhani. Instrumented anvil-on-rod impact experiments for validating constitutive strength model for simulating transient dynamic deformation response of metals. *Mater. Sci. Eng.*, 494(12):416 – 424, 2008.

[59] C. Mast, P. Mackenzie-Helnwein, P. Arduino, G. Miller, and W. Shin. Mitigating kinematic locking in the material point method. *J. Comput. Phy.*, 231(16):5351 – 5373, 2012.

[60] P. Maudlin, J. Bingert, and G. G. III. Low-symmetry plastic deformation in bcc tantalum: experimental observations,modeling and simulations. *Int. J. Plasticity.*, 19:483515, 2003.

[61] F. A. McClintock. A criterion for ductile fracture by growth of holes. *J. Appl. Mech.*, 17:201–217, 1968.

[62] M. A. Meyers. *Dynamic behaviour of metals.* John Wiley & Sons, New Jersy, 1994.

[63] J. Monaghan. Introduction to sph. *Comput. Phys. Commun.*, 48:89–96, 1988.

[64] H. Mhlhaus and E. Alfantis. A variational principle for gradient plasticity. *Int. J. Solids. Struct.*, 28(7):845 – 857, 1991.

[65] W. L. Oberkampf, T. G, Trucano, and C. Hirsh. Verification and validation of modeling and simulation in computer science and engineering applications. In *Foundations of Verification and Validation in 21st Century Workshop*, 2002.

[66] W. L. Oberkampf and C. J. Roy. Verification and validation in scientific computing. Cambridge, UK, Cambridge University Press, 2010.

[67] W. L. Oberkampf and T. G. Trucano. Verification and validation in computational fluid dynamics. *Prog. Aerosp. Sci.*, 38:209–272, 2002.

[68] S. D. Pautz. Verification of transport codes by the method of manufactured solutions the attila experience. In *Proc. ANS International Meeting on Mathematical Methods for Nuclear Applications*, Salt Lake City, Utah, 2001.

[69] K. Rakvg, T. Brvik, and O. Hopperstad. A numerical study on the deformation and fracture modes of steel projectiles during taylor bar impact tests. *Int. J. Solids. Struct.*, 51(34):808 – 821, 2014.

[70] M. M. Rashid. Incremental kinematics for finite element applications. *Int. J. Num. Meth. in Engr.*, 36:(23)3937–3956, 1993.

[71] J. R. Rice and D. M. Tracey. On the ductile enlargement of voids in triaxial stress fields. *J. Mech. Phys. Solids*, 17:201–217, 1969.

[72] R. Rieben and D. A. White. Verification of high-order mixed fem solution of transient magnetic diffusion problems. Technical report, Lawrence Livermore National Laboratory, 2005.

[73] P. J. Roache. *Fundamentals of verification and validation*, volume 41. SIAM, 1999. Editor: Mark Anisworth.

[74] P. J. Roache. *Fundamentals of verification and validation.* Hermosa Publishers, 2009.

[75] C. J. Roy, C. C. Nelson, T. M. Smith, and C. C. Ober. Verification of euler/navier stokes codes using the method of manufactured solutions. *Int. J. Num. Meth. in Fluids.*, 44:599–620, 2004.

[76] C. J. Roy and W. L. Oberkampf. A comprehensive framework for verification, validation, and uncertainty quantification in scientific computing. *Comput. Methods Appl. Mech. Engrg.*, 200:2131–2144, 2011.

[77] A. Sadeghirad, R. Brannon, and J. Burghardt. A convected particle domain interpolation technique to extend applicability of the material point method for problems involving massive deformations. *Intl. J. Num. Meth. Engng.*, 86:(22)1435–1456, (2011).

[78] A. Sadeghirad, R. Brannon, and J. Guilkey. Second-order convected particle domain interpolation (CPDI2) with enrichment for weak discontinuities at material interfaces. *Intl. J. Num. Meth. Engng.*, 95:928–952, 2013.

[79] L. Schwer. Guide for verification and validation in computational solid mechanics. In *The American Society of Mechanical Engineers.* ASME, 2006.

[80] W. Spitzig, R. Sober, and O. Richmond. Pressure dependence of yielding and associated volume expansion in tempered martensite. *Acta. Metall. Mater.*, 23(7):885 – 893, 1975.

[81] W. Spitzig, R. Sober, and O. Richmond. The effect of hydrostatic pressure on the deformation behavior of maraging and hy-80 steels and its implications for plasticity theory. *Metall. Trans.*, 7(11):1703–1710, 1976.

[82] M. Steffen, P. Wallstedt, J. Guilkey, R. Kirby, and M. Berzins. Examination and analysis of implementation choices within the material point method (mpm). *Comput. Model. Eng. Sci.*, 2:107–127, 2008.

[83] D. J. Steinberg. Equation of state and strength properties of selected materials. Technical report, LLNL, 1996.

[84] S. Steinberg and P. Roache. Symbolic manipulation and computational fluiddynamics. *J Comput Phys*, 57:251284, 1985.

[85] A. Stomakhin, C. Schroeder, L. Chai, J. Teran, and A. Selle. A material point method for snow simulation. *ACM Trans. Graph.*, 32(4):102:1–102:10, July 2013.

[86] O. E. Strack, R. B. Leavy, and R. M. Brannon. Aleatory uncertainty and scale effects in computational damage models for failure and fragmentation. *Int. J. Num. Meth. in Engr*, In Press, 2014.

[87] D. Sulsky, A. Chen, and H. Schreyer. A particle method for history-dependent materials. *Comput. Method. Appl. M.*, 118:179–196, 1994.

[88] M. S. Swan. Incorporation of a general strain-to-failure fracture criterion into a stress-based plasticity model through a time-to-failure softening mechanism. Master's thesis, University of Utah, 2012.

[89] G. Taylor. The use of flat ended projectiles for determining yield stress. i: theoretical consideration. *Proc. R. Soc*, 194:298, 1948.

[90] X. Teng, T. Wierzbicki, S. Hiermaier, and I. Rohr. Numerical prediction of fracture in the taylor test. *Int. J. Solids. Struct.*, 42(9-10):2929 – 2948, 2005.

[91] M. Timmel, S. Kolling, P. Osterrieder, and P. D. Bois. A finite element model for impact simulation with laminated glass. *Int. J. Impact. Eng.*, 34:1465–1478, 2007.

[92] S. Timoshenko and J. Goodier. *Theory of elasticity*. McGraw-Hill, 1970.

[93] D. Tremblay, S. Etienne, and D. Pelletier. Code verification and the method of manufactured solutions for fluid-structure interaction problems. In *36th AIAA Fluid Dynamics Conference*, volume 2, pages 882–892, 2006.

[94] P. Wallstedt and J. Guilkey. An evaluation of explicit time integration schemes for use with the generalized interpolation material point method. *J. Comput. Phy.*, 227:9628–9642, 2008.

[95] W. Weibull. The phenomenon of rupture in solids. *Swedish Academy of Engineering Science Proceedings*, 153:1–55, 1939.

[96] T. Wierzbicki, Y. Bao, Y. Lee, and Y. Bai. Calibration and evaluation of seven fracture models. *Int. J. Mech. Sci.*, 47(4-5):719 – 743, 2005.

[97] M. Wilkins, R. Streit, , and J. Reaugh. Cumulative-strain-damage model of ductile fracture: Simulation and prediction of engineering fracture tests. Technical Report Technical Report UCRL- 53058, Lawrence Livermore National Laboratory, 1980.

[98] M. Wilkins, R. Streit, and J. Reaugh. Cumulative-strain-damage model of ductile fracture: simulation and prediction of engineering fracture tests. Technical report, Lawrence Livermore National Laboratory, 1980.

[99] H. Xiao, . T. Bruhns, and A. Meyers. A closed-form solution to finite bending of a compressible elastic-perfectly plastic rectangular block. *Defence. Sci. J.*, 53(1):25–39, 2003.

[100] X. Xiao, W. Zhang, G. Wei, and Z. Mu. Effect of projectile hardness on deformation and fracture behavior in the taylor impact test. *Mater. Des.*, 31(10):4913 – 4920, 2010.

[101] X. Xiao, W. Zhang, G. Wei, Z. Mu, and Z. Guo. Experimental and numerical investigation on the deformation and failure behavior in the taylor test. *Mater. Des.*, 32(5):2663 – 2674, 2011.

[102] V. M. Yarushina, M. Dabrowski, and Y. Y. Podladchikov. An analytical benchmark with combined pressure and shear loading for elastoplastic numerical models. *Geochemistry, Geophysics, Geosystems*, 11(8), 2010.

[103] H. Zhang, K. Wang, and Z. Chen. Material point method for dynamic analysis of saturated porous media under external contact/impact of solid bodies. *Comput. Method. Appl. M.*, 198(1720):1456 – 1472, 2009.

[104] S. Zhou, X. Zhang, and H. Ma. Numerical simulation of human head impact using the material point method. *Int. J. Comput. Meth.*, 10(04):1350014, 2013.